universität
wien

DISSERTATION

Titel der Dissertation

Two-Dimensional Electronic Spectroscopy of Molecular Systems

Verfasser

Mag. rer. nat. Jaroslaw Sperling

angestrebter akademischer Grad

Doktor der Naturwissenschaften (Dr. rer. nat.)

Wien, 2010

Studienkennzahl lt. Studienblatt:	A 091 419
Dissertationsgebiet lt. Studienblatt:	Chemie
Betreuerin / Betreuer:	Prof. Harald Friedrich Kauffmann

CONTENTS

1. *Introduction* 1

2. *Theoretical Framework* 9
   - 2.1 Dynamic Quantum Systems and Perturbation Theory 10
   - 2.2 Perturbative Expansion of the Density Matrix and Nonlinear Polarization . 15
   - 2.3 Modeling the Nonlinear Response of Excitonic Systems 18

3. *Two-Dimensional Spectra of Symmetric Dimers - A Theoretical Study* 25
   - 3.1 Introduction 26
   - 3.2 Two-Dimensional Photon-Echo Spectra 27
   - 3.3 Linear Absorption Spectra 33
   - 3.4 Spectra of Discrete Conformational Distributions 34
   - 3.5 Conclusions 40

4. *Experimental Design* 43
   - 4.1 Introduction 44
   - 4.2 Pulse Generation 46
   - 4.3 Experimental Set-up and Procedures 49

5. *Phonon-Coupling of a Two-Level System* 59
   - 5.1 Introduction 60
   - 5.2 Experiment and Results 62
   - 5.3 Simulations and Discussion 64
   - 5.4 Analytical Considerations 67
   - 5.5 Conclusions 69

6. Simultaneous Characterization of Monomeric and Dimeric Lineshapes 73

6.1 Introduction 74

6.2 Experiment and Results 76

6.3 Simulations and Discussion 79

6.4 Conclusions 87

7. Exciton Motion in Molecular Nanotubes 89

7.1 Introduction 90

7.2 Linear and Nonlinear Experiments 91

7.3 Simulations and Discussion 96

7.4 Conclusions 101

8. Outlook 107

1. INTRODUCTION

> *The basic principles which have been exploited are very general and can be applied to other coherent spectroscopies as well. Applications are conceivable in electron spin resonance, nuclear quadrupole resonance, in microwave rotational spectroscopy, and possibly in laser infrared spectroscopy.*
>
> R. R. Ernst and co-workers in *J. Chem. Phys.*, **64**, 2229 (1976)

Related publication:

Two-dimensional electronic spectroscopy of molecular excitons
F. Milota, J. Sperling, A. Nemeth, T. Mancal, and H. F. Kauffmann
Accounts of Chemical Research, **42**, 1364 (2009)

Historical Perspective

The field of molecular chemical physics has advanced considerably over the past half-century, and a vast part of this knowledge has been gained by probing the response of molecular systems to sequences of pulsed electromagnetic fields. Historically, the associated experimental techniques rapidly evolved for the radio frequency regime of the electromagnetic spectrum. Coherent multi-dimensional spectroscopies, which rely on sequences of pulsed radiation fields with defined phase properties, have thus been developed initially for the interrogation of nuclear magnetic resonances.

Modern nuclear magnetic resonance (NMR) spectroscopy has started around 1950, with the demonstration of the so-called spin-echo (the reversal of inhomogeneous dephasing by a sequence of two pulses) by E. L. Hahn [1]. More than two decades later, following suggestions made by J. Jeener during a conference presentation, R. R. Ernst and co-workers demonstrated a Fourier transform approach for a two-dimensional (2D) version of NMR, and introduced the term *two-dimensional spectrum* for *when all variables of the plotted function are frequencies* [2]. In the ensuing decades, literally hundreds of different pulse sequences have been developed, and have potentiated the capabilities of NMR spectroscopy [3, 4]. Because multi-dimensional NMR techniques allow to sense (through-bond or through-space) coupled spins, nowadays they are not only in routine use by organic chemists for molecular structure analysis, but they also have revolutionized structural biology [4].

In view of the success of 2D-NMR spectroscopy, it has been ever since tantalizing to envisage analogues for the interrogation of spectroscopic transitions that occur at successively higher frequencies of the electromagnetic spectrum. Already in 1957, R. P. Feynman *et al.* pointed out that the theoretical techniques developed for analyzing the magnetic resonance precession model can be adapted to treat any quantum mechanical two-level system [5]. Concepts equivalent to those of NMR would thus also apply to optical transitions - given coherent light fields were to be ever created [5]. Experimentally, 2D microwave spectroscopy for correlating molecular rotational transitions has been realized in the late 1980s [6]. The vision of 2D infrared (IR) spectra that reveal interacting vibrations, or an electronic version of 2D spectroscopy for studying electronic coupling patterns (cf. Fig. 1.1), has driven the implementation of multi-dimensional concepts also at these frequency regimes.

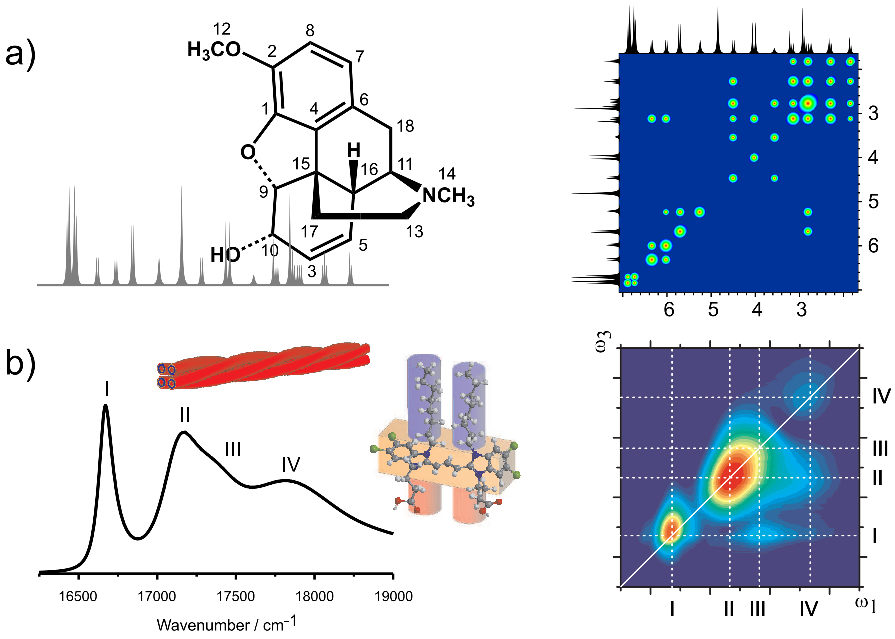

Fig. 1.1: Coherent two-dimensional (2D) spectroscopy illustrated. (a) A 2D spectrum of nuclear magnetic resonances can map the coupling pattern of an ensemble of spin-1/2 systems (here, the H^1-nuclei of Codeine). (b) A 2D electronic spectrum reveals coupling strengths between electronic transitions (absorption bands) of a supramolecular aggregate.

Indeed, very soon after the first report of a pulsed laser light source [7], the optical version of a spin-echo, the photon-echo, has been demonstrated by S. R. Hartmann and co-workers in 1964 [8]. Since then, the technical progress in pulsed laser instrumentation, accompanied by the ongoing development of experimental and theoretical concepts in nonlinear laser spectroscopy [9, 10, 11, 12], has allowed to deepen the understanding of electronic structures and dynamics of molecular systems considerably (as recognized, *inter alia*, by A. H. Zewail's Nobel Prize in 1999, for his studies of the transition states of chemical reactions using femtosecond spectroscopy [13]). However, although a variety pico- and femtosecond time-resolved spectroscopies of vibrational and electronic transitions meanwhile have come of age, the exploitation of coherent pulse sequences has yet not reached a level comparable to that in NMR spectroscopy, and multi-dimensional concepts have been relatively slow to come.

Only within roughly the past decade, after an impressive amount of work in both experiment and theory [14, 15, 16, 17, 18, 19], coherent infrared spectroscopy has been established for providing 2D correlations of vibrations with femtosecond time resolution. The experimental realization of two-dimensional electronic spectroscopy (2D-ES) [20], on the other hand, has been lagging the IR counterparts by several years. The reasons for this delay are commonly summed up by the notion that the required interferometric stability of experimental designs and the precise manipulation of pulse delays become increasingly difficult to achieve at shorter wavelengths. More generally, while real-time detection of electromagnetic fields is straightforward at radio frequencies, there is no such thing like a simple antenna for electric fields at the carrier frequencies of vibrational or electronic transitions. These obstacles have been overcome recently only, and several experimental approaches to generate phase-locked pulse sequences have meanwhile been successfully demonstrated[1]. Notably, all of them share the principle of spectral interferometry for detection of the signal field [21]. The first pioneering experiment on a simple dye molecule [22] has thereby paved the way for experiments devised particularly to unravel electronic interactions. Exemplary highlights in the course of recent developments are investigations of electronic coupling strengths and coherence effects in natural [23, 24, 25] and artificial [26] light harvesting systems, conjugated polymers [27], and the direct observation of biexcitons (bound exciton pairs) in quantum wells [28].

Principles of Two-Dimensional Electronic Spectroscopy

In two-dimensional electronic spectroscopy, a sequence of three laser pulses allows for experimental control of two time intervals: the one between the first and the second (t_1), and the one between the second and the third (t_2) interaction with the sample (cf. Fig. 1.2a). During the third time interval which follows the last excitation pulse (t_3), the created third-order nonlinear polarization radiates the signal $S^{(3)}(t_3, t_2, t_1)$. In principle, given an appropriate experimental scanning scheme, the time domain data might be Fourier transformed with respect to any two (out of the three) time-variables and analyzed as a series of two-dimensional frequency-frequency domain spectra (as a function of the remaining time variable).

The present work focuses on the currently most popular variant of 2D electronic spectroscopy, designated for evaluating signals in the form of $S^{(3)}(\omega_3, t_2, \omega_1)$, i.e. for the measurement of (ω_1, ω_3)-spectra along a more or less coarse grid of t_2-delays. This version of a 2D experiment can be intuitively perceived as a correlation of electronic coherences, that evolve during t_1 and t_3. Accordingly, for the simplest case of an electronic two-level system, the first laser pulse (with wavevector $\mathbf{k_1}$) creates a coherence between the ground- and the excited state. The second pulse ($\mathbf{k_2}$) converts the quantum mechanical superposition into a population (or a vibrational wavepacket), either in the ground- or the excited state. After

---

[1] A detailed and referenced discussion is given Chapter IV.

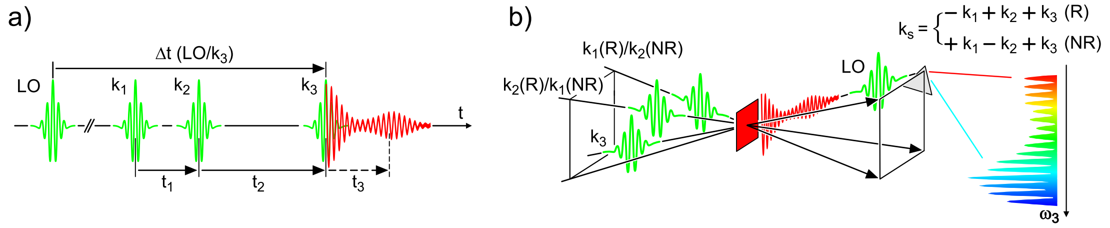

Fig. 1.2: (a) Definition of time-delays in two-dimensional electronic spectroscopy. The sequence of excitation pulses (with wavevectors $\mathbf{k}_1$, $\mathbf{k}_2$, $\mathbf{k}_3$) is preceded by a local oscillator pulse (LO). (b) Spatial wavevector architecture in which rephasing ($\mathbf{k}_s = -\mathbf{k}_1 + \mathbf{k}_2 + \mathbf{k}_3$, denoted by R) and non-rephasing ($\mathbf{k}_s = +\mathbf{k}_1 - \mathbf{k}_2 + \mathbf{k}_3$, NR) signal contributions are collected. Signal detection is accomplished in frequency domain by spectral interference with the LO.

time t_2, again, electronic coherences are created by the third pulse ($\mathbf{k_3}$), and, depending on phase-matching conditions, so-called rephasing or non-rephasing signal contributions are radiated in particular spatial wavevector architectures (cf. Fig. 1.2b).

Though the experimental realization involves a number of hurdles, mapping of the third-order nonlinear response by 2D-ES exploits a number of unique advantages that are inherent to the method. First, it is essential to note that both the real and the imaginary part of the complex nonlinear signal are characterized, gathering the maximum amount of information that can be inferred by any third-order technique [20]. Further, the achievable spectral resolution of a 2D experiment is in practice only limited by the maximal delay between consecutive interactions, while its temporal resolution is given by the accuracy in timing the interaction sequence, i.e., by pulse durations. Unlike other techniques, 2D-ES is therefore not limited by a trade-off between time- and frequency-resolution, which results from the inverse relation between the spectral bandwidth and the temporal duration of the excitation pulses.

Apart from this general characteristics, the spread of the information content into two frequency dimensions considerably facilitates the interpretation of the nonlinear response. A key property of the two-dimensional signal representation can be appreciated by recalling that a 2D plot effectively compares the frequencies of electronic transitions (traced as coherences in t_1 and t_3) against each other. Considering an energetically disordered ensemble of absorbers, the width of the static distribution of transition frequencies (inhomogeneous broadening) will be reflected as a *diagonal* elongation of the 2D signal, as long as each absorber evolves with the same frequency during t_1 and t_3 (cf. Fig. 1.3a). The same effect, in turn, removes static broadening from the *anti-diagonal* width of 2D signal peaks, which allows to discern homogeneous and inhomogeneous line broadening mechanisms. This property is particularly helpful if a strict separation of timescales is not applicable,

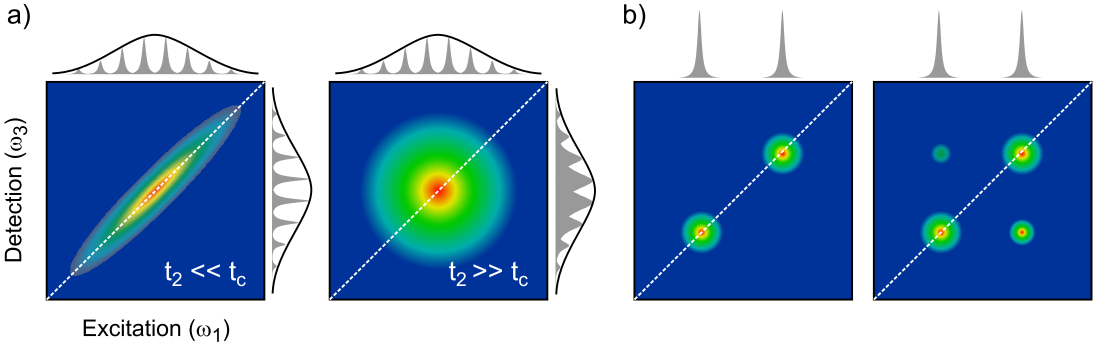

Fig. 1.3: Fundamental effects in 2D electronic spectra. (a) 2D relaxation spectra trace the correlation loss between ω_1- and ω_3-frequencies in a disordered ensemble, reflected by the decreasing ellipticity of the 2D lineshape. (b) Cross-peaks allow to distinguish between uncoupled (left) and coupled (right) absorbers.

as is typically the case in condensed-phase systems, where the transition energies of individual chromophores are continuously altered by their local environments. In this case, the transient loss of the correlation between ω_1- and ω_3-frequencies due to system-bath interactions can be directly monitored by recording 2D spectra for a sequence of increasing t_2-delays. The ellipticity of an initially diagonally elongated peak will thereby steadily decrease, directly reflecting the decay of the frequency-frequency correlation function (cf. Fig. 1.3a).

Whereas the above considerations refer to ensembles of non-interacting absorbers, the full potential of 2D-ES unfolds when interrogating coupled molecular multi-chromophores, in which the close spatial proximity of molecular transition dipoles induces the formation of delocalized excited states (molecular excitons). 2D-ES allows to probe the strengths of electronic inter-molecular interactions in a direct way, by exposing coupled electronic transitions as cross-peaks in the 2D spectrum, and providing information that is not exposed *at all* in linear spectra (cf. Fig. 1.3b). While the appearance of a cross-peak in a 2D correlation plot (recorded at $t_2 = 0$) immediately visualizes electronic couplings, the transient behavior of cross-intensities in 2D relaxation spectra (recorded for $t_2 > 0$) can capture the pathways and timescales of exciton motion even in complex dynamical systems. The perspective to observe and quantify electronic interactions in an unbiased fashion has been one of the main driving forces for pursuing coherent non-linear spectroscopy in two dimensions.

Outline of the Thesis

Two-dimensional electronic spectroscopy is a unique tool for gathering spectral information which either can not be accessed directly or can not be accessed at all by other spectroscopic methods. The content of this thesis is intended to substantiate this statement, presenting studies of molecular samples that can be differentiated by their structural complexity, ranging from simple dye molecules to a supramolecular assembly of coupled molecular absorbers. By combining experimental and theoretical results, it is shown how 2D-ES can image the physical phenomena that are behind the optical response of a particular system.

- The theoretical framework is briefly outlined in Chapter II.
- Chapter III presents a theoretical study on the information content of 2D electronic photon-echo spectra, focusing on their potential to distinguish between different conformations of coupled symmetric dimers.
- Chapter IV describes a passively phase-stabilized experimental set-up, suitable for studies across the entire range of the visible spectrum. Experimental difficulties and evaluation protocols are discussed.
- Chapter V reports and analyzes the oscillatory behavior of lineshapes in 2D relaxation spectra of a perylene-based dye molecule, whose signals are strongly modulated by an underdamped low-frequency vibrational mode.
- In Chapter VI, monomers and van-der-Waals bound dimers of a molecular chromophore are simultaneously monitored in a 2D experiment, illustrating how 2D lineshapes reflect excitation delocalization effects.
- Chapter VII characterizes exciton motion in a self-assembled supramolecular aggregate by temporal, energetic, and spatial attributes, which are inferred from a comparison of experimental 2D spectra to simulations employing both homogeneous and inhomogeneous microscopic models.
- Chapter VIII closes with an outlook on forthcoming developments.

2. THEORETICAL FRAMEWORK

After a brief description of the dynamics of quantum systems, the concept of time-dependent perturbation theory is outlined. The focus is then kept on the sequence of steps towards deriving a perturbative expansion of the density matrix, and the diagrammatic representation of the optical transition pathways that contribute to nonlinear signals. Aspects of the theoretical treatment of multi-chromophoric systems and the incorporation of system-bath interactions are briefly addressed.

2.1 Dynamic Quantum Systems and Perturbation Theory

Time-Dependent Schrödinger Equation. The following considerations start with a *time-independent* Hamiltonian in the Schrödinger-picture (wavefunction picture) [10], where the formal solution of the time-dependent Schrödinger equation[1]

$$\frac{\partial|\Psi(t)\rangle}{\partial t} = -\frac{i}{\hbar}H|\Psi(t)\rangle \tag{2.1}$$

is given by[2]

$$|\Psi(t)\rangle = \mathrm{e}^{-\frac{i}{\hbar}H(t-t_0)}|\Psi_0\rangle \tag{2.2}$$

where $|\Psi_0\rangle \equiv |\Psi(t_0)\rangle$. The solution can be represented using the eigenvalues E_n and eigenvectors $|\phi_n\rangle$ of the stationary Schrödinger equation

$$H|\phi_n\rangle = E_n|\phi_n\rangle \tag{2.3}$$

by expanding $|\Psi(t)\rangle$ in the (complete and orthonormal) basis set of eigenstates $|\phi_n\rangle$

$$|\Psi(t)\rangle = \sum_n \langle\phi_n|\Psi(t)\rangle|\phi_n\rangle \tag{2.4}$$

where $\langle\phi_n|\Psi(t)\rangle$ are the time-dependent expansion coefficients, which can be readily determined. Substituting the above equation into Eq. 2.1 and multiplying with $\langle\phi_n|$ from the left gives

$$\frac{d}{dt}\langle\phi_n|\Psi(t)\rangle = -\frac{i}{\hbar}E_n\langle\phi_n|\Psi(t)\rangle \tag{2.5}$$

with the solution(s)

$$\langle\phi_n|\Psi(t)\rangle = \mathrm{e}^{-\frac{i}{\hbar}E_n(t-t_0)}\langle\phi_n|\Psi_0\rangle \tag{2.6}$$

---

[1] The discussion does not refer to a particular representation. The state vector $|\Psi(t)\rangle$ is related to the wavefunction (representing the state in coordinate representation) via $\Psi(x,t) = \langle\mathbf{x}|\Psi(t)\rangle$, where $\mathbf{x}$ is a complete set of coordinates.

[2] The action of an operator A on one of its eigenfunctions $|\phi_n\rangle$ is defined as $A|\phi_n\rangle = a_n|\phi_n\rangle$, where a_n is the eigenvalue of the operator A. The *function* of an operator (like the exponential on the righthand side of Eq. 2.2) can be defined in a similar way: $f(A)|\phi_n\rangle = f(a_n)|\phi_n\rangle$.

where $\langle\phi_n|\Psi_0\rangle$ are the initial expansion coefficients of the wavefunction. Combining the solution above with Eq. 2.4 gives

$$|\Psi(t)\rangle = \sum_n \mathrm{e}^{-\frac{i}{\hbar}E_n(t-t_0)}\langle\phi_n|\Psi_0\rangle|\phi_n\rangle \tag{2.7}$$

where the superposition of oscillatory terms is determined by oscillations of the expansion coefficients, and is well known as a *wavepacket* from standard textbooks on quantum mechanics. The time-evolution of $|\Psi(t)\rangle$ can also be written in a simple form as

$$|\Psi(t)\rangle \equiv U(t,t_0)|\Psi_0\rangle \tag{2.8}$$

by introducing the time evolution operator $U(t,t_0)$. The specific representation (in terms of eigenstates of the Hamiltonian H, cf. Eq. 2.7)

$$U(t,t_0) = \sum_n |\phi_n\rangle\mathrm{e}^{-\frac{i}{\hbar}E_n(t-t_0)}\langle\phi_n| \tag{2.9}$$

will only be useful if the full set of eigenstates is readily available. In a basis free representation $U(t,t_0)$ is given by (cf. Eq. 2.2)

$$U(t,t_0) = \mathrm{e}^{-\frac{i}{\hbar}H(t-t_0)} \qquad . \tag{2.10}$$

The introduction of $U(t,t_0)$ allows to solve the time evolution in general, since, once $U(t,t_0)$ is obtained, it can act on any initial state $|\Psi_0\rangle$ to get the state at time t. As shown below, the concept of the time evolution operator opens up a convenient approximation scheme for quantum dynamics [10].

Time-Dependent Hamiltonian. So far, the equations hold for a *time-independent* Hamiltonian, which, for dynamic systems, implies the inclusion of all degrees of freedom. However, it is often useful to eliminate some degrees of freedom and treat them as "external" forces. This is the case in time-resolved nonlinear spectroscopy, where it is common to classically approximate the pulsed electromagnetic fields acting on the system.

Generalizing the time evolution operator for a *time-dependent* Hamiltonian $H(t)$ corresponds to a non-perturbative expansion of the wavefunction in the Schrödinger picture. Keeping in mind the time-dependence of the Hamiltonian, substitution of Eq. 2.8 into Eq. 2.1 gives[3]

---

[3] Note that $U(t,t_0) \neq U(t-t_0)$ for a time-dependent Hamiltonian.

$$\frac{\partial}{\partial t}U(t,t_0)|\Psi_0\rangle = -\frac{i}{\hbar}H(t)U(t,t_0)|\Psi_0\rangle \qquad . \tag{2.11}$$

Since this relation must hold for any initial state vector $|\Psi_0\rangle$, $U(t,t_0)$ must satisfy the same equation

$$\frac{\partial}{\partial t}U(t,t_0) = -\frac{i}{\hbar}H(t)U(t,t_0) \tag{2.12}$$

which, upon integration from t_0 to t, and using the relation $U(t_0,t_0) = 1$ yields

$$U(t,t_0) = 1 - \frac{i}{\hbar}\int_{t_0}^{t} \mathrm{d}\tau H(\tau)U(\tau,t_0) \qquad . \tag{2.13}$$

One can solve this equation by iteratively plugging it into itself. The first iteration gives

$$U(t,t_0) = 1 - \frac{i}{\hbar}\int_{t_0}^{t}\mathrm{d}\tau H(\tau) + \left(\frac{i}{\hbar}\right)^2 \int_{t_0}^{t}\mathrm{d}\tau_2 \int_{t_0}^{\tau_2}\mathrm{d}\tau_1 H(\tau_2)H(\tau_1)U(\tau_1,t_0) \qquad . \tag{2.14}$$

Further iteration gives the expression

$$U(t,t_0) = 1 + \sum_{n=1}^{\infty}\left(-\frac{i}{\hbar}\right)^n \int_{t_0}^{t}\mathrm{d}\tau_n \int_{t_0}^{\tau_n}\mathrm{d}\tau_{n-1}\ldots\int_{t_0}^{\tau_2}\mathrm{d}\tau_1 H(\tau_n)H(\tau_{n-1})\ldots H(\tau_1) \tag{2.15}$$

where $U(t,t_0)$ has disappeared on the right hand side. Notably, since the Hamiltonians at different times do not commute, the time variables in the above integral need to be fully ordered (i.e. $t \geq \tau_n \geq \ldots \geq \tau_1 \geq t_0$) [10].

In practice, the above expressions are not very useful. Since the expansion Eq. 2.15 treats the *entire* Hamiltonian perturbatively, it usually applies only for very short times (and breaks down at longer times). Thus, in the following, the time evolution operator is recast in the so-called *interaction picture*, which allows to treat part of the Hamiltonian (H_0) exactly and expand perturbatively only in the remainder of the Hamiltonian ($H'(t)$). Such expansions form the basis of perturbation theory.

Interaction Representation. If the system Hamiltonian $H(t)$ can be decomposed as

$$H(t) = H_0 + H'(t) \tag{2.16}$$

where $H'(t)$ represents a small perturbation of the dynamics given by H_0, a perturbation expansion with respect to $H'(t)$ can be performed. Usually one will attempt to separate $H(t)$ such that the eigenvalue problem of H_0 can be solved analytically, or by means of numerical diagonalization. The time evolution operator with respect to H_0 is then known and given by

$$U_0(t, t_0) = \mathrm{e}^{-\frac{i}{\hbar} H_0 (t - t_0)} \quad . \tag{2.17}$$

Provided such a separation can be made, the time-dependent state vector

$$|\Psi(t)\rangle = U(t, t_0)|\Psi(t_0)\rangle \tag{2.18}$$

can be written as

$$|\Psi(t)\rangle \equiv U_0(t, t_0)|\Psi_I(t)\rangle \tag{2.19}$$

where the subscript I denotes the interaction picture[4]. Note that $|\Psi(t)\rangle$ is the wavefunction under subject of the full Hamiltonian $H(t)$, whereas $U_0(t, t_0)$ is the time evolution operator with respect to the system Hamiltonian H_0 only. Hence, the time dependence of $|\Psi_I(t)\rangle$ describes the time evolution of the wavefunction caused by the difference between $H(t)$ and H_0, i.e. by the perturbation $H'(t)$ [5]. The equation of motion for the state vector in the interaction representation follows from the original time-dependent Schrödinger equation. Substitution of Eq. 2.19 into the Schrödinger equation gives

$$\begin{aligned}
-\frac{i}{\hbar} H(t)|\Psi(t)\rangle &= \frac{\partial |\Psi(t)\rangle}{\partial t} \\
-\frac{i}{\hbar} H(t) U_0(t, t_0)|\Psi_I(t)\rangle &= \frac{\partial}{\partial t} U_0(t, t_0)|\Psi_I(t)\rangle \\
&= \Big(\frac{\partial}{\partial t} U_0(t, t_0)\Big)|\Psi_I(t)\rangle + U_0(t, t_0)\Big(\frac{\partial}{\partial t}|\Psi_I(t)\rangle\Big) \\
&= -\frac{i}{\hbar} H_0 U_0(t, t_0)|\Psi_I(t)\rangle + U_0(t, t_0)\Big(\frac{\partial}{\partial t}|\Psi_I(t)\rangle\Big)
\end{aligned} \tag{2.20}$$

Using the relation $H'(t) = H(t) - H_0$, one obtains

$$-\frac{i}{\hbar} H'(t) U_0(t, t_0)|\Psi_I(t)\rangle = U_0(t, t_0)\Big(\frac{\partial}{\partial t}|\Psi_I(t)\rangle\Big) \quad . \tag{2.21}$$

---

[4] Since $U_0(t_0, t_0) = 1$, it follows from Equ. 2.19 that $|\Psi_I(t_0)\rangle = |\Psi(t_0)\rangle$

[5] In particular, if there is no perturbation, $|\Psi_I(t)\rangle = |\Psi(t_0)\rangle$

Recalling that U_0 is unitary[6], one can now write

$$-\frac{i}{\hbar}U_0^\dagger(t,t_0)H'(t)U_0(t,t_0)|\Psi_I(t)\rangle = \frac{\partial}{\partial t}|\Psi_I(t)\rangle \qquad . \tag{2.22}$$

Defining the weak perturbation in the interaction picture as

$$H'_I(t) = U_0^\dagger(t,t_0)H'(t)U_0(t,t_0) \tag{2.23}$$

one arrives at the equation of motion for the state vector $|\Psi_I(t)\rangle$

$$\frac{\partial}{\partial t}|\Psi_I(t)\rangle = -\frac{i}{\hbar}H'_I(t)|\Psi_I(t)\rangle \qquad . \tag{2.24}$$

Eq. 2.24 is formally equivalent to the Schrödinger equation, and can be solved iteratively along the same lines as outlined in the previous subsection. Introducing the time evolution operator in the interaction representation

$$|\Psi_I(t)\rangle \equiv U_I(t,t_0)|\Psi_I(t_0)\rangle \tag{2.25}$$

one obtains the expression (cf. Eq. 2.15)

$$U_I(t,t_0) = 1 + \sum_{n=1}^{\infty}\left(-\frac{i}{\hbar}\right)^n \int_{t_0}^{t} \mathrm{d}\tau_n \int_{t_0}^{\tau_n} \mathrm{d}\tau_{n-1} \ldots \int_{t_0}^{\tau_2} \mathrm{d}\tau_1 H'_I(\tau_n)H'_I(\tau_{n-1})\ldots H'_I(\tau_1) \qquad . \tag{2.26}$$

To arrive at an expression for $U(t,t_0)$, note that with the above definitions one can write

$$\begin{aligned} |\Psi(t)\rangle &= U_0(t,t_0)|\Psi_I(t)\rangle \\ &= U_0(t,t_0)U_I(t,t_0)|\Psi_I(t_0)\rangle \\ &= U_0(t,t_0)U_I(t,t_0)|\Psi(t_0)\rangle \end{aligned} \tag{2.27}$$

from which follows that

$$U(t,t_0) = U_0(t,t_0)U_I(t,t_0) \qquad . \tag{2.28}$$

Combining Eq. 2.28 and Eq. 2.26 gives

---

[6] $U_0^\dagger(t,t_0) = U_0^{-1}(t,t_0)$

$$U(t,t_0) = U_0(t,t_0) + \sum_{n=1}^{\infty} \left(-\frac{i}{\hbar}\right)^n \int_{t_0}^{t} \mathrm{d}\tau_n \int_{t_0}^{\tau_n} \mathrm{d}\tau_{n-1} \ldots \int_{t_0}^{\tau_2} \mathrm{d}\tau_1 \\ U_0(t,t_0) H_I'(\tau_n) H_I'(\tau_{n-1}) \ldots H_I'(\tau_1) \tag{2.29}$$

Using the relation $U_0(\tau_n,\tau_{n-1}) = U_0(\tau_n,t_0)U_0(t_0,\tau_{n-1}) = U_0(\tau_n,t_0)U_0^\dagger(\tau_{n-1},t_0)$ and writing the interaction Hamiltonian in the Schrödinger picture (cf. also Eq. 2.23), the above equation can be alternatively written as

$$\begin{aligned} U(t,t_0) &= U_0(t,t_0) + \sum_{n=1}^{\infty} \left(-\frac{i}{\hbar}\right)^n \int_{t_0}^{t} \mathrm{d}\tau_n \int_{t_0}^{\tau_n} \mathrm{d}\tau_{n-1} \ldots \int_{t_0}^{\tau_2} \mathrm{d}\tau_1 \\ &\quad U_0(t,\tau_n) H'(\tau_n) U_0(\tau_n,\tau_{n-1}) H'(\tau_{n-1}) \ldots U_0(\tau_2,\tau_1) H'(\tau_1) U_0(\tau_1,t_0) \end{aligned} \tag{2.30}$$

This type of expressions allow for an intuitive physical interpretation and, as will be shown, connects to the diagrammatic representation of the system's evolution in terms of so-called Feynman diagrams [10]. The system propagates freely under the subject of the system Hamiltonian H_0 until time τ_1, described by $U_0(\tau_1,t_0)$. At time τ_1 it interacts with the perturbation $H'(\tau_1)$, propagates again freely until τ_2, interacts with $H'(\tau_2)$, and so on.

Eq. 2.30 at hand, one obtains for the wavefunction in the Schrödinger picture

$$\begin{aligned} |\Psi(t)\rangle &= |\Psi^{(0)}(t)\rangle + \sum_{n=1}^{\infty} \left(-\frac{i}{\hbar}\right)^n \int_{t_0}^{t} \mathrm{d}\tau_n \int_{t_0}^{\tau_n} \mathrm{d}\tau_{n-1} \ldots \int_{t_0}^{\tau_2} \mathrm{d}\tau_1 \\ &\quad U_0(t,\tau_n) H'(\tau_n) U_0(\tau_n,\tau_{n-1}) H'(\tau_{n-1}) \ldots U_0(\tau_2,\tau_1) H'(\tau_1) U_0(\tau_1,t_0) |\Psi(t_0)\rangle \end{aligned} \tag{2.31}$$

where $|\Psi^{(0)}(t)\rangle \equiv U_0(t,t_0)|\Psi(t_0)\rangle$ is the zero-order wavefunction, i.e. the wavefunction without the perturbation $H'(t)$.

2.2 Perturbative Expansion of the Density Matrix and Nonlinear Polarization

Making use of the methodology outlined in the previous section, one can develop a perturbative expansion of the systems's density matrix (for a definition of the density matrix, see Appendix). To this end, the density matrix is defined in the interaction picture

$$|\Psi(t)\rangle\langle\Psi(t)| = U_0(t,t_0)|\Psi_I(t)\rangle\langle\Psi_I(t)|U_0^\dagger(t,t_0) \tag{2.32}$$

or, written alternatively

$$\rho(t) = U_0(t,t_0)\rho_I(t)U_0^\dagger(t,t_0) \qquad . \tag{2.33}$$

Analogous to the time evolution of the wavefunction in the interaction picture $|\Psi_I(t)\rangle$ and its perturbative expansion (cf. Eqs. 2.24, 2.25, and 2.26), one can likewise perturbatively expand the density matrix in the interaction picture $\rho_I(t)$, whose time evolution is governed by

$$\frac{\partial \rho_I(t)}{\partial t} = -\frac{i}{\hbar}[H_I'(t), \rho_I(t)] \tag{2.34}$$

i.e., an expression formally equivalent to the Liouville-von Neumann equation (see Appendix). Accordingly, the perturbative power expansion of $\rho_I(t)$ is given by

$$\begin{aligned} \rho_I(t) = \rho_I(t_0) + \sum_{n=1}^{\infty}\left(-\frac{i}{\hbar}\right)^n \int_{t_0}^{t} \mathrm{d}\tau_n \int_{t_0}^{\tau_n} \mathrm{d}\tau_{n-1} \ldots \int_{t_0}^{\tau_2} \mathrm{d}\tau_1 \\ [H_I'(\tau_n),[H_I'(\tau_{n-1}),\ldots [H_I'(\tau_1),\rho_I(t_0)]\ldots]] \qquad . \end{aligned} \tag{2.35}$$

Going back to the Schrödinger picture yields the expression

$$\begin{aligned} \rho(t) = \rho^{(0)}(t) + \sum_{n=1}^{\infty}\left(-\frac{i}{\hbar}\right)^n \int_{t_0}^{t} \mathrm{d}\tau_n \int_{t_0}^{\tau_n} \mathrm{d}\tau_{n-1} \ldots \int_{t_0}^{\tau_2} \mathrm{d}\tau_1 \\ U_0(t,t_0)\cdot[H_I'(\tau_n),[H_I'(\tau_{n-1}),\ldots [H_I'(\tau_1),\rho(t_0)]\ldots]]\cdot U_0^\dagger(t,t_0) \qquad . \end{aligned} \tag{2.36}$$

The interaction Hamiltonian in the equations above contains both the perturbation $H'(t)$ and the time evolution operators (cf. Eq. 2.23). Since the density matrix contains a ket and a bra, it can act on $H_I'(t)$ either from the left or from the right.

In a next step, one can proceed and specify the perturbation as

$$H'(t) = E(\mathbf{r},t)\cdot\mu \tag{2.37}$$

where $E(\mathbf{r},t)$ is the electric field and μ is the (time-independent) dipole operator in the Schrödinger picture. The electric field can be written as summation over all incoming fields

$$E(\mathbf{r},t) = \sum_j \left(E_j(t)\mathrm{e}^{-i\omega_j t + i\mathbf{k}_j\mathbf{r}} + E_j^*(t)\mathrm{e}^{i\omega_j t - i\mathbf{k}_j\mathbf{r}}\right) \tag{2.38}$$

where $E_j(t)$ respectively $E_j^*(t)$ denote the temporal field envelopes. Rewriting Eq. 2.36

one thus obtains[7]

$$\rho(t) = \rho^{(0)}(-\infty) + \sum_{n=1}^{\infty} \rho^{(n)}(t) \tag{2.39}$$

with the nth-order density matrix elements given by

$$\begin{aligned}\rho^{(n)}(t) = \left(-\frac{i}{\hbar}\right)^n \int_{-\infty}^{t} \mathrm{d}\tau_n \int_{-\infty}^{\tau_n} \mathrm{d}\tau_{n-1} \ldots \int_{-\infty}^{\tau_2} \mathrm{d}\tau_1 E(\tau_n) E(\tau_{n-1}) \ldots E(\tau_1) \\ U_0(t,t_0) \cdot [\mu_I(\tau_n), [\mu_I(\tau_{n-1}), \ldots [\mu_I(\tau_1), \rho(-\infty)] \ldots]] \cdot U_0^\dagger(t,t_0)\end{aligned} \tag{2.40}$$

and the dipole operator in the interaction picture defined as

$$\mu_I(t) = U_0^\dagger(t,t_0) \mu U_0(t,t_0) \qquad . \tag{2.41}$$

The expectation value of the nth-order polarization, which is the observable in any experiment, is given by (see Appendix) [10]

$$P^{(n)}(t) = \langle \mu \rho^{(n)}(t) \rangle \qquad . \tag{2.42}$$

Thus, inserting Eq. 2.40 into the above equation and making use of Eq. 2.41, one obtains

$$\begin{aligned}P^{(n)}(t) = \left(-\frac{i}{\hbar}\right)^n \int_{-\infty}^{t} \mathrm{d}\tau_n \int_{-\infty}^{\tau_n} \mathrm{d}\tau_{n-1} \ldots \int_{-\infty}^{\tau_2} \mathrm{d}\tau_1 E(\tau_n) E(\tau_{n-1}) \ldots E(\tau_1) \\ \langle \mu_I(t) \cdot [\mu_I(\tau_n), [\mu_I(\tau_{n-1}), \ldots [\mu_I(\tau_1), \rho(-\infty)] \ldots]] \rangle \qquad .\end{aligned} \tag{2.43}$$

Finally, by performing a transformation of the time variables (replacing the absolute time points τ_n with time intervals t_n) [10], one arrives at the expression for the nth-order polarization

$$\begin{aligned}P^{(n)}(t) = \left(-\frac{i}{\hbar}\right)^n \int_{0}^{\infty} \mathrm{d}t_n \int_{0}^{\infty} \mathrm{d}t_{n-1} \ldots \int_{0}^{\infty} \mathrm{d}t_1 \\ E(t-t_n) E(t-t_n-t_{n-1}) \ldots E(t-t_n-t_{n-1}-\ldots-t_1) \\ \langle \mu_I(t_n+t_{n-1}+\ldots+t_1) \cdot [\mu_I(t_{n-1}+\ldots+t_1), \ldots [\mu_I(0), \rho(-\infty)] \ldots] \rangle\end{aligned} \tag{2.44}$$

which can be rewritten as a convolution of n electric fields

---

[7] Assuming $\rho(t_0)$ to be an equilibrium density matrix that does not evolve in time under subject of H_0, one can send $t_0 \rightarrow -\infty$, as done in Eq. 2.39 and Eq. 2.40.

$$\begin{aligned} P^{(n)}(t) = &\int_0^\infty \mathrm{d}t_n \int_0^\infty \mathrm{d}t_{n-1} \dots \int_0^\infty \mathrm{d}t_1 \\ &E(t-t_n)E(t-t_n-t_{n-1})\dots E(t-t_n-t_{n-1}-\dots-t_1) \cdot S^{(n)}(t_n, t_{n-1}, \dots, t_1) \end{aligned} \tag{2.45}$$

with the nth-order nonlinear response function

$$S^{(n)}(t_n, \dots, t_1) = \left(-\frac{i}{\hbar}\right)^n \langle \mu_I(t_n + \dots + t_1) \cdot [\mu_I(t_{n-1} + \dots + t_1), \dots [\mu_I(0), \rho(-\infty)] \dots] \rangle \tag{2.46}$$

In the above expression, the interactions in the commutators generate a non-equilibrium density matrix $\rho^{(n)}$, whose off-diagonal elements emit a light field at time $t_n + \dots + t_1$. Note that only the first n interactions are part of the commutators, while the last is not. Writing down explicitly the commutator of a nth-order response function, one obtains a set of 2^n terms (pathways), each with various numbers of interactions on the left (on the ket) respectively on the right (on the bra) of the density matrix. Since the entire set of terms can be grouped into pairs that are complex conjugates of each other, one is left with an expression that contains 2^{n-1} independent terms.

Is should be further mentioned that the form of Eq. 2.46 guarantees that the response functions are real (as they relate two real quantities, the electric field and the polarization) [10]. However, individual contributions (pathways) to the response function are complex. Thus, once a particular wavevector is chosen for the signal in order to select particular contributions, the relevant polarization becomes complex (see discussion below).

2.3 Modeling the Nonlinear Response of Excitonic Systems

The considerations outlined so far do not relate explicitly to a particular scheme of electronic levels, and the molecular systems covered within this work are to be discussed on an individual basis. However, as the interrelation between electronic and optical properties of excitonic systems is a central issue throughout most of the remaining chapters, some general aspects of modeling the nonlinear optical response of molecular multi-chromophores are outlined in the following.

Fortunately, a theoretical description of electronic excitations of molecular assemblies becomes considerably simplified if non-overlapping charge distributions can be assumed (which applies for the systems studied here). The excitations are then known as Frenkel

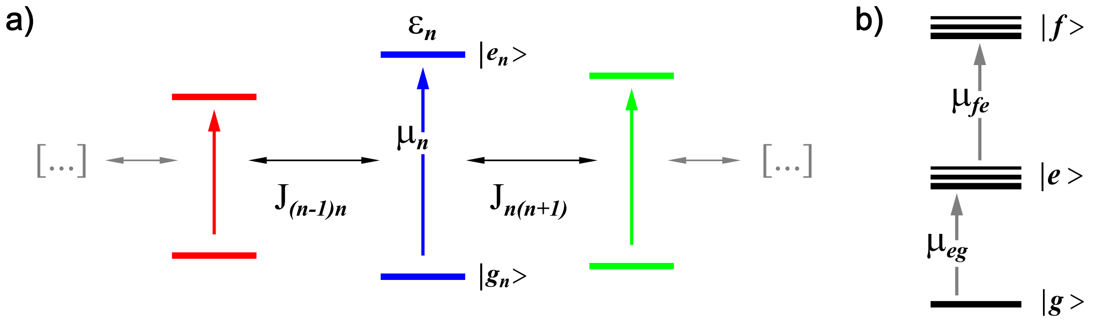

Fig. 2.1: (a) Assembly of molecular sites with individual coupling strengths (J) and site-transition energies (ε); μ_n indicates a transition dipole moment in the local basis. (b) Level scheme and (schematically indicated) transition dipoles in the excitonic basis. The energy spectrum consists of well-separated groups of energy levels, representing single ($|e\rangle$) and double excitations ($|f\rangle$).

excitons, and their localization and energy-transfer dynamics have been extensively studied using the Frenkel exciton Hamiltonian, whose parameters are closely related to the electronic structure of the individual chromophores [29, 30]. In the Frenkel exciton picture of multi-chromophoric systems (cf. Fig. 2.1), excitations can occur at molecular sites ($n = 1, \ldots, N$) with individual site transition energies ε_n and inter-site couplings J_{mn}. For the one-exciton manifold, the Frenkel exciton Hamiltonian is given by

$$H_s = \sum_n \varepsilon_n |n\rangle\langle n| + \sum_m \sum_{n\neq m} J_{mn}|m\rangle\langle n| \qquad . \tag{2.47}$$

The electronic eigenstates of the system can be obtained by diagonalization of the above matrix. Their spatial characteristics may vary from site-localized states (if the energetic width of the distribution of transition frequencies is larger than typical couplings) to delocalized ones (if coupling terms become dominant over the variation of transition frequencies). The two-exciton manifold, in turn, comprises the highest accessible states in (conventional) 2D electronic spectroscopy, and involves simultaneous excitation of different sites ($m \neq n$). A thorough discussion of the construction of the respective Hamiltonian is beyond the scope in the present context [31].

Since the studies described here deal with condensed phase systems, molecular properties have generally to be assumed to be fluctuating; in other words, energy levels and other intramolecular quantities become time dependent, which necessitates a theoretical description of the system-bath coupling. The population and phase relaxation processes, induced by a fluctuating environment (may it be solvent modes or intramolecular modes), result in line-broadenings and spectral shifts, directly impacting multidimensional signals. While such bath effects may be incorporated by simply "adding" (phenomenological) relaxation rates (as is done, in fact, in Chapter III of this theses), it is common to involve semiclassical treatments of bath degrees of freedom by using correlation function time-domain methods.

Generally, the coupling of an excitonic system to a bath will induce time-dependent fluctuations $Q_{mn}(t)$ in all matrix elements of the total Hamiltonian, represented by the system-bath coupling Hamiltonian

$$H_{sb} = \sum_m \sum_n Q_{mn}(t)|m\rangle\langle n| \qquad . \tag{2.48}$$

Since purely stochastic models of fluctuations do not account for dissipation [32, 33], for electronic transitions, most frequently a microscopic description of the bath is applied. The widely used multimode Brownian oscillator (BO) model provides closed expressions for the optical response of two-level systems [34, 35, 10]. Therein, fluctuations are related to the collective coordinate of a BO, whose equilibrium position is displaced in the excited electronic state, and which experiences the (random) influence of the remaining bath coordinates during propagation. Within the BO model, the ensemble averaged fluctuation-correlation functions

$$C_{klmn}(\tau) = \langle Q_{kl}(t+\tau)Q_{mn}(t)\rangle \tag{2.49}$$

carry in principle all relevant information on bath fluctuations[8]. A large number of phenomenological models commonly used in nonlinear optics, e.g. stochastic models, homogeneous Lorentzian, and inhomogeneous Gaussian line broadening can be obtained as limiting cases of the BO model. It therefore provides an unifying framework for the analysis of optical response functions. After adequate transformation of the matrix elements $Q_{mn}(t)$, i.e. in the electronic eigenstate representation, diagonal exciton-phonon coupling leads to the decay of coherences (pure dephasing), while off-diagonal elements induce a population redistribution within the excitonic states. It should be mentioned that only the diagonal part of the system-bath coupling can be treated exactly (for Gaussian fluctuations) [10, 30]. Exciton relaxation effects in assemblies of electronic chromophores (effects of off-diagonal fluctuations), on the other hand, are commonly accounted for within the framework of Redfield theory or extensions thereof [36, 37, 38, 39].

Given the excitonic level positions (transition frequencies) and their linewidths (relaxation rates) have been determined, the nonlinear optical response of the system under study can be calculated on the basis of the 3^{rd}-order response function (cf. Eq. 2.46)

---

[8] For multi-chromophores, the relevant number of such expressions reduces significantly if fluctuations of couplings $Q_{mn}(t)$ can be neglected (H_{sb} can be assumed to be diagonal in the site representation), and/or fluctuations at different chromophores are statistically independent, i.e. $C_{mmnn}(\tau) = \delta_{mn}\langle Q_{mm}(t+\tau)Q_{nn}(t)\rangle$.

$$S^{(3)}(t_3,t_2,t_1) = \left(-\frac{i}{\hbar}\right)^3 \langle \mu_I(t_3+t_2+t_1)\cdot[\mu_I(t_2+t_1)[\mu_I(t_1)[\mu_I(0),\rho(-\infty)]]]\rangle \quad . \tag{2.50}$$

Note that, since the experiments to be presented involve three laser pulses, the expression for the electric field (cf. Eq. 2.38)

$$E(\mathbf{r},t) = \sum_{j=1}^{3}\big(E_j(t)\mathrm{e}^{-i\omega_j t+i\mathbf{k}_j\mathbf{r}} + E_j^*(t)\mathrm{e}^{i\omega_j t-i\mathbf{k}_j\mathbf{r}}\big) \tag{2.51}$$

contains six terms. As a result, already for a two-level system, the integrand

$$\begin{aligned} P^{(3)}(t) = &\int_0^\infty \mathrm{d}t_3 \int_0^\infty \mathrm{d}t_2 \int_0^\infty \mathrm{d}t_1 \\ &E(t-t_3)E(t-t_3-t_2)E(t-t_3-t_2-t_1)\cdot S^{(3)}(t_3,t_2,t_1) \end{aligned} \tag{2.52}$$

which needs to be evaluated when calculating the nonlinear polarization, contains a total of $6\cdot 6\cdot 6\cdot 2^{3-1} = 864$ terms, which arise from convolving the systems's nonlinear response function with the electric field. Fortunately, the number of terms that are relevant for comparing calculated and experimental data can be reduced considerably [10].

First, if the temporal envelopes $E_j(t)$ of the laser pulses are shorter then the typical time separations between them, one can neglect pulse overlap effects and assume strict time ordering. It is further common to perform calculations in the so-called semi-impulsive limit, assuming the laser pulses to be short compared with any timescale of the material system, but still long compared to optical periods. The temporal envelopes of the pulses are then replaced by δ-functions, while keeping the assigned carrier frequencies and wavevectors (assumption of "physical" δ-functions). Each pulse then enters with a term containing either $e^{-i\omega t}$ or $e^{i\omega t}$ (and the associated wavevector) into Eq. 2.52. This allows, in turn, to employ the rotating wave approximation (RWA), which relies on the fact that integrals of highly oscillating functions vanish (given the "functional envelope" does not change significantly during an oscillation period). Simply speaking, the RWA is a way to select only resonant terms in $S^{(3)}(t_3,t_2,t_1)$, where the optical frequency is canceled by a material frequency of opposite sign. It is valid near resonance conditions and if the envelope of the electric field is slowly varying in time (compared to the pulse carrier frequency). Given the RWA is applicable, and recalling that each threefold product of electric fields in Eq. 2.52 carries a wavevector $\mathbf{k_s} = \pm\mathbf{k}_1 \pm \mathbf{k}_2 \pm \mathbf{k}_3$, the number of relevant terms is further reduced due to a non-collinear wavevector architecture in the experiment. Depending on the choice of

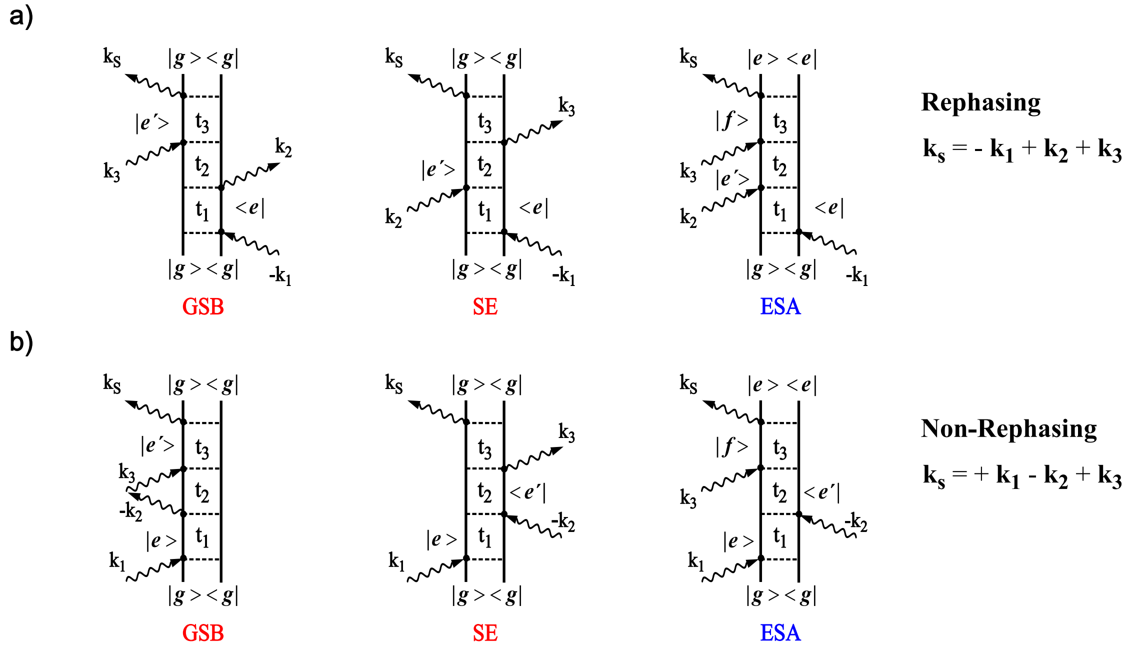

Fig. 2.2: Double-sided Feynman diagrams representing the evolution of the density matrix during the pathways that contribute to the third order response of a molecular aggregates (in the rotating wave approximation). Shown are the signal directions (a) $\mathbf{k}_s = -\mathbf{k}_1 + \mathbf{k}_2 + \mathbf{k}_3$ and (b) $\mathbf{k}_s = +\mathbf{k}_1 - \mathbf{k}_2 + \mathbf{k}_3$, which can be distinguished as rephasing respectively non-rephasing contributions. In each diagram, the left (right) vertical line denotes the time evolution of the ket (bra) of the density matrix, time is running from bottom to top. Interactions with the light field are represented by arrows. An arrow pointing towards the diagram represents energetic up-climbing on the corresponding side of the density matrix, an arrow pointing away represents a de-excitation. The diagrams can be classified as ground state bleach (GSB), stimulated emission (SE), and excited state absorption (ESA) contributions, respectively, giving rise to positive (GSB, SE) and negative (ESA) absorptive signals. After the first two interactions, i.e. during t_2, the system evolves either in the ground state (GSB), or in the one-exciton manifold (SE and ESA). Note that in the latter case, population and/or coherence transfer may lead to new pathways. The third interaction takes the system again into a one-exciton coherence (GSB, SE), or, alternatively, into a coherence between a one- and a two-exciton state (ESA).

$\mathbf{k}_s$, only a handful of terms in $S^{(3)}(t_3, t_2, t_1)$ usually survives the RWA and needs to be considered for the calculation of $P^{(3)}(t)$.

This chapter closes with presenting the Liouville-space pathways that contribute to the third-order response of a molecular aggregate (level scheme Fig. 2.1b) in the rotating wave approximation. Fig. 2.2 shows the so-called double sided Feynman diagrams for the signal directions $\mathbf{k_s} = -\mathbf{k}_1 + \mathbf{k}_2 + \mathbf{k}_3$ respectively $\mathbf{k_s} = +\mathbf{k}_1 - \mathbf{k}_2 + \mathbf{k}_3$. The rules governing this type of diagrammatic representation are outlined in the figure caption. This type of presentation is intimately linked to Eq. 2.50. The illustrated pathways form the interpretational basis for simulations and experiments described in the forthcoming chapters.

APPENDIX

Expanding $|\Psi(t)\rangle$ in a basis $|n\rangle$ one obtains

$$|\Psi(t)\rangle = \sum_n c_n(t)|n\rangle \tag{2.53}$$

respectively

$$\langle\Psi(t)| = \sum_n c_n^*(t)\langle n| \tag{2.54}$$

for the Hermitian conjugate [10]. The density matrix $\rho(t)$ of a pure quantum state is defined as

$$\rho(t) \equiv |\Psi(t)\rangle\langle\Psi(t)| = \sum_{n,m} c_n(t)c_m^*(t)|n\rangle\langle m| \tag{2.55}$$

with matrix elements

$$\rho_{nm}(t) \equiv \langle n|\rho(t)|m\rangle = c_n(t)c_m^*(t) \qquad . \tag{2.56}$$

The expectation value of an operator A in the density matrix picture is given by

$$\langle A(t)\rangle = \langle\Psi(t)|A|\Psi(t)\rangle = \sum_{nm} c_n(t)c_m^*(t)A_{nm} = \mathrm{Tr}[\rho(t)A] \qquad . \tag{2.57}$$

The equation of motion for the density operator is given by the time-evolution of the ket and the bra

$$\frac{\partial\rho(t)}{\partial t} = \frac{\partial|\Psi(t)\rangle}{\partial t}\langle\Psi(t)| + |\Psi(t)\rangle\frac{\partial\langle\Psi(t)|}{\partial t} = -\frac{i}{\hbar}[H,\rho] \qquad . \tag{2.58}$$

This equation is known as the Liouville-von Neumann equation, written in Hilbert space [10]. In condensed phase systems, one generally deals with statistical ensambles, rather than pure states. While there is no way to write a wavefunction of a statistical average, one can write the density matrix of a statistical average. Let P_k be the probability of a system being in a pure state $|\Psi_k(t)\rangle$, then the density matrix is defined as

$$\rho(t) = \sum_k P_k|\Psi_k(t)\rangle\langle\Psi_k(t)| \qquad . \tag{2.59}$$

If the system can be represented by a wavefunction, it is in a pure state, and all P_k's are 0, except for one which is 1. Otherwise the system is in a mixed state and has to be represented by $\rho(t)$.

3. TWO-DIMENSIONAL SPECTRA OF SYMMETRIC DIMERS - A THEORETICAL STUDY

An exemplary theoretical study on the information content of two-dimensional photon-echo spectra is presented, focusing on their potential to distinguish between different conformations of electronically coupled symmetric dimers. The analysis is performed on the basis of an analytical formula for the frequency-domain signal. The dimers are modeled in terms of two identical, energy-degenerate, excitonically coupled pairs of electronic states in the site-representation. The spectra of conformationally weighted ensembles, composed of either two or four dimers, are compared with their one-dimensional linear absorption counterparts. In order to provide a realistic coupling pattern for the ensemble consisting of four dimers, excitonic couplings are estimated on the basis of optimized geometries and site-transition dipole moments, calculated by standard semiempirical methods for a bridged bithiophene structure. In the framework of the model, the highly readable two-dimensional spectra allow to unambiguously identify spectral doublets, by relating peak heights and positions to mutual orientations of site-localized transition dipoles.

Related publication:

Two-dimensional electronic spectra of symmetric dimers: Intermolecular coupling and conformational states
V. Szöcs, T. Pálszegi, V. Lukeš, J. Sperling, F. Milota, W. Jakubetz, and H. F. Kauffmann
Journal of Chemical Physics, **124**, 124511 (2006)

3.1 Introduction

The information provided by conventional one-dimensional (1D) spectroscopies is limited by the projection onto a single frequency-axis. This complicates the separation of operative line-broadening mechanisms and studies on chromophore-chromophore interactions, particularly in studies carried out in condensed phases. Time-resolved multi-dimensional (nD) spectroscopies, on the other hand, hold great potential to identify correlations of electronic transitions by spreading congested spectra into two (or more) frequency dimensions that correspond to specific time-intervals of a pulse sequence. In the present chapter, in a lowest order approach to tackle electronically interacting molecular units, heterodyne detected photon-echo (PE) signals of energy-degenerate symmetric dimers (SDs) are analyzed. Comprising the simplest case of a polychromophoric assembly, the SDs under consideration are modeled in terms of two identical, excitonically coupled pairs of electronic states in the site-representation. The resonant, purely electronic inter-site coupling is assumed to be mediated by the interaction of (site-)transition dipole moments, which is a useful approximation in the absence of direct inter-chromophoric orbital overlap. The method has been developed keeping an eye on the treatment of the coherent dynamics of the "bottom states" in the density-of-states of conjugated polymers [40, 41], for which the model of non-interacting excitonic two-site conformational systems is a reasonable choice - even though the present model assumptions may not hold in terms of a fully quantitative description.

This study continues previous work [42], where, by numerical Fourier inversion of the time-domain PE-signal of inhomogeneously broadened (but otherwise identical) dimers, the essential features of electronic two-dimensional (2D) correlation spectra have been analyzed in frequency-frequency space. Here, the probability information content of electronic 2D-PE and 1D linear absorption (LA) spectra of discrete conformational distributions of SDs (with individual coupling strengths and transition dipole orientations) is compared in detail. This task is accomplished on the basis of an analytic expression for the 2D-PE signal in frequency-frequency space at waiting time zero ($T = 0$)[1]. It is this configuration of the 3-pulse PE experiment (where the second and third pulses coincide), that contains the required spectroscopic information, taking the classical tasks of absorption spectroscopy to new levels of resolution. More advanced possibilities are connected with waiting-time resolved 3-pulse PE spectroscopy [30, 43, 23, 39, 44, 45] through its direct access to energy transfer between coupled chromophores.

---

[1] Throughout this chapter τ_{12}, T, and t' refer to time intervals that are otherwise denoted as t_1, t_2, and t_3, respectively.

The chapter is organized as follows. In Section 3.2, a brief outline of the model is given, the 2D-PE spectra of symmetric dimers are discussed, and analytic formulas for the signals in 2D frequency-frequency space are derived. Section 3.3 turns to the corresponding electronic linear absorption (LA) spectra, again providing analytic formulas for the signals. In two case studies described in Section 3.4, spectra of statistical distributions formed by two and four bichromophores, respectively, are compared. For the SD-pair, it is shown how the information content of PE spectra in frequency-frequency space can be used for the identification of SD doublets in a blurred linear absorption spectrum. In the case of four SDs, using realistic estimates on excitonic couplings obtained from optimized geometries and semiempirical calculations on a bridged bithiophene-structure, a multiplet is deciphered, which, for the same parameters of spectral broadening, is hidden in the congested LA spectrum. The chapter closes with a summary and conclusions addressing the limitations of the model.

3.2 Two-Dimensional Photon-Echo Spectra

Outline of the Model. The calculation of the time-domain 2D-PE signal for a single resonantly coupled SD is discussed in detail in Ref. [42]. For the sake of completeness, the most relevant steps are outlined briefly in the following, before turning to the analytically derived expression for the the heterodyned 2D-PE signal of a SD in frequency-frequency space.

The electronic site-subsystem of a specific SD is described by its electronic ground state $|g_i\rangle$ and its first excited state $|e_i\rangle$, with equal transition frequency ω_{eg} for both sites forming the SD (see Fig.3.1). The Hilbert space of the SD's electronic states consists of the ground state $|G\rangle = |g_{\mathrm{I}}\rangle|g_{\mathrm{II}}\rangle$, a subspace of two one-exciton states $|E_1\rangle = \{|g_{\mathrm{I}}\rangle|e_{\mathrm{II}}\rangle, |e_{\mathrm{I}}\rangle|g_{\mathrm{II}}\rangle\}$, and a two-exciton state $|E_2\rangle = |e_{\mathrm{I}}\rangle|e_{\mathrm{II}}\rangle$, the latter comprising a pair of site-localized excitations (different from one-electron, delocalized Frenkel excitons). In the interaction Hamiltonian, each site is represented by its electronic states $|g_i\rangle$ and $|e_i\rangle$ and by the corresponding basis of intramolecular vibrational states. The resonant dipole-dipole inter-site coupling of magnitude J, which is assumed to be factorized from nuclear vibrational motions, depends on the inter-site distance. Its effective component is determined by the angle θ between the

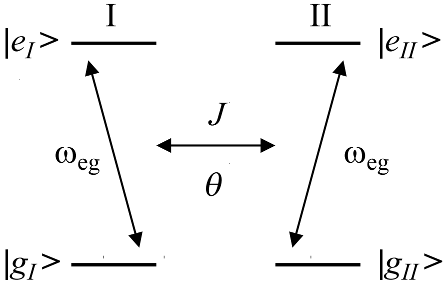

Fig. 3.1: Two-site, four-level excitonic system in the adiabiatic approximation, showing schematically the intersite coupling of magnitude J and the site transition dipole angle θ determining the effective coupling.

site transition dipole moments $\mathbf{d}_{\mathrm{I}}$ and $\mathbf{d}_{\mathrm{II}}$ of equal magnitude $d = |\mathbf{d}_{\mathrm{I}}| = |\mathbf{d}_{\mathrm{II}}|$. Assuming site-localized vibrations, the total energy of a dimer is obtained by adding the corresponding vibrational Hamiltonians to those for the electronic states. Overall, the interaction causing delocalization and resonant transfer of excitation energy between the sites will be determined by the stable conformation geometry in a local free energy minimum, and the extent of coupling determines the energy splitting between the electronically excited states of the system.

The 3-pulse PE sequence consists of three pulses with time delay τ_{12} between the first and second pulse and waiting time (or population time) T between the second and the third pulse, with $T = 0$ (coinciding or degenerate pulses 2 and 3) representing the limit of zero waiting time. The coherence time after the third pulse, when the echo is built up, is denoted t', so that the total time elapsed (t) is given $t = \tau_{12} + T + t'$. With the assumptions outlined above, the time-domain PE signal of a SD can be derived [42] for resonant δ-pulse excitation by propagation of the density operator in Liouville space [10]. Accordingly, in an ensemble of randomly oriented, but otherwise identical dimers, at $T = 0$ the PE sequence generates the 3^{rd}-order polarization[2]

$$P^{(3)}(\tau_{12}, t') = iK \exp(i\omega_L t)\ \exp(-t/T_2)\ \exp(-\sigma^2(t'-\tau_{12})^2/2)\ R_\delta(\tau_{12}, t') + c.c. \quad . \quad (3.1)$$

Here, *c.c.* stands for complex conjugate, K is a constant that results from the signal phase-matching condition $\mathbf{k}_{\mathrm{S}} = -\mathbf{k}_1 + \mathbf{k}_2 + \mathbf{k}_3$, which at $T = 0$ simplifies to $\mathbf{k}_{\mathrm{S}} = -\mathbf{k}_1 + 2\mathbf{k}_2$ ($\mathbf{k}_n$ is the wave-vector of the vertically polarized n^{th} electric field pulse), and ω_L is the carrier frequency of the δ-pulses. The parameters $1/T_2$ and σ describe the homogeneous dephasing of coherence due to unspecified system-bath interactions, and the width of the inhomogeneous (static) distribution of transition energies, respectively. Note that, following the convention introduced above ($\hbar = 1$), $1/T_2$ and σ are given in energy units, so that the ratio of homogeneous (HLB) to inhomogeneous line-broadening (IHLB), HLB/IHLB= $T_2^{-1}\sigma^{-1}$, becomes dimensionless.

---

[2] The convention $\hbar = 1$ is used throughout this chapter.

As discernible from the exponential prefactors in Eq. 3.1, the overall decay of $P^{(3)}$ is determined by the rate $1/T_2$, while the contribution due to rephasing reaches its maximum at time $t' = \tau_{12}$ (formation of the "true echo"). In the above expression, the response function to δ-pulse excitation $R_\delta(\tau_{12}, t')$ is composed of two four-point dipole correlation functions

$$R_\delta(\tau_{12}, t') = 2F_{E_1}(\tau_{12}, \tau_{12} + t', \tau_{12}, 0) - F_{E_2}(\tau_{12}, \tau_{12}, \tau_{12} + t', 0) \tag{3.2}$$

which are given by four-point correlation functions of coupled SDs [42],

$$\begin{aligned} F_{E_1}(t_1, t_2, t_3, t_4) &= \langle \mathbf{d}_{GE_1}(t_1)\; \mathbf{d}_{E_1G}(t_2)\; \mathbf{d}_{GE_1}(t_3)\; \mathbf{d}_{E_1G}(t_4) \rangle & (3.3) \\ F_{E_2}(t_1, t_2, t_3, t_4) &= \langle \mathbf{d}_{GE_1}(t_1)\; \mathbf{d}_{E_1E_2}(t_2)\; \mathbf{d}_{E_2E_1}(t_3)\; \mathbf{d}_{E_1G}(t_4) \rangle \quad . & (3.4) \end{aligned}$$

Since the weak inter-site coupling J is assumed to be independent of vibrations, F_{E_1} and F_{E_2} can be decomposed into excitation transfer (ET) and vibrational (ν) parts, which depend on the coupling J respectively on the vibrational Hamiltonians [42]. For appropriate time-ordering, F_{E_1} equals the one-particle response functions $R^*_{2(3)}(t', 0, \tau_{12})$ of a two-level system (TLS) in the well-known formalism developed by Mukamel and co-workers [10], while F_{E_2} has no simple one-particle counterpart. The four point dipole correlation functions contain the electronic coupling term J and explicitly read [42]

$$\begin{aligned} F_{E_1}(\tau_{12}, \tau_{12} + t', \tau_{12}, 0) &= |d|^4\,(4/5)\{\sin^4\theta\exp(-iJt_-) + \cos^4\theta\exp(iJt_-)\} + \\ &\quad\; |d|^4\,(2/15)\sin^2\theta\,\{\exp(-iJt_+) + \exp(iJt_+)\} \qquad (3.5) \\ F_{E_2}(\tau_{12}, \tau_{12}, \tau_{12} + t', 0) &= (2/15)\,\{(2 + 3\cos\theta + \cos 2\theta)\exp(-iJt_+) + \\ &\quad\; (2 - 3\cos\theta + \cos 2\theta)\exp(iJt_+)\} \end{aligned}$$

where the notation $t_\pm = t' \pm \tau_{12}$ has been introduced.

The method of heterodyne-detection relies on mixing the signal with a local oscillator field, for which a δ-pulse shape, a carrier frequency equal to the excitation frequency ω_L, and zero relative phase shift with respect to the phase of the signal field are assumed. The time-domain 2D-PE signal $S(\tau_{12}, t')$ is then simply proportional to the signal polarization given in Eq. 3.1,

$$S(\tau_{12}, t') \propto P^{(3)}(\tau_{12}, t') \quad . \tag{3.6}$$

One is now interested in the analytical form of the corresponding double Fourier transform of $S(\tau_{12}, t')$, which allows to switch to the undoubtedly more informative signal representation in frequency-frequency space, i.e. in the derivation of

$$S(\omega_{\tau_{12}}, \omega_{t'}) = \int_0^\infty \int_0^\infty \exp(i\omega_{t'} t') \exp(i\omega_{\tau_{12}} \tau_{12}) S(\tau_{12}, t') dt' d\tau_{12} \qquad . \tag{3.7}$$

The 2D Photon-Echo Signal. In previous work, analytical results for $S(\omega_{\tau_{12}}, \omega_{t'})$ have been given only for the two simple special cases of parallel ($\theta = 0$) and perpendicular ($\theta = \pi/2$) orientations of transition dipoles, for which $P^{(3)}(\tau_{12}, t')$ simplifies considerably [42]. Here, inserting Eqs. 3.6 and 3.1 into Eq. 3.7 results in a tedious expression, whose numerator consists of a lengthy sum of exponentials, with exponents that can be written as quadratic polynomials in $(\omega_{t'} - \omega_{\tau_{12}})/2$, ω_L, J, $1/T_2$, and θ. Exploiting the fact that exponentials with imaginary exponents involve multiples of θ, and applying the Euler formula and subsequently the sum rules for polynomials in $\sin(n\theta)$ and $\cos(n\theta)$, the numerator can be simplified considerably. After some rearrangements, a compact and instructive formula can be obtained for the heterodyned PE signal of a SD in frequency-frequency space:

$$\begin{aligned} S(\omega_d, \omega_a) = \quad & \frac{(1-\cos\theta)^2}{2(T_2^{-1} - i\omega_a)} \left[e^{-(\omega_d + J)^2/2\sigma^2} + e^{-(\omega_d - J - 2\omega_L)^2/2\sigma^2} \right] \\ & + \frac{(1+\cos\theta)^2}{2(T_2^{-1} - i\omega_a)} \left[e^{-(\omega_d - J)^2/2\sigma^2} + e^{-(\omega_d + J - 2\omega_L)^2/2\sigma^2} \right] \\ & + \frac{i\cos\theta}{J^2 + \left(T_2^{-1} - i\omega_a\right)^2} \left[J + i\left(T_2^{-1} - i\omega_a\right)\cos\theta \right] e^{-\omega_d^2/2\sigma^2} \\ & - \frac{i\cos\theta}{J^2 + \left(T_2^{-1} - i\omega_a\right)^2} \left[J - i\left(T_2^{-1} - i\omega_a\right)\cos\theta \right] e^{-(\omega_d - 2\omega_L)^2/2\sigma^2} \ . \end{aligned} \tag{3.8}$$

To make the following discussion more transparent, in the expression given above, $\omega_{\tau_{12}}$ and $\omega_{t'}$ have been transformed into the $(-\pi/4)$ rotated diagonal (ω_d) and antidiagonal (ω_a) frequencies according to

$$\omega_d = -(\omega_{t'} - \omega_{\tau_{12}})/2 + \omega_L \qquad \omega_a = (\omega_{t'} + \omega_{\tau_{12}})/2 \qquad . \tag{3.9}$$

The shape of the absolute value of the real part of the 2D signal in frequency-frequency space, $|\mathrm{Re}\{S(\omega_{\tau_{12}}, \omega_{t'})\}|$, is schematically shown in Fig. 3.2a. In $(-\omega_{\tau_{12}}, \omega_{t'})$-coordinates, four peaks are arranged at the edges of a square with side-length $2J$. The transformation $S(\omega_{\tau_{12}}, \omega_{t'}) \rightarrow S(\omega_d, \omega_a)$ represented by Eq. 3.9 moves the new frequency origin to the center of the square and sets the signs in such a way that $\omega_{t'}$ and $|\omega_{\tau_{12}}|$ decrease with increasing

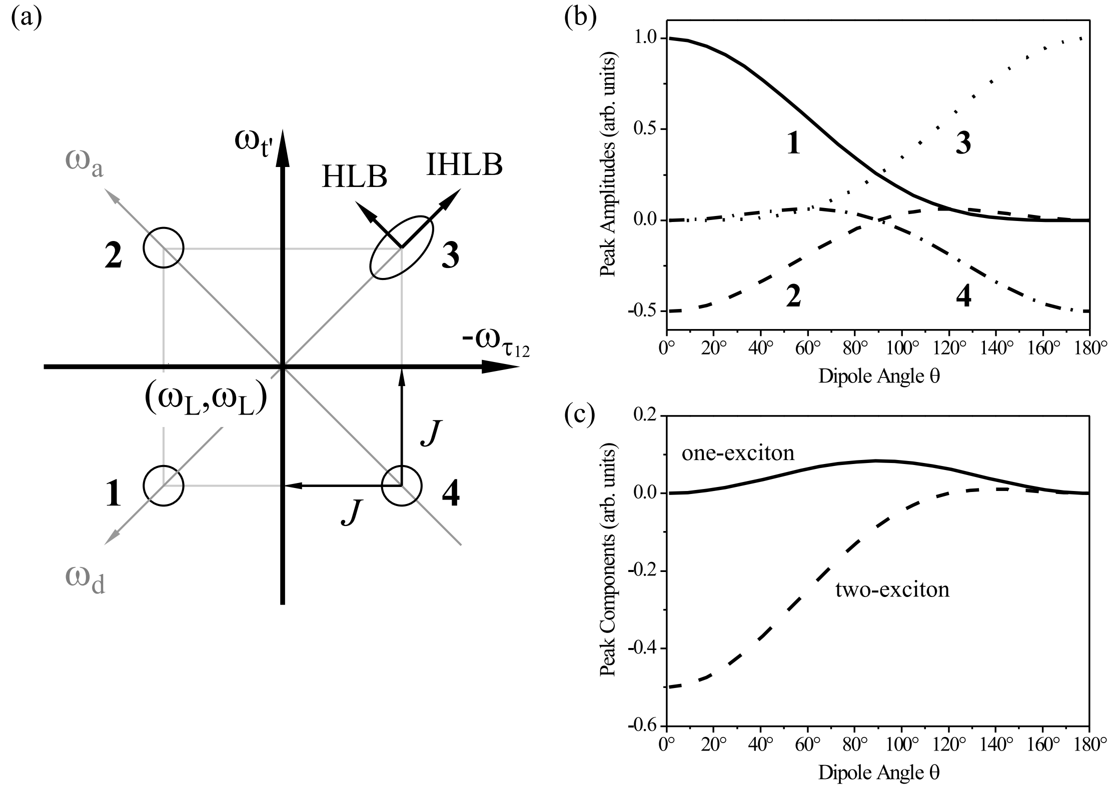

Fig. 3.2: (a) Schematics of peak positions in $|\mathrm{Re}\{S(\omega_{\tau_{12}}, \omega_{t'})\}|$, i.e. the absolute value of the real part of the 2D-PE signal, for a symmetric dimer. The origin in the $(-\omega_{\tau_{12}},\ \omega_{t'})$ plane is set to $(\omega_L,\ \omega_L)$. The rotated diagonal (ω_d) and anti-diagonal (ω_a) axes are also shown (arrows point in the directions of increasing coordinate values). HLB and IHLB denote homogeneous and inhomogeneous line-broadening, respectively. (b) Angle dependence of diagonal and anti-diagonal peak amplitudes of the real part $\mathrm{Re}\,[S(\omega_{\tau_{12}}, \omega_{t'})]$ of the 2D-PE signal (in the limit $\sigma \rightarrow 0$ and $1/T_2 \rightarrow 0$). Note that anti-diagonal peaks disappear for $\theta = \pi/2$, due to cancellation of one- and two-exciton contributions, as illustrated in (c).

ω_d. As discussed below, the cut of the signal along this axis is closely related to the (1D) LA spectrum. Since the transformation is *not* unitary, the positions of the peak maxima in the new coordinates (ω_d, ω_a) are $P_1 \equiv (J, 0)$ and $P_3 \equiv (-J, 0)$ for the diagonal peaks, and $P_2 \equiv (0, J)$ and $P_4 \equiv (0, -J)$ for the antidiagonal peaks, respectively. Eq. 3.8implies a second four-peak signal-structure, equivalent to the one sketched in Fig. 3.2a, and centered around $(-\omega_{\tau_{12}} = -\omega_L,\ \omega_{t'} = -\omega_L)$. This can be seen by substituting ω_d with $2\omega_L - \omega_d$ in Eq. 3.8, which leads to the interchange $(\omega_d \pm J - 2\omega_L)^2 \longleftrightarrow (\omega_d \mp J)^2$ and $(\omega_d - 2\omega_L)^2 \longleftrightarrow (\omega_d)^2$. However, since for optical carrier frequencies $|2\omega_L| \gg J$, terms containing $2\omega_L$ are neglected in the analysis of the signal structure around (ω_L, ω_L).

Clearly, the inter-peak distances in the 2D-PE frequency-domain spectrum contain information on the inter-site coupling J. The peak heights, on the other hand, are in distinct relation to the mutual angle θ of site-localized transition dipoles, thus serving as a structural probe for resonantly interacting molecules. For the case $J > 0$, and the limit $\sigma \to 0$ and $1/T_2 \to 0$, Fig. 3.2b shows the angle dependence of the maxima of diagonal and anti-diagonal peaks in the $\mathrm{Re}\,[S(\omega_{\tau_{12}}, \omega_{t'})]$-spectrum. While diagonal peaks have qualitatively the same dependence on θ as the peaks in LA (see below), the anti-diagonal peaks disappear in the limit $\theta = \pi/2$. This is due to the cancelation of one- and two-exciton contributions, as illustrated in Fig. 3.2c, from which one further perceives the dominance of the two-exciton contribution at small values of θ.

The consistency of results can be checked on the basis of diagonal and anti-diagonal cuts of the signal $S(\omega_d, \omega_a)$, defined as

$$\begin{aligned} D_{\mathrm{Re}}(\omega_d) &= \mathrm{Re}\,[S(\omega_d, 0] && (3.10) \\ A_{\mathrm{Re}}(\omega_a) &= \mathrm{Re}\,[S(0, \omega_a] \quad . && (3.11) \end{aligned}$$

From Eq. 3.8, one obtains for the diagonal cut

$$\begin{aligned} D_{\mathrm{Re}}(\omega_d) &= \frac{(1-\cos\theta)^2}{2} e^{-(\omega_d+J)^2/2\,\sigma^2} + \frac{(1+\cos\theta)^2}{2} e^{-(\omega_d-J)^2/2\sigma^2} \\ &\quad - \frac{\cos^2\theta}{1+(JT_2)^2} e^{-\omega_d^2/2\,\sigma^2} \qquad . \qquad (3.12) \end{aligned}$$

The first two peaks of $D_{\mathrm{Re}}(\omega_d)$ are centered at $\omega_d = \mp J$, i.e. at absolute frequency $\omega_L \mp J$, with weights $(1 \mp \cos\theta)^2/2$. As shown below, within the presented model the peaks in the LA spectrum appear at the same frequencies with quantitatively similar peak height factors of $(1 - \cos\theta)$ and $(1 + \cos\theta)$, respectively. However, in contrast to LA, where the peak shapes are determined by the convolution of homogeneous and inhomogeneous line-broadening, the peak-widths in Eq. 3.12 are exclusively determined by the IHLB parameter, which is one of the key-features of heterodyne-detected frequency-domain 2D spectra [46]. The last term in Eq. 3.12, centered around $\omega_d = 0$ (absolute frequency ω_L), ensures that the response of the system is well-behaved in the limit of decoupled sites. While the contribution vanishes under the conditions assumed here, i.e. for $1/T_2 \ll |J|$, the signal of an isolated TLS, $D^{\mathrm{TLS}}_{\mathrm{Re}}(\omega_d) = e^{-\omega_d^2/2\,\sigma^2}$, is recovered in the limit $J \to 0$ and $\theta \to 0$.

The anti-diagonal cut of the signal, in turn, is given by

$$\begin{aligned} A_{\mathrm{Re}}(\omega_a) &= -\frac{1}{T_2^2}\frac{(\omega_a^2+J^2+T_2^{-2})\cos\theta+2J\omega_a}{[(\omega_a+J)^2+T_2^{-2}][(\omega_a-J)^2+T_2^{-2}]}\cos\theta \\ &\quad +\frac{1}{T_2^2}\frac{3+2\cos 2\theta}{2(\omega_a^2+T_2^{-2})}e^{-J^2/2\sigma^2} \qquad . \end{aligned} \tag{3.13}$$

The shape of the cut is Lorentzian around the peaks at $\omega_a = \pm J$, and is controlled by the homogenous broadening parameter T_2, with peak heights determined by θ. In analogy to the cut along the diagonal, the central peak around $\omega_a = 0$ (absolute frequency ω_L) again disappears ($T_2^2\omega_a^2 \gg 1$). Furthermore, checking the TLS limit of the equation above, one obtains $A_{\mathrm{Re}}^{\mathrm{TLS}}(\omega_a) = 1/[1+(\omega_a T_2)^2]$, i.e. a single peak at the absolute frequency ω_L, as expected.

3.3 Linear Absorption Spectra

In systems without dissipation, the absorption coefficient describes a transition between two states, with a rate proportional to the inter-state oscillator strength. Here, one has to consider the absorption from the common SD ground state G to a one-exciton state E_1 mediated by the dipole moment $\mathbf{d}_{GE_1}$ [42]. Assuming the inter-site coupling to be independent of vibrational modes, the Hamiltonian H_{E_1} takes the simple form

$$\mathbf{H}_{E_1} = \begin{pmatrix} \omega_{eg} & J \\ J & \omega_{eg} \end{pmatrix} \tag{3.14}$$

H_{E_1} has one antisymmetric eigenstate with energy $E_- = \omega_{eg} - J$, and one symmetric eigenstate with energy $E_+ = \omega_{eg} + J$. Following established procedures [47] one obtains for the pure, dissipation-free absorption coefficient

$$\alpha_0(\omega) = K_1\omega\{|d_I - d_{II}|^2\delta(\omega-\omega_{eg}+J) + |d_I + d_{II}|^2\delta(\omega-\omega_{eg}-J)\} \tag{3.15}$$

where constants are collected in the prefactor K_1. After spatial averaging, using the relations $\left\langle d_I^2\right\rangle_{or} = \left\langle d_{II}^2\right\rangle_{or} = |d|^2/3$ and $\langle d_I d_{II}\rangle_{or} = |d|^2/3\cos\theta$, the SD absorption becomes

$$\alpha_0(\omega) = K_1\omega\{(1-\cos\theta)\ \delta(\omega-\omega_{eg}+J) + (1+\cos\theta)\ \delta(\omega-\omega_{eg}-J)\} \qquad . \tag{3.16}$$

Eq. 3.16 has a noteworthy limit: for $\theta = 0$, a single peak at energy $\omega = \omega_{eg} + J$ appears. This is a consequence of the fact that for parallel dipoles the symmetric eigenstate $|+\rangle$

carries the entire oscillator strength. The “real” frequency shift, however, may be either to the red or to the blue, depending on the sign of J.

To model HLB and IHLB in Eq. 3.16, one can use a well-established approach wherein the real time-resolved absorption $\alpha_0(t)$ is modified according to [47]

$$\alpha(t) = \alpha_0(t) D(t) \tag{3.17}$$

where $D(t)$ is symmetric in time and includes a Lorentzian (homogeneous) and a Gaussian (inhomogeneous) contribution, i.e. $D(t) = D_{\mathrm{HLB}}(t) D_{\mathrm{IHLB}}(t) = \exp(-|t|/T_2)\exp(-t^2\sigma^2/2)$. In frequency-space, $\alpha(\omega)$ is then given by

$$\alpha(\omega) = \int \alpha_0(\omega - \Omega) D(\Omega)\; d\Omega \qquad . \tag{3.18}$$

In the above expression, $D(\Omega)$ is the Fourier transform of $D(t)$, which can be derived analytically as

$$D(\Omega) = \frac{1}{2\sigma\sqrt{2\pi}} \left\{ \exp[-(\Omega - iT_2^{-1})^2/2\sigma^2] \left(1 - \mathrm{erf}[(i\Omega + T_2^{-1})/\sigma\sqrt{2}]\right) \right\} + c.c. \qquad . \tag{3.19}$$

Here, $\mathrm{erf}[z]$ is the complex error function. As is evident, Eq. 3.19 assumes a Lorentzian shape in the limit $\sigma \to 0$ and a Gaussian shape in the limit $T_2 \to \infty$, frequently referred to as the homogeneous and inhomogeneous limits of line broadening. Finally, combining Eq. 3.18 and Eq. 3.19, the absorption coefficient has the form

$$\alpha(\omega) = K_1 \omega_{eg} \{(1 - \cos\theta)\; D(\omega - \omega_{eg} + J) + (1 + \cos\theta)\; D(\omega - \omega_{eg} - J)\} \tag{3.20}$$

where in view of $|J| \ll \omega_{eg}$, the prefactor ω in Eq. 3.16 has been substituted by ω_{eg}.

3.4 Spectra of Discrete Conformational Distributions

With the expressions derived above at hand, one can now calculate the 1D LA spectrum as well as the 2D-PE spectrum of a given ensemble of SD conformers. In both cases, the SD spectra are simply given by the sum of individual spectra, weighted by conformational probabilities. Before demonstrating the potential of 2D-PE spectra for decoding the number of dimers involved and their inter-site orientations in disordered ensembles, it should be mentioned that the particular choices for the HLB and IHLB parameters are somewhat arbitrary. However, as will be shown, this does not affect any of the conclusions to be drawn.

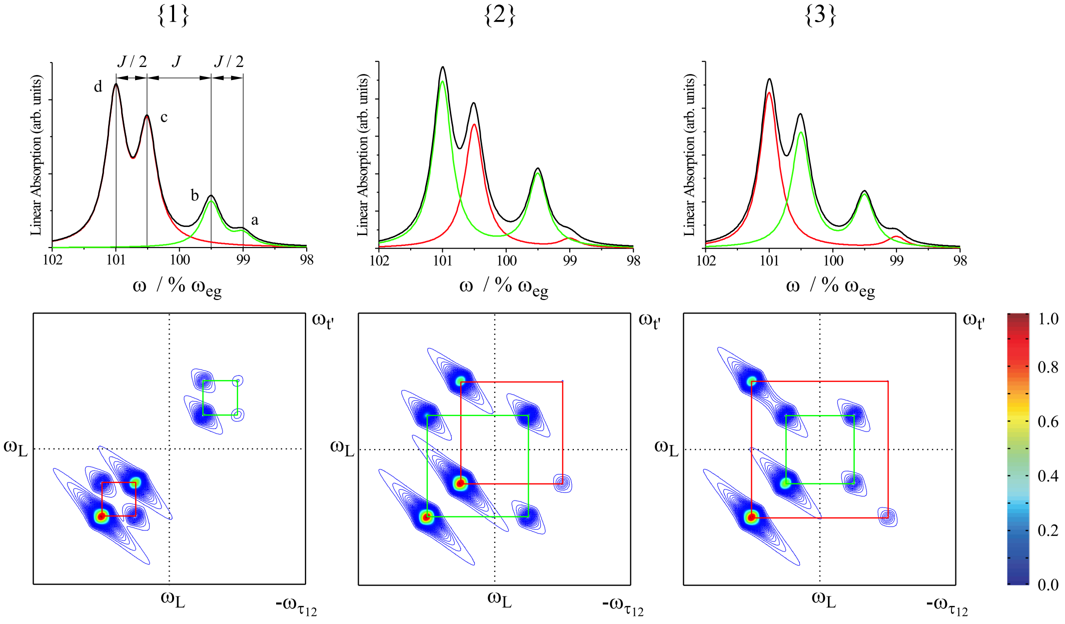

Fig. 3.3: Hypothetical linear absorption quadruplets (top row) vs. absolute values of the real part of 2D-PE signals $|\mathrm{Re}\{S(\omega_{\tau_{12}}, \omega_{t'})\}|$ (bottom row) for two symmetric dimers with common parameters $\sigma/\omega_{eg} = 1/(T_2\omega_{eg}) = 5 \cdot 10^{-4}$, corresponding to pairings $\{1\} = \{(a, b), (c, d)\}$ (left), $\{2\} = \{(a, c), (b, d)\}$ (middle), and $\{3\} = \{(a, d), (b, c)\}$ (right). The arbitrary assignment of the coherence transfer parameter J as indicated in the top left plot is explained in the text.

In the following, two specific cases are studied: (i) the assignment problem in an ensemble of two dimers ($N = 2$ system) giving a quadruplet in LA, and (ii) the unraveling of spectral doublets hidden in a congested spectrum of an $N = 4$ ensemble, for the excitonic couplings are estimated on the basis of optimized geometries and site-transition dipole moments calculated for the bridged bithiophene structure 1,2-bithiophene-2-yl-ethane-1,2-dion ($T_2[CO]_2$) using standard semiempirical methods.

Peak Assignment in an Ensemble of Two Dimers. The three top panels of Fig. 3.3 show a calculated LA spectrum of two SDs ($p_1 = p_2 = 0.5$) formed by four peaks, denoted, with increasing energy, a, b, c and d. The spectrum has been obtained from Eq. 3.20; for the parameters used, see below. Lets assume these parameters to be unknown, and to attempt to disentangle the spectrum. Guided by the general form of Eq. 3.20, and in view of the additivity of the two individual SD spectra, one can assign $\hbar\omega_{eg}$ (i.e., numerically ω_{eg}) to the frequency halfway between the peaks b and c. Further, the energy differences of neighboring absorption peaks can be denoted as $J/2$, J and $J/2$ (cf. Fig. 3.3). Pairing the peaks into doublets without using any additional information, i.e. inverting the addition of the individual spectra, the overall spectrum can be interpreted in three different ways, as any of three different sums of individual absorption spectra. A lower and higher energy peak specify a given pairing, and the possible selections from the set $\{a, b, c, d\}$ give the three pairings $\{(a, b); (c, d)\}$, $\{(a, c); (b, d)\}$, and $\{(a, d); (b, c)\}$, denoted as $\{1\}$, $\{2\}$, and $\{3\}$ in the following. The three ways to interpret the LA spectrum are visualized in the top row of Fig. 3.3.

The evaluation of the corresponding electronic couplings $\{J_1; J_2\}$ gives the values $\{J/4; J/4\}$, $\{3J/4; 3J/4\}$ and $\{J; J/2\}$; furthermore, the site energy gaps $\{\omega_{eg}^1, \omega_{eg}^2\}$ are given by the pairs $\{\omega_{eg} - 3J/4; \omega_{eg} + 3J/4\}$, $\{\omega_{eg} - J/4; \omega_{eg} + J/4\}$, and $\{\omega_{eg}; \omega_{eg}\}$, respectively. Eventually, using the relation for the peak intensity ratio of an individual SD in LA given by Eq. 3.20, the mutual orientations $\{\theta_1; \theta_2\}$ of site transition dipoles in the i-th SD can be calculated. The pairs so obtained are (30°; 67.5°), (82°; 54.5°), and (37.3°; 59.6°) for the possible pairings $\{1\}$, $\{2\}$, and $\{3\}$. As can be verified, the calculation of a LA spectrum with any of the given sets of parameters results in the same spectral shape.

The 2D-PE spectra corresponding to the three pairings are shown in the three bottom panels of Fig. 3.3. For clarity of presentation, the discussion is restricted to $|\mathrm{Re}\{S(\omega_{\tau_{12}}, \omega_{t'})\}|$, i.e. to the absolute values of the real part of 2D-PE signals. In each case, the spectrum is formed by two squares of four related peaks, each square structure representing the signals of an individual dimer. In correspondence to the specific pairings, the squares are either separated from each other (case $\{1\}$), intersecting (case $\{2\}$), or concentric (case $\{3\}$). Although the LA spectrum can be interpreted by different sums of SD doublets, the 2D-PE spectra are specific for each of the three pairings, allowing to resolve the assignment problem in LA.

The relative peak intensities in the diagonal part of the spectrum are the same as those in the LA spectrum. This is a signature of the strict one-exciton dependence of the 2D diagonal peaks. Overall, the diagonal part of the 2D-PE spectra carries the same information content as the LA spectra, which follows from the comparison of the θ-dependences of the diagonal peaks in the frequency-frequency domain, Eq. 3.12, with the LA peaks, Eq. 3.20. However, the assignment problem can be unambiguously solved by inspection of the off-diagonal peaks. This would even hold for much larger HLB and IHLB parameters. If such a simultaneous analysis of 1D LA and 2D-PE spectra were applied in an experimental study, the agreement between the relative positions of 2D-PE square quadruplets would play a decisive role.

Spectral Doublets in an Ensemble of Four Dimers. It becomes clear from the simple treatment above, that the frequency-frequency space 2D-PE signals provide a very helpful platform for the visualization of site-to-site coupling relations. Lets now turn to the more

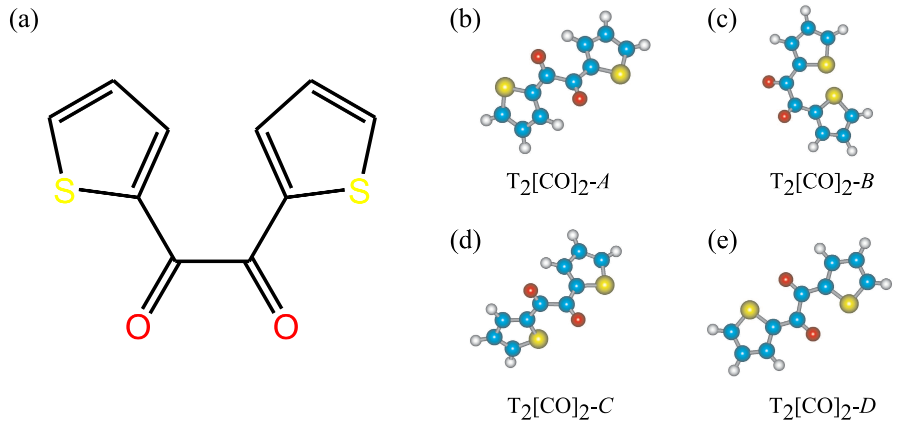

Fig. 3.4: (a) Structure of 1,2-bis-thiophen-2-yl-ethane-1,2-dion ($T_2[CO]_2$). (b)-(e) The four conformations of $T_2[CO]_2$ as obtained from semiclassical conformation analysis, denoted as A, B, C, and D, respectively (cf. Table 3.1 for details).

involved case of an $N = 4$ ensemble. Further, to approach a more realistic situation, excitonic couplings shall now be estimated on the basis of optimized geometries and semiempirically calculated site-transition dipole moments for 1,2-bithiophene-2-yl-ethane-1,2-dion ($T_2[CO]_2$, cf. Fig. 3.4a), a symmetric dimer with four different conformations, denoted A, B, C, and D (cf. Fig. 3.4b-e).

Site-to-site couplings are estimated according to the following procedure. First, a conformational analysis of $T_2[CO]_2$ has been carried out at the Hartree-Fock level using the standard semiempirical AM1 (Austin Model 1) method [48]. The inter-ring orientation is determined by two dihedral angles between the thiophene rings and the neighboring CO-group of the bridge ($S_n{-}C_\alpha{-}C{=}O$), and an additional dihedral angle ($O{=}C{-}C'{=}O'$) within the bridge [49]. For further calculations, the molecule (in a particular conformer geometry) is split into two thiophene units, by breaking the bond between the two CO-groups of the bridge and replacing the carbonyl groups by hydrogen atoms. Now, for each of the two sites, electronic transition energies and electronic transition dipole moments are calculated by the semiempirical ZINDO/S method [50]. The single excitations from the 10 highest occupied to the 10 lowest unoccupied molecular orbitals are considered. The standard ZINDO/S hamiltonian is used, with $\sigma-\sigma$ and $\pi-\pi$ overlap weighting factors of 1.267 and 0.584, respectively. All calculations are done using the Hyperchem program package [51]. Finally, taking the (center-of-mass) distance and the spatial orientation of two related units (as obtained from conformational analysis), as well as their quasi-individual electronic properties (as obtained by the described procedure), the site-to-site coupling is approximated as the dipole-dipole interaction energy [47].

	$T_2[CO]_2 - A$	$T_2[CO]_2 - B$	$T_2[CO]_2 - C$	$T_2[CO]_2 - D$
J (cm^{-1})	-19.3	-255.7	-34.4	64.1
θ (deg)	119.5	123.1	76.1	178.8
$\omega_{eg} + J$ (cm^{-1})	34945.7	34709.3	34930.6	35029.1
$\omega_{eg} - J$ (cm^{-1})	34984.3	35220.7	34999.4	34900.9

Tab. 3.1: $T_2[CO]_2$ conformation parameters

Table 3.1 collects the excitonic couplings, mutual angles of site-transition dipole moments, and one-excitonic eigenenergies of $T_2[CO]_2 - X$, where X is either A, B, C or D (and denotes the actual conformation). The single-site transition energy $\omega_{eg} = 34965$ cm^{-1} (286 nm) represents the central position of all $T_2[CO]_2 - X$ doublets in the absorption spectrum. Notably, the $S_0 \rightarrow S_1$ transition maxima as calculated with ZINDO/S (including configuration interaction) without splitting the $T_2[CO]_2 - X$ conformers into individual sites, have been found at 35335.7 cm^{-1}, 33222.6 cm^{-1}, 35971.2 cm^{-1}, and 31847.1 cm^{-1} for $T_2[CO]_2 - A$, B, C, and D, respectively. Clearly, these values are different from the one-exciton energy values obtained from the procedure described above, implying that dipole-dipole coupling describes the intersite interaction only partially, and that the effect of the site-connecting bridge is not included in J. However, for the present purposes (estimates of realistic parameters), this uncertainty is not relevant.

The LA spectrum (Fig. 3.5a) of the $T_2[CO]_2 - X$ ensemble, assuming the same ground state energy for all conformations, and a relatively small HLB/IHBL ratio ($T_2^{-1}\sigma^{-1} = 0.1$), consists of 7 peaks. In the corresponding 2D-PE spectrum (Fig. 3.5b), one discerns 14 peaks (out of a possible 16) of non-zero amplitude. As for the previous ($N = 2$) ensemble, it is a straightforward exercise to correctly assign LA doublets on the basis of squares formed by diagonal and off-diagonal signal peaks in the 2D-PE spectrum. By increasing the ratio of homogeneous to inhomogeneous line-broadening ($T_2^{-1}\sigma^{-1} = 1$), the number of discernible peaks in the LA spectrum drops to 5 (see Fig. 3.5a), since the HLB is merging some peaks into broader bands. Hence, quite apart from the assignment problem, if only the LA of a system with larger HLB is available, it is impossible to identify the number of individual peaks that are hidden under a broad, band-like structure.

In this case the 2D-PE spectrum, obtained for the same parameter set as the LA, and shown in Figs. 3.5b and 3.5c, turns out to be helpful. In the 2D spectrum, superficially viewed at the resolution of Fig. 3.5b, the number of peaks has decreased to 9. However, two of them are very broad, and evidently must be composed of two or more individual peaks. Indeed, inspecting the blow-up in Fig. 3.5c, both broad peaks are distributed over corners on different, but intertwined concentric pairs of squares. It follows that in the

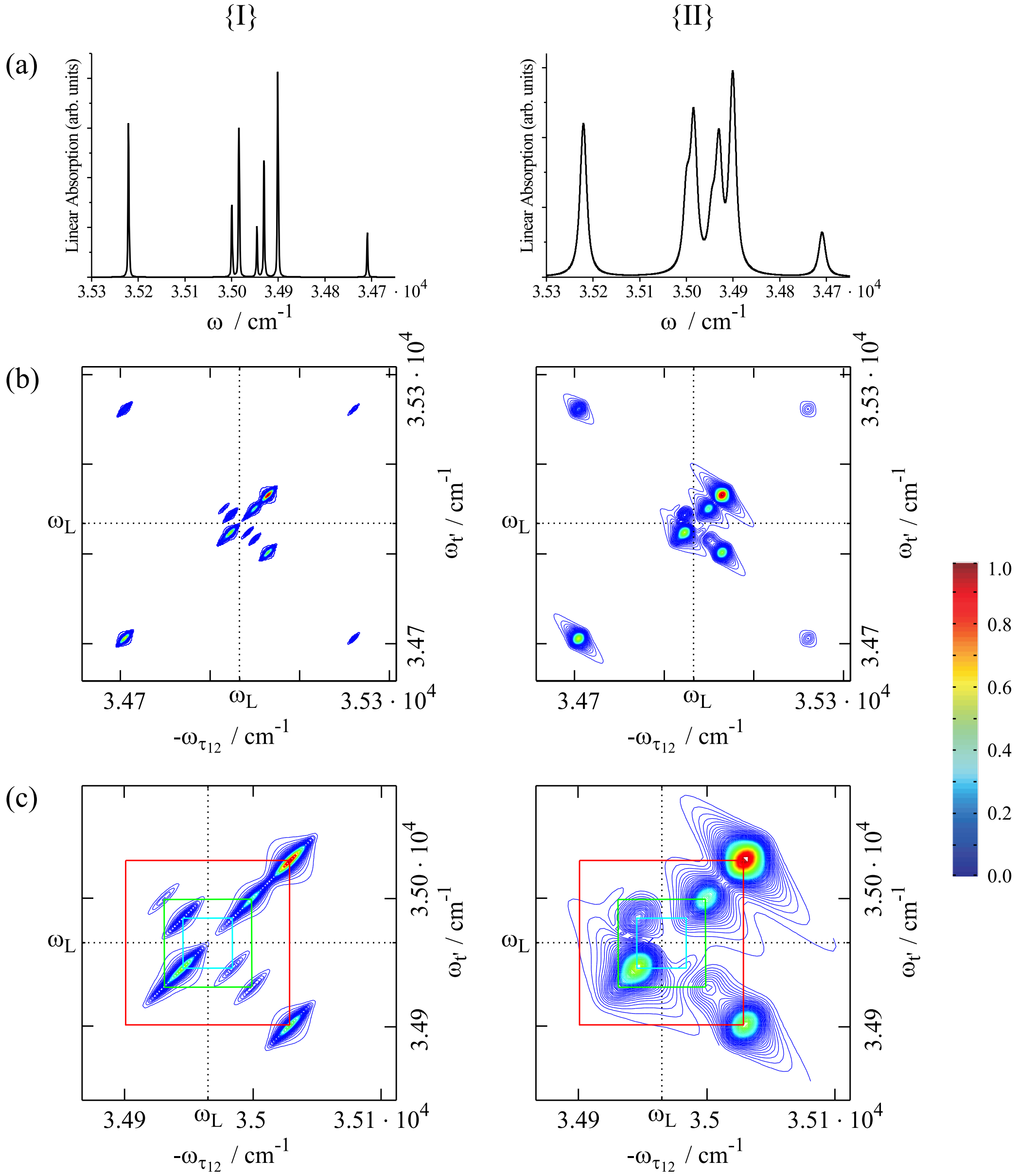

Fig. 3.5: Linear absorption vs. $|\mathrm{Re}\{S(\omega_{\tau_{12}}, \omega_{t'})\}|$ for the system formed by $\mathrm{T}_2[\mathrm{CO}]_2 - A$, B, C, and D, assuming equal conformational probabilities. Left column (I): Low HLB/IHLB ratio $T_2^{-1}\sigma^{-1} = 0.1$. Right column (II): High HLB/IHLB ratio $T_2^{-1}\sigma^{-1} = 1$. In both cases, $\sigma/\omega_{eg} = 2.10^{-4}$ and $\omega_{eg} = 34965\,\mathrm{cm}^{-1}$. Remaining parameters are given in Table I. (a) LA spectra. (b) 2D-PE spectra calculated for the same parameters. (c) Central parts of the 2D-PE spectra showing precise peak-positions in the frequency range of overlapping LA peaks. Dashed squares indicate the positions of peaks corresponding to individual symmetric dimer signals.

inner area of the 2D spectrum, it is possible to assign peaks corresponding to three SDs, the fourth SD clearly corresponding to the well separated outer square in Fig. 3.5b.

As it is well known that in a 2D-PE spectrum HLB operates by broadening peaks along the anti-diagonal coordinate, it is interesting to note that the strongly broadened peaks in the present spectrum belong to the diagonal subset, while the off-diagonal spectrum is, in fact, the better resolved one. This can be ascribed to the lower amplitudes of the off-diagonal peaks. On an absolute scale, the more intense peaks have a larger homogeneous width and thus, for the same peak-to-peak distances, the broader (diagonal) peaks are more strongly overlapping. Based on this analysis of information contents of the LA and 2D-PE spectra of the system formed by $\mathrm{T}_2[\mathrm{CO}]_2 - A$, B, C and D, one concludes that, not quite unexpectedly, “the more peaks, the more information”. From the broad band in the center of the LA spectrum, it is impossible to determine how many individual peaks are hidden under the three apparent ones, while from the 2D-PE spectrum, with twice the information content, this number can readily be extracted. In the 2D-PE spectrum of SDs, the number of peaks is increased by a factor of two (relative to LA), but since the spectra are spread into a second dimension, there is a chance to resolve congested 1D spectra by comparison with informationally richer 2D signals. This will always be the case if the range of the 2D-PE spectrum accommodating the cross peaks is less congested than the LA spectrum.

3.5 Conclusions

On the basis of a Frenkel exciton description, an analytical solution for the heterodyne detected 2D-PE signal of SDs is presented. The expressions are sufficiently general to recover the correct signal shapes for isolated chromophores as limiting cases. The 2D spectra, determined by field- and coupling-induced transitions of site-localized excitons (correlated up to the fourth order), provide the direct visualization of exciton correlations, and a projection of homogeneous and inhomogeneous broadening into orthogonal frequency channels. Since the coupled dynamics of site transition-dipoles depends on their mutual orientation and on the extent of the inter-site coupling J, it can form the basis of structural studies, which are spatially limited only by the range of the electronic interaction. Two examples illustrate how assignment problems in 1D LA spectra of disordered systems can be solved by inspection of the 2D-PE signal peak structure in frequency-frequency space. In a system of two conformationally different SDs, each individual dimer gives rise to a square-like peak pattern, which can readily be identified in the 2D spectrum. The concept is equally applicable to congested spectra subject to substantial broadening, as illustrated in the case study of a bridged bithiophene structure with four stable conformations.

For many systems of experimental interest, at least some of the simplifications of the present model will have to be dropped. If the electron densities of chromophores overlap, the electronic coupling will involve additional contributions. In particular for π-conjugated chromophores in close spatial proximity, charge-transfer states will have to be included into the excited state description. The pair of lowest allowed excited states can be effectively represented by two mixed Frenkel-Wannier excitons (i.e. by “right” and “left” local excitations with some charge-transfer character), and by an effective coupling having both resonant and charge-transfer contributions [43]. Such an effective excitonic description complicates the situation, because delocalized molecular orbitals of strongly coupled (quasi-) dimers will first have to be transformed to obtain quasi-monomer localized orbitals (compare, e.g., Ref. [52]). Another important issue is electron-nuclear coupling and the possibility of coherent nuclear motion in photoexcited, flexible sites. In such systems, vibrational effects on the topology of 2D-PE signals of electronically coupled dimers are essential and will have to be included. In this context, the 2D wavepacket interferometry description of multi-dimensional electronic spectroscopy developed by Cina *et al.* [44] can be taken as a guidepost. Certainly, the most important feature left unconsidered in the present work, but also the most natural extension of the model, is the inclusion of time-resolution with respect to the waiting time T. This additional information can already be helpful in the context of spectroscopic assignment, since a different time evolution of individual peaks may expose still hidden information. The most important aspect, however, is its capability to provide a direct time-resolved view into ongoing energy transfer processes.

To summarize, in combination with quantum-chemical calculations of geometrical structures and electronic states, the presented model provides a platform for the interpretation of cross-correlation signals in 2D-PE spectra. A system of two conformationally different, electronically coupled dimers may be considered as the simplest case of a disordered chromophoric ensemble. For larger systems, the solutions presented may be used in iterative procedures to test model assumptions on narrow conformational distributions underlying the observed 1D and 2D spectra.

4. EXPERIMENTAL DESIGN

After addressing the essential prerequisites for the experimental implementation of two-dimensional optical spectroscopy, this chapter describes a passively phase-stabilized set-up, suitable for studies across the entire visible spectrum. Passive phase-stabilization is achieved by a diffractive optical element, the use of refractive optics for introducing pulse delays, and the use of common optics for the pulse-pairs that need to be phase-locked. Calibration procedures and evaluation protocols, experimental pitfalls, and the superficially trivial point of sample handling are discussed.

Related publications:

Two-dimensional electronic spectroscopy of molecular excitons
F. Milota, J. Sperling, A. Nemeth, T. Mancal, and H. F. Kauffmann
Accounts of Chemical Research, **42**, 1364 (2009)

2D Optical Spectroscopy of a Conjugated Polymer with tunable visible 15 fs-Pulses from a 200kHz NOPA
F. Milota, P. Baum, J. Sperling, E. Riedle, K. Matuszna, and H. F. Kauffmann
Springer Series in Chemical Physics, **88**, 359 (2007)

4.1 Introduction

The experimental implementation of two-dimensional electronic spectroscopy requires two essential prerequisites. First, the emitted signal field, not just its intensity, must be fully characterized in time and/or frequency, commonly referred to as *heterodyne* detection (in contrast to *homodyne* detection schemes, in which phase information is lost). Notably, heterodyne detected photon-echoes have been carried out by D. A. Wiersma and co-workers already in the mid 90's, by characterizing nonlinear signals in a separate up-conversion experiment [53, 54, 55, 56]. The level of complexity has been significantly reduced by the pioneering works of M. Joffre and co-workers [21, 57, 58], who switched experimental signal detection into frequency domain employing Fourier transform spectral interferometry. The technique relies on mixing the signal field with a collinearly propagating local oscillator field (LO), that is usually much stronger than the signal itself and shifted by an amount t_4 in time. The interference pattern of the two fields can be recorded in frequency domain with a simple time-integrating spectrometer. It is given by

$$\begin{aligned} I_{het}(\omega) &= |E_{sig}(\omega) + E_{LO}(\omega)|^2 \\ &= |E_{sig}(\omega)|^2 + |E_{LO}(\omega)|^2 + 2\mathrm{Re}(E^*_{sig}(\omega)E_{LO}(\omega)) \\ &= |E_{sig}(\omega)|^2 + |E_{LO}(\omega)|^2 + 2|E^*_{sig}(\omega)E_{LO}(\omega)|\cos\left(\phi_{LO}(\omega) - \phi_{sig}(\omega) + \omega t_4\right) \end{aligned} \tag{4.1}$$

where E_{sig} (E_{LO}) and ϕ_{sig} (ϕ_{LO}) are the electric field and the spectral phase of the signal (local oscillator) [21]. Given that (i) $E_{sig} \ll E_{LO}$ and (ii) the LO field is known, the first two terms ($|E_{sig}|^2$+$|E_{LO}|^2$) in the last line above can be neglected respectively subtracted. The phase of the signal field is then retrieved from the remaining term $2\mathrm{Re}(E^*_{sig}E_{LO})$ by a Fourier transform into time-domain, filtering, and back transformation [21]. This allows to separate the detected nonlinear optical response into its real and imaginary part.

It is essential to realize that $I_{het}(\omega)$ is usually not recorded in "single-shot mode", but integrated over a certain number of pulse pairs. Thus, a characterization of the signal transient by spectral interferometry is only applicable if there is a stable synchronization between the two fields. In other words, the signal electric field must result from a coherent emission that is triggered either by the local oscillator itself or by a coherent offspring under a constant phase relation. This notion connects to the second challenge encountered in electronic 2D spectroscopy: Creation of phase stable relationships within the sequence of excitation/detection pulses in combination with adjustable time delays.

Several experimental strategies have been established to fulfill the outlined criteria. Employing active phase-stabilization, all of the excitation beams may be stabilized, which allows to perform different variants of four-wave mixing experiments in heterodyne detection mode, such as heterodyned transient gratings or double-quantum 2D spectroscopy [59, 60]. A drawback of this approach is the considerable complexity of such experiments due to additional feedback loops of the stabilization electronics. Alternatively, pulse-shaping devices may be utilized to create collinear [61], partially non-collinear [62, 63], or fully non-collinear [64, 28] pulse sequences with controllable inter-pulse delays and phases. As a key advantage, pulse-shaping based set-ups permit to select the desired nonlinear signal by phase-cycling procedures (coadding experimental results obtained with different inter-pulse phases). A particular disadvantage of collinear geometries, in turn, is the necessity of signal detection against a background that is orders of magnitude more intense, as it includes the incident light fields as well as all other nonlinear responses. Pulse-shaping techniques have thus been joined with non-collinear geometries by several groups [64, 63, 28], combining interferometric phase stability and generalized waveform shaping capabilities in each of the incident beams.

Yet another approach relies on employing diffractive optical elements (gratings) as beam-splitters that generate two or more replicas out of a single incoming pulse [65, 66, 67, 68, 69]. In such arrangements, pulse delays are commonly adjusted by steering refractive optical elements like, e.g., moveable glass wedge pairs inserted into the beam paths. This allows to design reliable and relatively simple, passively phase-locked set-ups for carrying out two-dimensional electronic spectroscopy in the visible part of the spectrum. It should be noted, however, that due to the dispersive nature of gratings such strategies presumably will not be effective for ultra-broadband excitation conditions or for experiments covering the ultraviolet spectral range. Experimental set-ups that are particularly designed for exploiting phase-cancelation effects emerge as promising alternatives in this context [66, 70, 71].

The results reported in this thesis have been obtained by employing an experimental design inspired by the work R. J. D. Miller and co-workers [66], and G. R. Fleming and co-workers [67, 68]. Passive phase-stabilization is achieved by a diffractive optical element, the use of refractive optics for introducing pulse delays, and the use of common optics for the pulse-pairs that need to be phase-locked.

4.2 Pulse Generation

The beamline is based on an all-solid state laser system that pumps a non-collinear optical parametric amplifier (NOPA) at a reptition rate of 200 kHz [72]. After appropriate compression by combining brewster angled chirped mirrors and a fused-silica prism sequence [73], the system yields pulses which are widely tuneable in the region from 20800 to 13900 cm^{-1} (480 to 720 nm), and have energies of more than 250 nJ and durations of less than 20 fs. The high repetition rate thereby strongly facilitates averaging and data acquisition. For complete characterization of the excitation fields and to ensure shortest possible pulse durations at the sample, zero-additional-phase SPIDER[1] (ZAP-SPIDER) is applied [74, 75, 76, 77].

Pump Laser, Oscillator, Regenerative Amplifier. The sole pump source Verdi V-18 (Coherent Inc.) is a diode-pumped, frequency-doubled Nd:Vanadate (Nd:YVO4) laser. After intracavity doubling (intracavity SHG) of the characteristic lasing wavelength (1064nm), Verdi V-18 delivers 16 W of continuous wave power at 532 nm, which is split to pump the oscillator Mira Seed and the regenerative amplifier RegA9050 (both Coherent Inc.) with 6 W and 10 W, respectively.

Mira Seed is a passively (Kerr lens) modelocked Titanium:Sapphire oscillator, featuring an intracavity prism-compressor. For the experiments described here, its operating wavelength (tunable from 780 to 840 nm) has been adjusted to 800 nm. Mira Seed typically delivers 420 mW in mode-locked operation, with pulse durations of 30 fs at a repetition rate of 76 MHz, corresponding to a single pulse energy of 5.5 nJ. Prior to amplification, the pulses are stretched in a diffractive (grating-based) stretcher-compressor unit to approximately 10 ps.

The principle of operation of the regenerative amplifier RegA9050 essentially relies on appropriately timed Q-switching of the laser cavity, injection of a stretched oscillator pulse, its amplification within a defined number of intracavity round-trips, and pulse ejection by the cavity dumper. The amplification process thereby lowers the repetition rate to 200 kHz. Recompression of the pulses is again achieved in the aforementioned stretcher-compressor unit. The obtained pulse train is characterized by a typical average power of 1.1 W (corresponding to a single pulse energy of 5.5 μJ) and pulse lengths of 45 fs.

Noncollinear Optical Parametric Amplifier. For conversion of the pulses into the visible spectral range, a non-collinear optical parametric amplifier (NOPA) [78] is employed. The non-collinear arrangement of the pump and seed (signal) beam in a NOPA is

---

[1] **S**pectral **P**hase **I**nterferometry for **D**irect **E**lectric field **R**econstruction

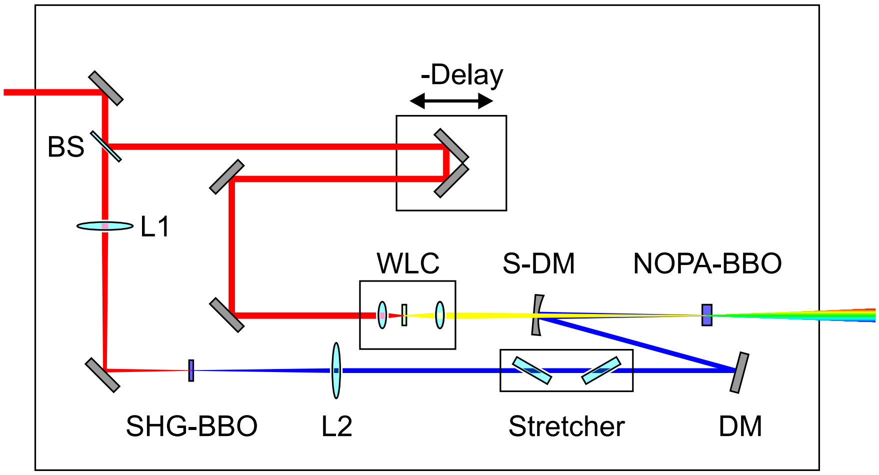

Fig. 4.1: Schematics of the non-collinear optical parametric amplifier (NOPA): (BS) beamsplitter, (L1,L2) lenses, (SHG-BBO) second-harmonic crystal, (DM) dichroic mirror, (WLC) white light continuum stage, (S-DM) spherical dichroic mirror.

an elegant solution to the problem of pulse lengthening encountered in collinearly phase matched parametric interactions (as a result of different group velocities of the pump, signal, and idler beams). The effective matching of the signal and idler group velocities in a non-collinear geometry is equivalent to very broadband phase matching in the parametric process. Consequently, a broad spectral range of the seed light can be amplified, resulting in output pulses that can be routinely compressed below 20 fs. A more detailed discussion can be found in Ref. [79].

Fig. 4.1 shows the schematic design of the NOPA unit. Briefly, the 800 nm input is split with a 10:90 beamsplitter (BS). For second harmonic generation, 90% of the energy are focused with a lens (f = 200 mm, L1) onto a 300 μm thick BBO crystal. The remaining 10 % are focused onto a 1 mm thick sapphire crystal for white light continuum generation (WLC unit in Fig.4.1). The second harmonic and the white light are brought to temporal and spatial overlap in a 2 mm thick BBO crystal (NOPA-BBO), where a part of the white light is amplified in a parametric amplification process (the white light beam is thereby aligned onto the super-fluorescence cone generated by the 400 nm pulses). As the white light pulses generated in the sapphire plate are highly chirped, control of their temporal delay with respect to the 400 nm pump-pulses (λ-delay in Fig. 4.1) allows for frequency selective amplification (the interaction geometry at the NOPA-BBO requiring appropriate readjustment). To increase the amplified spectral bandwidth, the 400 nm pulses are temporally stretched prior to the parametric amplification step (stretcher in Fig. 4.1) in two 15 mm thick fused silica plates which are arranged at Brewster angle. The

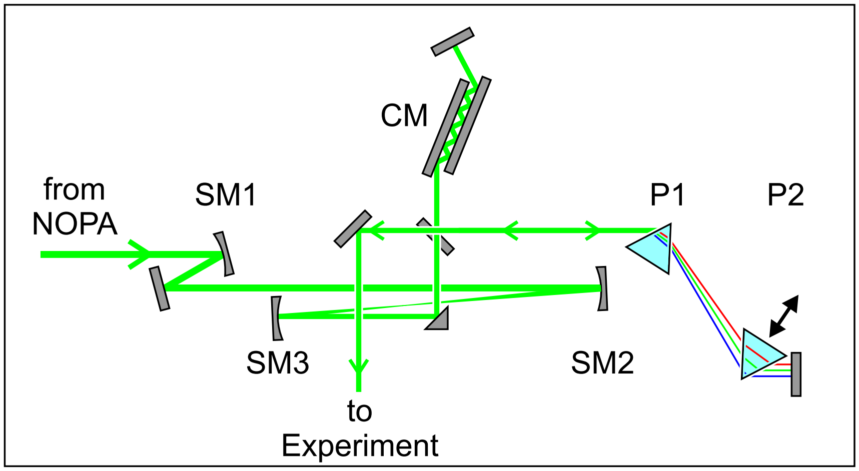

Fig. 4.2: Pulse compression by chirped mirrors and a prism pair: (SM1) spherical mirror ROC=1000 mm, (SM2) spherical mirror ROC=300 mm, (SM3) spherical mirror ROC=200 mm, (CM) chirped mirrors, (P1,P2) prisms.

central wavelength of the NOPA output can be tuned in the region between 480 nm and 720 nm. At 600 nm, e.g., the spectral width is 40 nm, the power reaches typically 45 mW (pulse energy 225 nJ), and the pulse duration can be compressed to typically 16 fs.

Pulse Compression and Characterization. Since the broad bandwidth output pulses of the NOPA are chirped due to the initial chirp of the seed continuum and additional chirp caused by the dispersion in the BBO (and the transmissive optics), pulse compression is required. Fig. 4.2 shows the schematics of the employed compressor unit. After collimating the slightly diverging NOPA output beam (by spherical mirror SM1), a telescope (SM2 and SM3) is implemented to reduce the beam diameter and to homogenize its spatial intensity distribution. Subsequently, in a first step, higher order chirp is compensated by 24 reflections from two Brewster-angled chirped mirrors coated with 58 alternating SiO_2/TiO_2 layers (a detailed discussion of the underlying principle and its applications can be found in Refs. [80, 73, 81]). The second step is a conventional (fused silica) prism compression for eliminating linear chirp (cf. Fig. 4.2).

It is important to note that compression of pulses minimizes their durations at one single point in space only. In other words, pulse durations are ideally characterized in the spot of the spectroscopic experiment or an equivalent position, which allows for appropriate precompensation of dispersive elements encountered along the beam baths for pulse manipulation. Thus, for a full characterization of the excitation pulses and effective precompression ensuring the shortest possible pulse duration at the location of the experiment, a ZAP-SPIDER apparatus is applied (the set-up is equivalent to the one presented in

Ref. [76]). To cross-check the validity of ZAP-SPIDER traces, additionally a frequency resolved second-harmonic intensity autocorrelation is recorded, by placing a 50 μm thick β-barium borate (BBO) crystal at the sample position. To reduce unwanted higher-order effects (and non-resonant signals from the solvent) and to prevent samples from too fast photodegradation, the NOPA beam is attenuated by a neutral density (ND) filter to yield not more than typically 1 nJ of energy in each of the excitation pulses.

4.3 Experimental Set-up and Procedures

Passively Phase-locked Diffractive Optics based Set-up. The experimental set-up is shown in Fig. 4.3. The description below follows the beam path of the precompressed input from the NOPA.

A 50:50 beamsplitter creates two beams of equal intensity, one of which travels along a conventional delay line (a linear translation stage with reflective optics) for adjustment of time delay t_2 (cf. inset in Fig. 4.3 and further explanations below). Both beams are focused with a spherical mirror (ROC = 600 mm) on a transmission grating (125 grooves/mm respectively a groove spacing of 8 μm), that is optimized for diffraction into ± first order. This creates two phase locked pulse pairs ($\mathbf{k_1}/\mathbf{k_2}$ and $\mathbf{k_3}$/LO) and arranges the four beams on the corners of a square (boxcar geometry). Pulse $\mathbf{k_3}$ and the LO are diffracted downwards (dotted lines in Fig. 4.3) and pulses $\mathbf{k_1}$ and $\mathbf{k_2}$ are diffracted upwards (solid lines) with respect to the initial beam height.

A focusing mirror (ROC = 750 mm) parallelizes the four diverging beams. Pulse $\mathbf{k_2}$ can be variably delayed with a motorized arrangement of two fused-silica glass wedges (thickness 0.9 mm, angle 2°, from Hellma) that are oriented antiparallel to each other (to avoid angular beam displacement upon increasing or decreasing the overall glass thickness). Given the encoder resolution (0.1 μm) of the computer controlled stage, time delay t_1 can be introduced with a resolution of 5.3 as and negligible amounts of chirp, as illustrated in Fig. 4.4. The latter shows ZAP-SPIDER traces for three wedge positions (corresponding to a time delay of -200, 0, and +200 fs) at pulse durations of 16 fs and a time-bandwidth product of 0.606. Pulses $\mathbf{k_1}$ and $\mathbf{k_3}$ traverse equivalent glass wedges in order to balance the dispersion with respect to $\mathbf{k_2}$. The LO is attenuated by a neutral density filter (ND), which is chosen in such a fashion that the local oscillator is attenuated by 3 orders of magnitude and precedes the other pulses by approximately 550 fs.

All four beams are focused onto the sample with a second spherical mirror (ROC = 750 mm) to a common spot size of ≈ 150 μm. The generated signals ($\mathbf{k_s} = \pm\mathbf{k_1} \mp \mathbf{k_2} + \mathbf{k_3}$), prop-

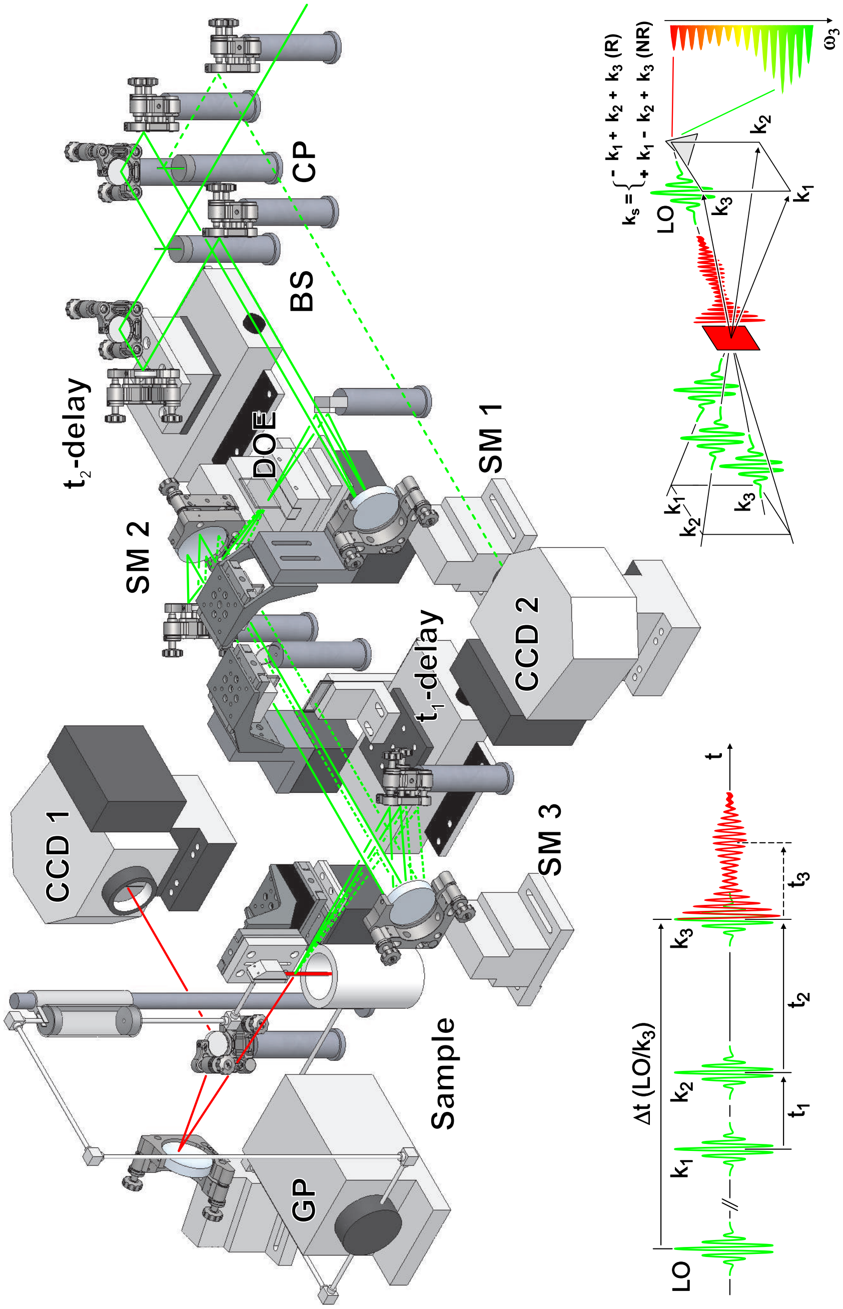
CP
BS
t_2-delay
DOE
SM 2
SM 1
CCD 2
t_1-delay
SM 3
CCD 1
Sample
GP
$k_s = \{ - k_1 + k_2 + k_3$ (R), $+ k_1 - k_2 + k_3$ (NR)
ω_3
LO
k_1
k_2
k_3
Δt (LO/k_3)
t_1
t_2
t_3
t

Fig. 4.3: Experimental set-up (rotated figure): (BS) beamsplitter, (CP) compensation plate, (DOE) diffractive optical element, (SM) spherical mirror, (GP) gear pump, (CCD) charge coupled device spectrometer. The left inset shows the definition of delay times, the right inset depicts the detection scheme and the geometry of the 2D-ES experiment: three pulses with wavevectors $\mathbf{k_1}, \mathbf{k_2}$ and $\mathbf{k_3}$ create a nonlinear signal ($\mathbf{k_s} = +\mathbf{k_1} - \mathbf{k_2} + \mathbf{k_3}$ for $t_1 < 0$ respectively $\mathbf{k_s} = -\mathbf{k_1} + \mathbf{k_2} + \mathbf{k_3}$ for $t_1 > 0$) which is spectrally interfered with a local oscillator field (LO) for signal detection in frequency domain.

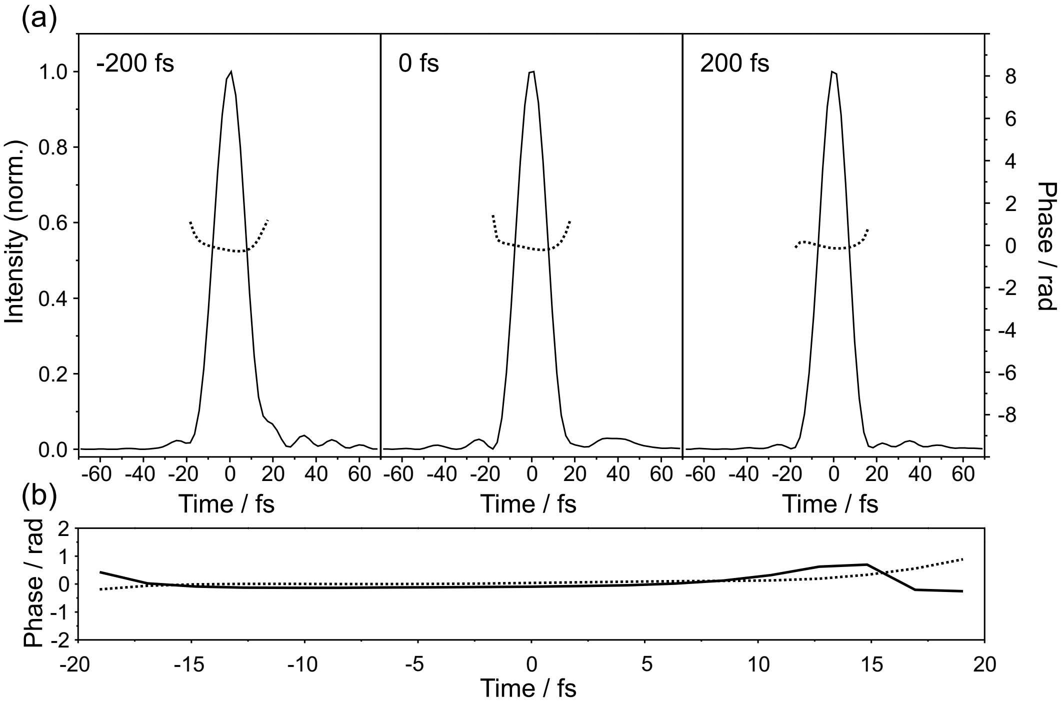

Fig. 4.4: (a) ZAP-SPIDER traces for the three wedge positions corresponding to a time delay of -200 fs (left), 0 fs (middle), and +200 fs (right). In all three cases the pulses have a duration of 16 fs and a flat temporal phase. (b) Residual phase differences between 0 fs and -200 fs (dashed line) respectively 0 fs and +200 fs (solid line).

agating along the path of the LO, are collimated by a spherical mirror (ROC = 500 mm) and focused onto the slit of a thermo-electrically cooled 1024 pixel CCD spectrometer (equipped with a 1800 groves/mm grating).

The phase stability of the setup can be tested, e.g., by monitoring the interference pattern between the signal and the LO over an extended period of time. Fig. 4.5 shows magnifications of typical spectral interferograms recorded over a time period of 90 minutes and after multiple scans and delay line movements. Fringe positions in the interferograms show no substantial changes within typical measurement sequences.

Calibration of Delays. The $t_1 = 0$ and $t_2 = 0$ points and the delay lines are determined, respectively calibrated, by spectral interferometry. A 25 μm diameter pinhole is placed at the sample position where all beams overlap. Two of the beams (1 and 2 for t_1-, 1 and 3 for t_2-delay) pass the pinhole. Since the diameter of the pinhole is smaller than the actual focus of the beams (approx. 150 μm), diffraction effectively generates two collinear plane waves whose spectrum (recorded with the spectrometer) shows an interference pattern. The number and distance of the fringes is a function of the delay stage position. Fourier

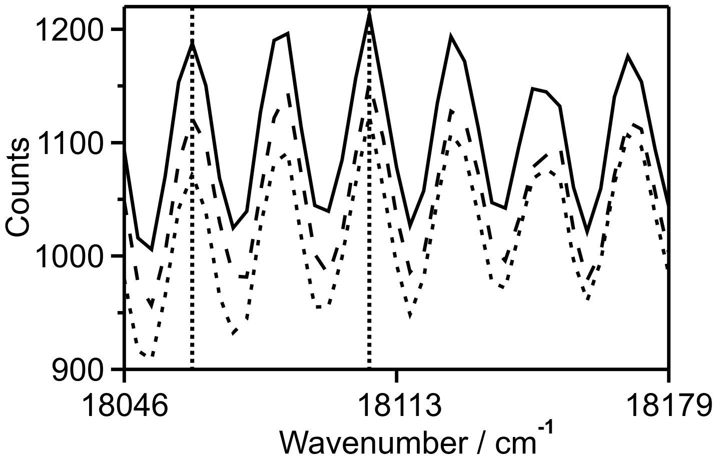

Fig. 4.5: Comparison of three interferograms (t_1, $t_2 = 0$) recorded over a time period of 90 minutes and after multiple scans and delay line movements. Solid line indicates the first interferogram, dashed line after 45 minutes, and short dashed line after 90 minutes (vertical lines serve as guidelines to the eye).

transformation of these interferograms gives three peaks at $t = 0$ and $t = \pm\tau$, where τ is the temporal separation of the pulses. For pulse separations above/below ±50 fs we plot delay versus stage position and extrapolate for $\tau = 0$ to determine $t_1, t_2 = 0$. Fig. 4.6 shows this procedure in a exemplary manner.

Though this procedure has been found suitable for the determination of zero-points, we have found it inappropriate for a precise calibration of the mechanical-to-optical delay conversion factors (necessary for converting the movement of the translation stages into optical delays). This point is crucial insofar, as our temporal scans are designed to fulfill the Nyquist criterion given by the central excitation wavelength (at least two points are sampled within a spatial delay corresponding to one period of the central excitation frequency). Consequently, any inappropriate calibration immediately translates into spectral shifts of the 2D spectra along ω_1 (i.e., along the indirectly measured frequency axis, for which Fourier transform into frequency domain has to be done explicitly).

Determination of calibration coefficients for the stages is achieved by selecting several frequency-cuts in the frequency resolved scan (oscillating functions of the stage position, cf. Fig. 4.7). A subsequent Fourier transformation of this waveforms yields the inverse number of stage steps necessary for one full period at a particular frequency cut. Since the period for a given frequency is well known (e.g. 2 fs at 500 THz), the calibration coefficient is the product of the inverse number of steps times the period in femtoseconds. This is done for a number of frequency cuts to calculate an average calibration coefficient.

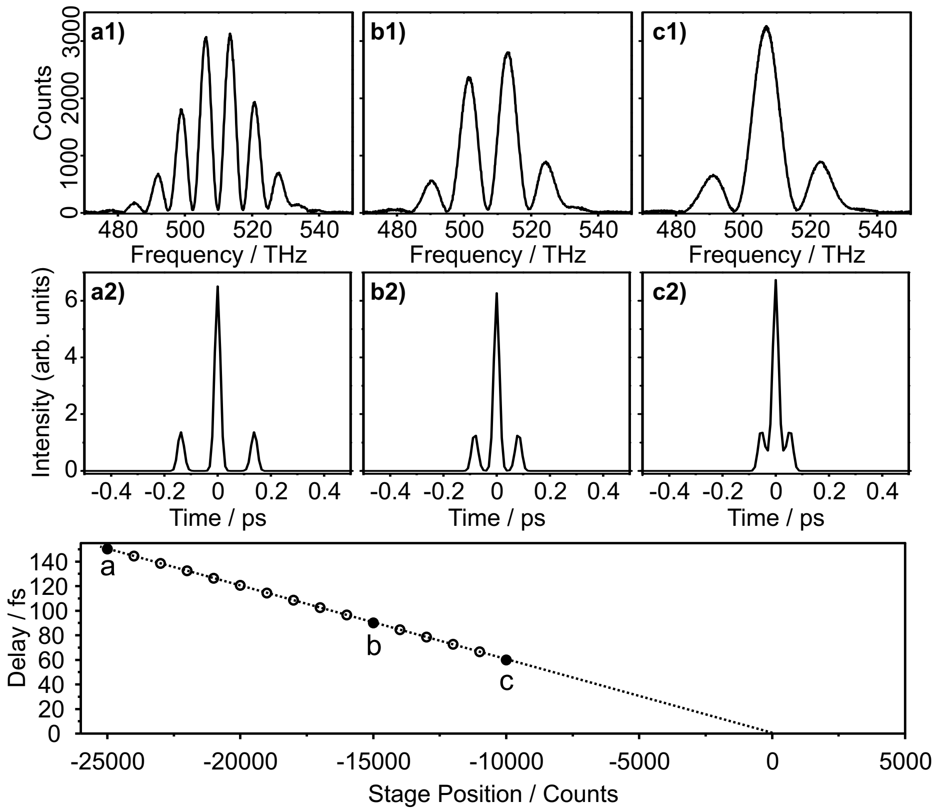

Fig. 4.6: Determination of zero-points by spectral interferometry. Panels a1, b1, and c1 show interferograms for stage positions of -25000, -15000, and -10000 counts. Panels a2, b2, and c2 are the corresponding Fourier transformations, which are plotted in the lowest panel as a function of motor position to determine the zero-point by extrapolation. Solid points correspond to values extracted from the interferograms (other points in the lowest panel are not depicted explicitly). Values below 50 fs are neglected due to poor resolution in frequency domain.

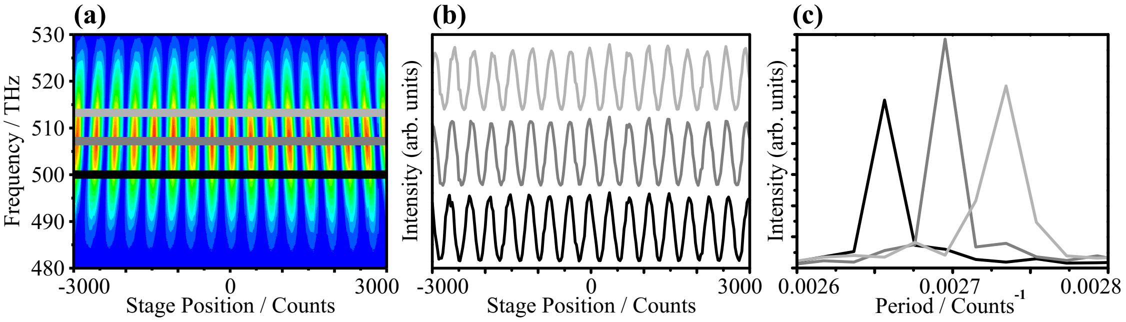

Fig. 4.7: Calibration of delay stages by spectral interferometry. (a) Frequency resolved scan with 3 frequency cuts at 500 THz (black), 507 THz (grey), and 513 THz (light-grey). (b) Waveforms of the corresponding frequency cuts. (c) shows the corresponding Fourier transforms, which give the inverse number of counts for one period of each cut.

Data Acquisition and Evaluation Protocol. Two-dimensional electronic spectra are recorded by scanning the t_1-delay (separating the first two interactions) symmetrically around $t_1 = 0$, while delay t_2 (separating the second and third interaction) is kept constant. In other words, for negative delay times only the t_1-stage is moving (refractive delay line), while for $t_1 \geq 0$ both stages (refractive and conventional delay line) move simultaneously to maintain the desired t_2 delay. The procedure collects non-rephasing contributions in the direction $\mathbf{k_s} = \mathbf{k_1} - \mathbf{k_2} + \mathbf{k_3}$ for negative values of t_1, and rephasing contributions in the direction $\mathbf{k_s} = -\mathbf{k_1} + \mathbf{k_2} + \mathbf{k_3}$ for positive t_1 values. This allows to dissect the signals into purely absorptive and purely dispersive parts of the complex 2D spectrum, by equally weighting rephasing and non-rephasing contributions [82].

Applying the described scheme, t_1-delays are scanned in 0.65 fs steps within intervals that range from typically ± 100 fs to ± 200 fs . Note that despite the high resolution of the refractive delay line, the applicable step-size is limited by the resolution of the conventional delay line (since, for $t_1 \geq 0$, the refractive delay can be only moved in multiples of the resolution of the conventional delay, in order to ensure a constant t_2).

The remaining steps follow very closely the procedure outlined by T. Brixner *et al.* [68], and shall be briefly repeated only for the sake of completeness. First, the CCD spectrometer does not only detect the desired signal

$$I_{het}(\omega) = |E_{sig}(\omega) + E_{LO}(\omega)|^2 \tag{4.2}$$

but also scattering contributions from all other pulses, which need to be subtracted prior to evaluation of the interference patterns. This is done in two steps. At the beginning of each experiment beams $\mathbf{k_1}$ and $\mathbf{k_2}$ are blocked with a shutter and the scattering contribution from beam $\mathbf{k_3}$ is recorded. As the delay between $\mathbf{k_3}$ and LO does not change during the course of an experimental scan, this contribution has to be recorded only once. For subtraction of the scattering contribution from beams $\mathbf{k_1}$ and $\mathbf{k_2}$, beam $\mathbf{k_3}$ is blocked with a computer controlled mechanical shutter (this scattering contribution has to be recorded and subtracted for each time step t_1 during a scan).

For every time-step in t_1, the signal field $E_{sig}(\omega)$ is reconstructed from the interferogram (Eq. 4.2) as follows. $I_{het}(\omega)$ is Fourier transformed into time domain, yielding three peaks at $t = -t_4, 0, +t_4$ (where t_4 denotes the time delay between the signal and the LO). Upon applying a filter function, only the peak at $t = +t_4$ is kept and inverse Fourier transformed. The amplitude of this complex term corresponds to $|E_{LO}(\omega)||E_{sig}(\omega)|$. $|E_{LO}(\omega)|$ is related to the spectrum of the LO pulse (which is readily measured), and can be divided out. The phase of the complex term corresponds to $\phi_{sig}(\omega) - \phi_{LO}(\omega) + \omega t_4$, where t_4 is initially approximated by the time delay between pulses $\mathbf{k_3}$ and LO, so that the ωt_4-term can be subtracted. Assuming a Fourier transform limited pulse (with a flat phase), ϕ_{LO} is neglected[2] (cf. also phasing procedure below). Thus, only the phase of the signal ϕ_{sig} remains, which is combined with the spectral amplitude $|E_{sig}(\omega)|$ to yield the frequency-domain electric field

$$E_{sig}(t_1, t_2, \omega_3) = |E_{sig}(t_1, t_2, \omega_3)| \mathrm{e}^{-i\phi_{sig}(t_1, t_2, \omega_3)} \tag{4.3}$$

that is related to the third-order nonlinear polarization by

$$E_{sig}(t_1, t_2, \omega_3) \propto \frac{i\omega_3}{n(\omega_3)} P^{(3)}(t_1, t_2, \omega_3) \tag{4.4}$$

where $n(\omega_3)$ is the frequency-dependent refractive index of the medium (which is neglected). Via the relation

$$S_{2D}(\omega_1, t_2, \omega_3) = \int_{-\infty}^{\infty} iP^{(3)}(t_1, t_2, \omega_3) \mathrm{e}^{i\omega_3 \tau} \mathrm{d}t_1 \tag{4.5}$$

a division of $E_{sig}(t_1, t_2, \omega_3)$ by ω_3 and a Fourier transformation with respect to t_1 gives the desired two dimensional spectrum in frequency-frequency space.

Due to the aforementioned uncertainty in the exact timing between the LO pulse and the signal, in the final data-analysis the projection slice theorem is applied, which relates the projection of the real part of the complex 2D spectrum onto the ω_3-axis to a frequency resolved pump-probe spectrum [20]. For recording pump-probe spectra, $\mathbf{k_1}$ is used as pump and $\mathbf{k_3}$ as probe pulse (other beams are blocked). The pump-probe spectrum is given by the difference in intensity of the probe beam with and without the pump beam (during the measurement, the pump beam is periodically blocked with a computer controlled electromechanical shutter). In analogy to the approach outlined by T. Brixner *et al.* [68], a second CCD-spectrometer employed (CCD 2 in Fig. 4.3), which can be read-out simultaneously with the first, as a reference to eliminate intensity fluctuations in the probe beam. This is done by taking a reflection of the compensation plate (cf. Fig. 4.3). The pump-probe spectrum is given by [68]

$$I_{PP}(t_2, \omega_3) = \left(\frac{I_{pu}(\omega_3)}{I_{pu}^{ref}(\omega_3)} - \frac{I_0(\omega_3)}{I_0^{ref}(\omega_3)} \right) \frac{I_{pu}^{ref}(\omega_3) + I_0^{ref}(\omega_3)}{2\sqrt{I_0(\omega_3)}} \tag{4.6}$$

where t_2 denotes the pump-probe delay, I_{pu} and I_0 are the intensities of the probe beam

---

[2] In principle, ϕ_{LO} could be determined by ZAP-SPIDER.

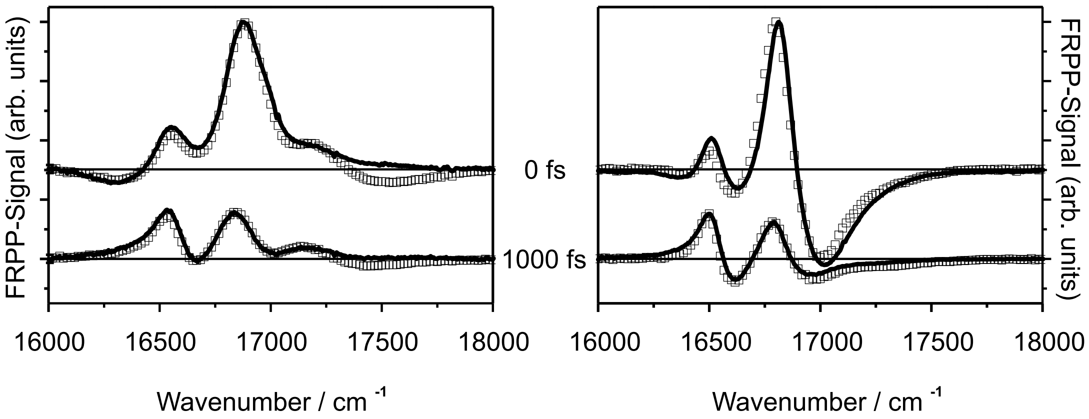

Fig. 4.8: Projections of "phased" 2D spectra (solid lines) for a t_2-delay set to 0 respectively 1000 fs in comparison with spectrally resolved pump-probe data (squares). Excitation vertical to the flow of a wire guided jet is depicted on the left, excitation parallel to the flow on the right side. The data is discussed in Chapter VII.

with and without the action of the pump, and I_{pu}^{ref} and I_0^{ref} are the corresponding reference beams. The corresponding projection of the real part of the 2D spectrum onto the ω_3 axis is given by

$$I_{2D}(t_2, \omega_3) = \mathrm{Re}\left(\frac{\omega_3}{n(\omega_3)} \int_{-\infty}^{\infty} S_{2D}(\omega_1, t_2, \omega_3) \mathrm{d}\omega_1\right) \quad . \tag{4.7}$$

In order to overlap this projection with the independently measured $I_{PP}(t_2, \omega_3)$ signal, the term $S_{2D}(\omega_1, t_2, \omega_3)$ in the equation above is multiplied by a phase factor $e^{i\phi_c}$, which is varied for best overlap of the two plots[3]. This procedure removes uncertainties in the phase of the LO (ϕ_{LO}) and in the exact delay t_4 between the signal and the local oscillator field. For illustration, Fig. 4.8 shows a comparison of spectrally resolved pump-probe data with projections of the corresponding "phased" 2D spectra at t_2-delays of 0 and 1000 fs.

Sample Handling. During numerous pre-runs and testing of the set-up, nonlinear signals of various dyes in solution have been recorded, initially employing conventional cuvettes for handling liquid samples. Thereby, severe difficulties have been encountered due to formation of thermal gratings and non-resonant signals from the window material of standard flow cells (typically made of Suprasil), which were partly found to be of the same order of magnitude as the desired signals themselves. To circumvent this obstacles, a gravity driven, wire-guided drop jet [83, 84] for circulation of the sample has been employed (cf. Fig. 4.9a). The basic design has been described by M. J. Tauber *et al.* [83] and has been

---

[3] An additional timing correction (t_c), as described in Ref. [68], has been found to be abdicable for data analysis.

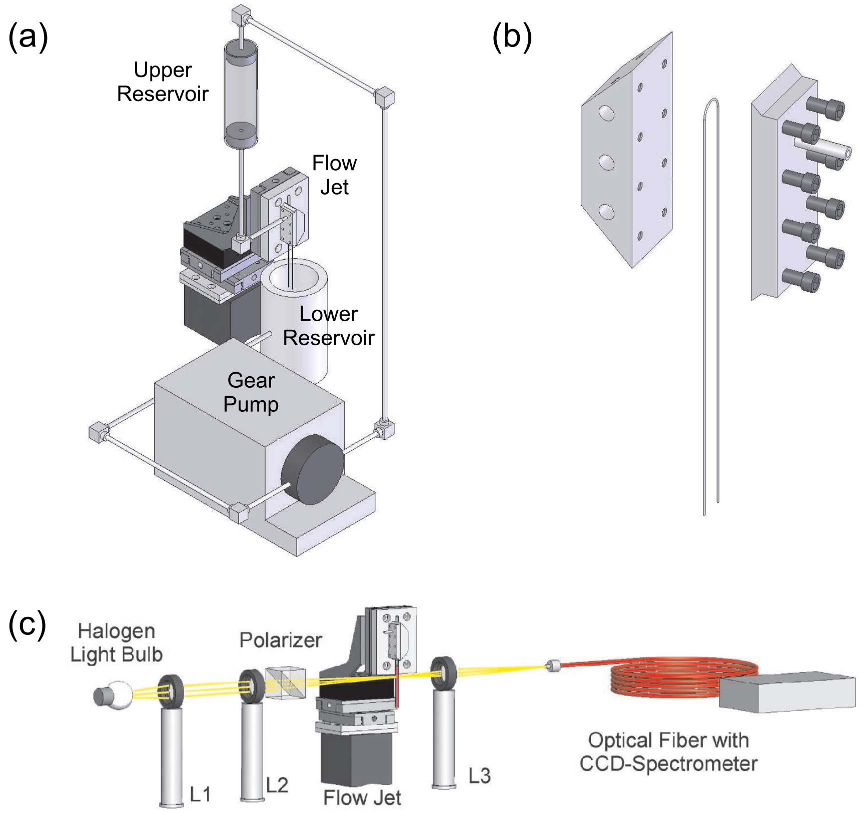

Fig. 4.9: (a) Arrangement for handling liquid samples. (b) Close-up of the wire-guided drop jet. (c) Layout for linear dichroism measurements. A Glan-Thompson polarizer can be adjusted to transmit light parallel respectively orthogonal to the flow direction.

further improved by S. Laimgruber *et al.* [84]. Here, a stainless steel wire with a diameter of 300 μm is arcuated to form an inverse “U”, which is clamped between two rectangular stainless steel plates. The two rectangles are pressed together by eight screws. The liquid enters through a hole in one of the plates and leaves at the bottom of the assembly, forming a film of approx. 200 μm thickness between the two wire ends (cf. Fig. 4.9b). The sample holder is mounted on a manual xyz-stage. The sample solution flows from an upper reservoir through the assembly into a lower reservoir, from where it is pumped back by means of a gear pump that circulates the sample solution at a flow rate of approximately 20 ml/min. The configuration avoids signals from cell windows, obliterates the necessity to compensate the dispersion of any cell material, avoids precipitation of the sample on the cell windows, and generates a stable and pulsation free sample film. All vessels, tubes, and connectors are made of Teflon to resist organic and corrosive solvents.

The presence of an aligning flow is also beneficial for the investigation of mesoscopic samples that tend to align along the flow direction in thin liquid films (cf. Chapter VII). For preferential excitation of selected transition dipole moments, one can simply switch the polarization of the excitation pulses between parallel and vertical to the flow direction. Linear dichroism (LD) spectra, on the other hand, are recorded with a home-built LD spectrometer, consisting of a halogen light source, collimating/focusing optics, a Glan-Thompson polarizer, the wire-guided jet, and a miniature CCD-spectrometer (USB2000, Ocean Optics). The schematic layout of this arrangement is depicted in Fig. 4.9c.

5. PHONON-COUPLING OF A TWO-LEVEL SYSTEM

Although modulations of nonlinear signals by vibrational wavepackets are readily observed in a variety of ultrafast time-resolved experiments, their signatures in two-dimensional electronic spectra have so far only been addressed in a handful of theoretical studies. This chapter reports and analyzes the oscillatory behavior of lineshapes in the two-dimensional relaxation spectra of a perylene-based dye molecule, whose four-wave-mixing signals are strongly modulated by coupling to an underdamped low-frequency vibrational mode. Vibrational wavepacket motion is found to induce a pronounced beating of the anti-diagonal absorptive peak width, accompanied by orientational changes in the dispersive signal part. The effects are reproduced well by simulations based on a Brownian oscillator model, and can be assigned to periodic alternations in the relative amplitudes of rephasing and non-rephasing contributions to the 2D spectra.

Related publications:

Vibrational wavepacket induced oscillations in two-dimensional electronic spectra I. Experiments
A. Nemeth, F. Milota, T. Mancal, V. Lukes, J. Hauer, H. F. Kauffmann, and J. Sperling
Journal of Chemical Physics, *submitted* (2010)

Vibrational wavepacket induced oscillations in two-dimensional electronic spectra II. Theory
T. Mancal, A. Nemeth, F. Milota, V. Lukes, H. F. Kauffmann, and J. Sperling
Journal of Chemical Physics, *submitted* (2010)

Vibronic modulation of lineshapes in two-dimensional electronic spectra
A. Nemeth, F. Milota, T. Mančal, V. Lukeš, H. F. Kauffmann, and J. Sperling
Chemical Physics Letters, **459**, 94 (2008)

5.1 Introduction

Creation of wavepackets in time-resolved spectroscopic experiments takes place if the employed excitation pulses are spectrally broad enough to coherently excite several vibrational and/or electronic levels. Femtosecond (fs) laser pulses meet this criterion for a broad range of molecular systems. In two-dimensional electronic spectroscopy (2D-ES), three femtosecond laser-pulses are incident on the sample and the emitted signal field is characterized in terms of amplitude and phase. The frequency domain 2D correlation spectrum corresponds to a Fourier transform of the induced polarization with respect to t_1 (time-separation between the first two pulses) and the detection time t_3 (the time elapsed after the third pulse). An additional time-delay t_2 between the two observation windows, separating the second and third pulse, can be used to measure the ongoing correlation loss of transition frequencies due to, e.g., system-bath interactions. Given the system under study features a vibronic multi-level structure, a t_2-sequence of two dimensional spectra allows to follow the dynamics of electronic and/or vibrational populations and/or coherences created by the first two interactions. The signatures of electronic coherences, as traced in two-dimensional electronic spectra, have recently received considerable theoretical [85, 86, 87, 88, 89, 90] and experimental [25, 27] attention. Using 2D electronic spectroscopy, quantum coherence during energy transport in a natural photosynthetic complex has been demonstrated, and suggested to increase the efficiency of the transfer process [25]. An assignment of the observed spectral modulation to an excitonic wavepacket motion was made, based on a good agreement of the experiment with the predictions of an excitonic model [85].

In general, however, contributions of vibrational wavepacket motion cannot be excluded and it is therefore of considerable interest to study the coherent vibrational case separately. Modulations of four-wave-mixing signals due to intramolecular vibrations are ubiquitous in femtosecond time-resolved experiments, and readily observed, e.g., in transient grating (TG) or three-pulse photon-echo peak-shift (3-PEPS) measurements on a variety of molecular systems (see, e.g., Ref. [91] and [92]). On the other hand, coherent vibrational motion has not yet been directly addressed in experimental electronic two-dimensional studies, and theoretical calculations explicitly including a manifold of vibrational states are rare [93, 87, 88], which motivates the present work. Since the temporal evolution of the 2D pattern is expected to become increasingly complex in the presence of several high-frequency

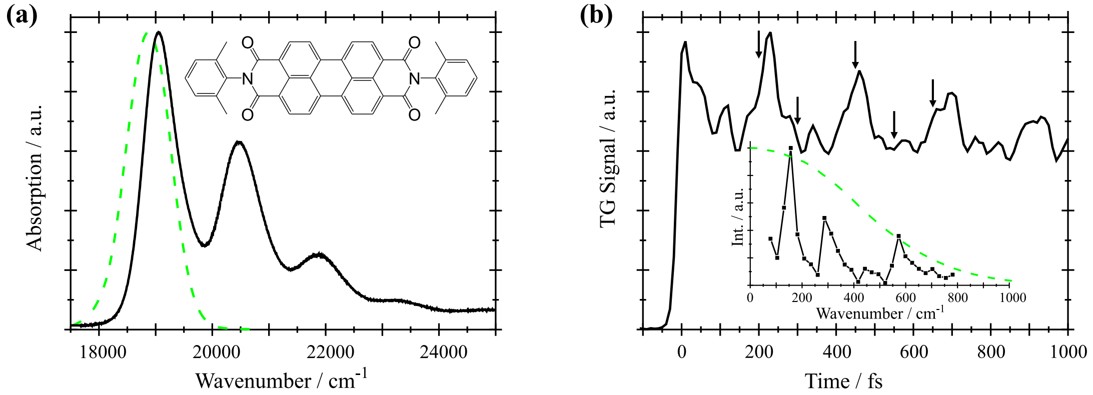

Fig. 5.1: (a) Chemical structure (inset) and the absorption spectrum of PERY in toluene (solid line). The dashed line shows the laser pulse spectrum. (b) Normalized transient grating signal of PERY (solid line) and the Fourier transform of the oscillating signal components (inset; the pulse-bandwidth is shown as dashed line for comparison). Vertical arrows indicate the t_2-delays for the 2D spectra shown in Fig. 5.2

vibrations, a simple system coupled to preferably only a few underdamped modes is desirable for a first-principle study. Thus, for the present study, the well characterized molecular dye N,N'-bis(2,6-dimethylphenyl)perylene-3,4,9,10-tetracarboxylicdiimide (PERY) has been chosen (cf. Fig. 5.1).

The linear absorption spectrum of PERY in solution (Fig. 5.1a) is characterized by a progression of a high-frequency mode (1410 cm^{-1}). Upon electronic excitation, the spectral region of its fundamental ($S_0^{\nu=0} \rightarrow S_1^{\nu=0}$) transition can be selected and entirely covered by the spectral bandwidth of routinely available sub-20 fs laser pulses. As demonstrated by extensive studies in several solvents [91, 92], under these excitation conditions, the third-order spectroscopic signals of PERY experience large amplitude modulations, dominated by coupling of the electronic transition to a low-frequency 140 cm^{-1} vibrational mode (cf. Fig. 5.1b, which shows typical transient grating data). The associated beating period of 240 fs allows to compare 2D-ES spectra at well-separated maxima, minima, rising, and trailing edges of the oscillating nonlinear signal, which minimizes obstructions due to the finite temporal resolution in the experiment. 3-PEPS studies on PERY in toluene have shown the major part of solvent relaxation to be completed on an ultrafast timescale ($t_2 \leq 50$ fs) [92]. Thus, one can expect solvation-induced shifts in the electronic transition energy (caused by a dynamic Stokes shift) to be small only, which is advantageous for analyzing variations in the 2D lineshape.

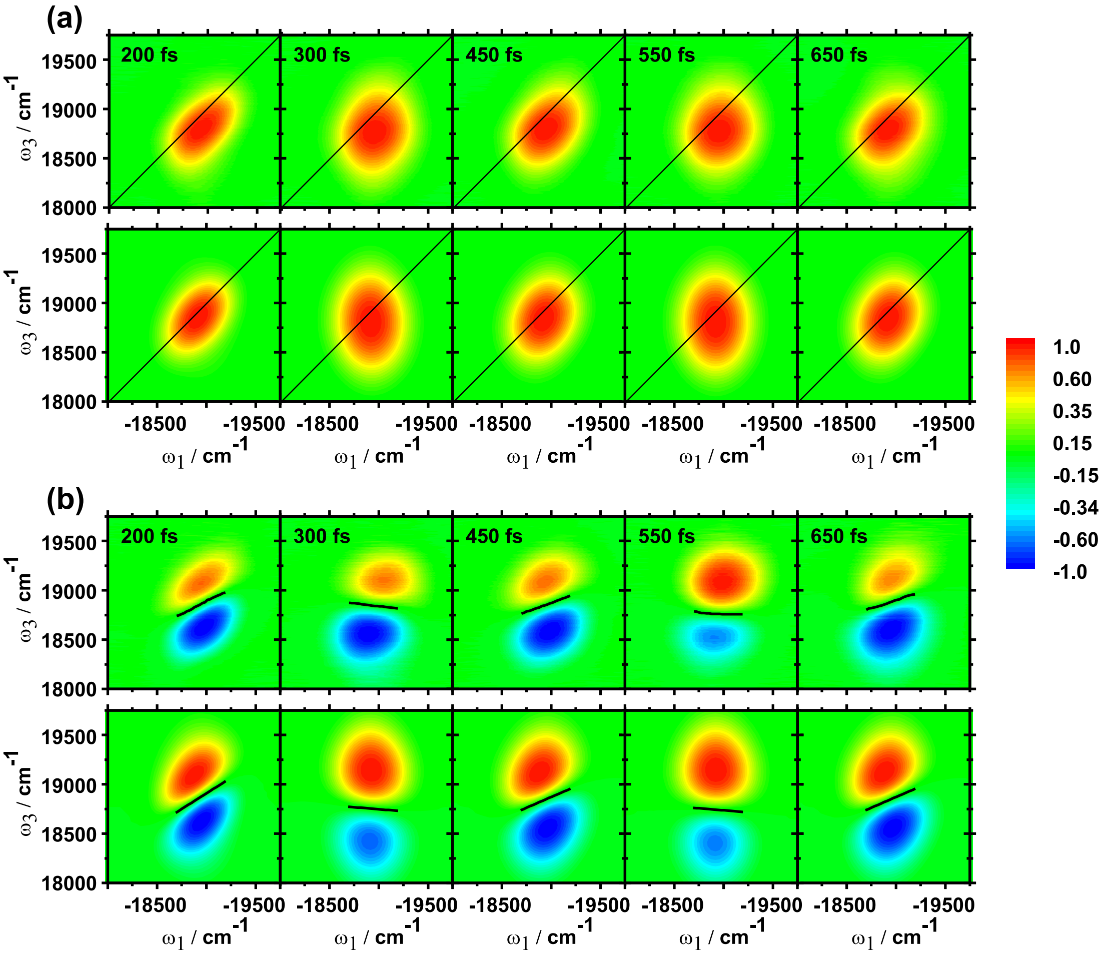

Fig. 5.2: (a) Absorptive and (b) dispersive experimental (upper rows) and calculated (lower rows) 2D electronic spectra of PERY in toluene. From left to right, the panels show the absorptive (dispersive) signal at a t_2-delay of 200, 300, 450, 550, and 650 fs (cf. also Fig. 5.1b). All spectra are normalized to the respective maximum absolute value, the color scale on the right applies for both (a) and (b). Diagonal lines are shown in the absorptive spectra; the black lines in the dispersive signal parts indicate the zero-crossings between positive and negative contributions.

5.2 Experiment and Results

PERY is purchased from Sigma-Aldrich and used as received. Solutions ($c = 3 \cdot 10^{-4}$ M) are prepared with spectrophotometric grade toluene (Uvasol, Merck). The 2D spectra are obtained by scanning the t_1-delay from -100 fs to +100 fs with a resolution of 0.65 fs, thus fulfilling the Nyquist sampling criterion for this frequency regime (approximately 1.77 fs). After the signal analysis procedure, the spectra in Fig. 5.2 feature a frequency resolution of 26 cm^{-1} in ω_1 respectively 3.3 cm^{-1} in ω_3.

A sequence of relaxation spectra is recorded for t_2-delays scanned in 50 fs steps from 0 to 800 fs. Three additional measurements are performed at delays close to the maxima of the transient grating signal (225, 475, and 675 fs, respectively). Since the main interest here lies in extracting dynamical features, the following discussion is focused on the data for nonzero t_2-delays. Periodic changes in the absorptive and dispersive 2D lineshapes are illustrated in Fig. 5.2a, which shows the results at five selected delay times close to the first three recurrence maxima of the TG signal, and the minima in between.

At all delays, the coordinates of the absorptive peak maxima are located in the $|\omega_1| > \omega_3$ triangular signal part and show weak variations within a range of $\approx$ 50 cm^{-1} only. As perceived from inspection of the top row in Fig. 5.2a, the ellipticity of the absorptive signal peak is subject to a periodic change. For t_2 = 200/450/650 fs, the absorptive lineshapes are of pronounced elliptic shape, with the major of the ellipse slanted towards the diagonal. On the other hand, at t_2 = 300 fs/550 fs, the form of the 2D peaks is more circular, and the major of the ellipse is oriented almost parallel to the ω_3-axis. Due to two contributions of opposite sign, the spectral changes are even more pronounced in the dispersive part of the 2D-ES signal (cf. top row in Fig. 5.2b). Both contributions experience an alternating narrowing and widening (along ω_3) that is in-phase with the vertical stretching of the absorptive peaks. Further, the slope of the zero-crossing between positive and negative signal contributions (nodal line) experiences strong changes in its orientation. The signal minima/maxima thereby oscillate out-of-phase to each other, experiencing a pendular type of motion along the ω_1-coordinate.

The results of a quantitative analysis, performed for every single 2D-ES spectrum of the t_2-sequence, are shown and compared to the TG signal in Fig. 5.3. Following a recently proposed procedure, the changes in the ellipticity of the absorptive 2D signal part are quantified in a straightforward way by determining the diagonal and anti-diagonal widths at a $1/e$ peak-height [25]. As seen by comparing Fig. 5.3b and c, the diagonal widths generally exceed the anti-diagonal ones, and show only a weak dependence on the time-delay, increasing slightly at t_2-values that correspond to the maxima of the TG signal. In contrast, the anti-diagonal peak widths are sharply decreased at the corresponding t_2-delays. This counter-evolution is mainly responsible for the strong modulation of the diagonal to anti-diagonal peak-width ratio (cf. Fig. 5.3d), whose functional form is remarkably close to the TG signal. The nodal line in every individual dispersive 2D spectrum is constructed from the experimental data using a set of vertical ($|\omega_1| = const.$) cuts in the region 18700 cm^{-1} < $|\omega_1|$ < 19200 cm^{-1}. For each cut, the zero-crossing between negative and positive signal contributions is evaluated by interpolation along ω_3. The slope of the nodal line is then

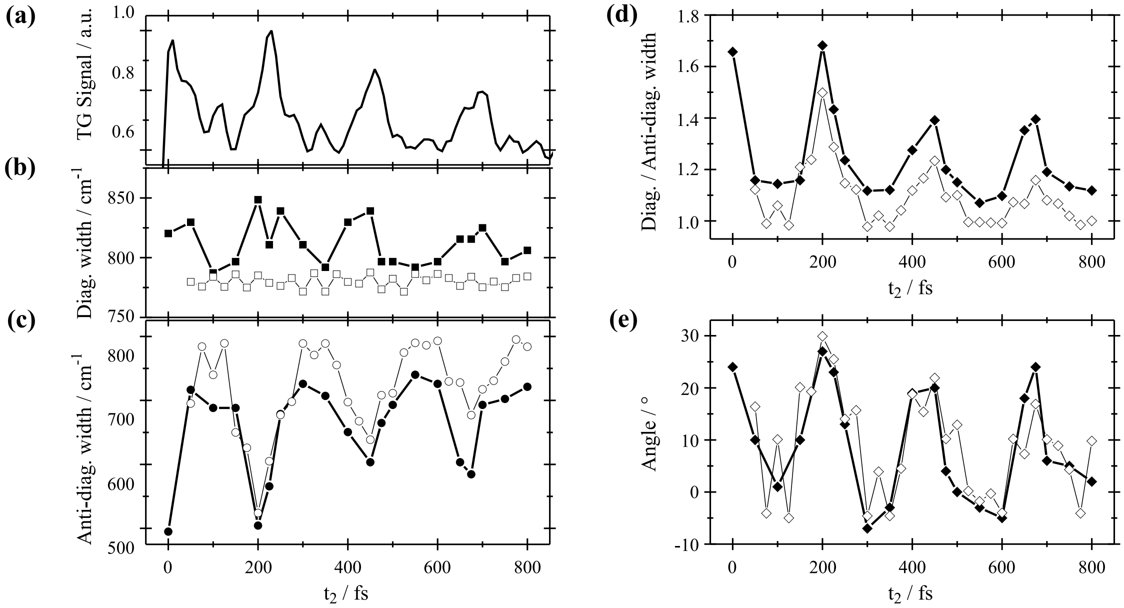

Fig. 5.3: A clip of the transient grating signal (a) compared to oscillations in the 2D spectral lineshape (b-e). Plots (a)-(c) share the same abscissa. Full symbols refer to experimental data, open symbols to calculations. Figs. (b)-(d) show the t_2-dependency of the (b) diagonal and (c) anti-diagonal width of the absorptive 2D peak, and (d) the corresponding evolution of the diagonal/anti-diagonal peak width ratio. (e) shows the angles of the nodal line in the dispersive 2D signal with respect to the ω_1-axis.

determined by fitting the resulting set of $(|\omega_1|, \omega_3)$ coordinates to a first order polynomial. As shown in Fig. 5.3e, the orientation of the nodal line shows pronounced changes over a range of 30°, and partly experiences a sign inversion at points were the absorptive peaks acquire circular shapes.

5.3 Simulations and Discussion

Tough the oscillation of the 2D lineshape is qualitatively similar to the one observed for the coherent evolution of electronic states [93, 85], it originates form a low-frequency vibrational beat in the present case. To substantiate this interpretation of the data in the following, theoretical simulations of the 2D spectra of PERY are performed in the impulsive limit, applying standard semi-classical second order cumulant expansion treatment of the electron-phonon interaction. PERY is treated as an electronic two-level system interacting with intramolecular as well as solvent vibrational modes. For both the overdamped solvent modes and the underdamped oscillatory modes the Brownian oscillator model is employed [10]. For the third-order response functions which are used to calculate the nonlinear signals the standard textbook expressions are used [10]. The response of a two-level electronic system is composed of four different response functions, usually denoted as R_1, R_2, R_3, and R_4, that are functions of the delays between three successive interactions of the system with an incident electric field. The incident field, in turn, enters into the total nonlinear signal via triple convolution with the response functions. Full expressions for the third order nonlinear signal can be found, e.g., in Ref. [68].

In the impulsive limit, the 2D spectrum is formally composed of two parts: One contribution where pulse $\mathbf{k}_1$ arrives at the sample before pulse $\mathbf{k}_2$ ($t_1 > 0$), and another contribution where $\mathbf{k}_2$ precedes $\mathbf{k}_1$ ($t_1 < 0$). In the first case, the signal electric field is proportional to the sum of the response functions $E_R(t_1, t_2, t_3) \propto R_2(t_1, t_2, t_3) + R_3(t_1, t_2, t_3)$, while in the second case, the signal field reads $E_{NR}(t_1, t_2, t_3) \propto R_1(t_1, t_2, t_3) + R_4(t_1, t_2, t_3)$. In both cases, delay t_1 is taken as an absolute value of the delay between pulses $\mathbf{k}_1$ and $\mathbf{k}_2$. The signal $E_R(t_1, t_2, t_3)$ features the well-known rephasing of the photon-echo, i.e. its phase evolves with mutually opposite signs during delays t_1 and t_3. This part of the signal will be denoted as rephasing part. In $E_{NR}(t_1, t_2, t_3)$, on the other hand, the phase evolves with the same sign during both delays, consequently the signal has no rephasing capability. Based on the rephasing and the non-rephasing part of the signal, a two-dimensional spectrum in frequency domain can be defined as

$$S(\omega_1, t_2, \omega_3) = S_R(\omega_1, t_2, \omega_3) + S_{NR}(\omega_1, t_2, \omega_3), \tag{5.1}$$

where

$$S_R(\omega_1, t_2, \omega_3) = \int_0^\infty \int_0^\infty dt_1 dt_3 E_R(t_1, t_2, t_3) e^{-i\omega_1 t_1 + i\omega_3 t_3} \tag{5.2}$$

and

$$S_{NR}(\omega_1, t_2, \omega_3) = \int_0^\infty \int_0^\infty dt_1 dt_3 E_{NR}(t_1, t_2, t_3) e^{+i\omega_1 t_1 + i\omega_3 t_3} \quad . \tag{5.3}$$

Since the spectral and temporal width are Fourier related quantities, the observable spectral window in a 2D experiment is inversely proportional to the pulse duration. To account for this effect, one has to recall that the 2D spectrum is a double Fourier transform of the third order signal, which in turn is a triple convolution of the response function with the electric fields of the pulse sequence. Utilizing the fact that the Fourier transform of a convolution of two functions results in a product of their respective Fourier transforms, the effect of the finite excitation bandwidth can be incorporated [94]. Assuming the response functions to vary only slowly with t_2, a correcting factor

$$f(\omega_1, \omega_3) = [A(\omega_1 - \Omega)]^2 A(\omega_3 - \Omega) \tag{5.4}$$

which multiplies the impulsive spectrum can be introduced. In the expression above, $A(\omega)$ is the Fourier transform of the slowly varying temporal envelope of the laser pulse, and Ω is the central frequency of the pulses. The apparent asymmetry of Eq. 5.4 in frequencies ω_1 and ω_3 mirrors the fact that *two* interactions of the system with the electric field are needed to reach the population period (time interval t_2) of the experiment, whereas the photon-echo signal is stimulated by a *single* interaction. In the simulations discussed below, Gaussian pulses with durations of 21 fs are assumed.

The system parameters used for the simulations are obtained by fitting the diagonal and the anti-diagonal width of the absorptive, and the tilt of the nodal line of the dispersive parts of the 2D spectrum for times $t_2 = 200$, 300, 450, and 550 fs. Although only these four points are fitted (using the least square non-linear minimization algorithm from the Matlab optimization toolbox), a good qualitative agreement at all population times is achieved. In order to restrict the number of minimization parameters, only the reorganization energies of two overdamped solvent modes (with correlation times of $\tau_c^{(1)} = 150$ fs and $\tau_c^{(2)} = 650$ fs) and two underdamped modes (with frequencies of $\omega_{osc}^{1)} = 143$ cm^{-1} and $\omega_{osc}^{(2)} = 575$ cm^{-1}) are varied. All other modes are neglected in this calculation. In particular, any fast oscillatory modes of PERY do not contribute to the 2D spectrum, because their spectral features lie outside the observation window set by the laser pulse spectrum. The correlation times $\tau_c^{(1)}$, and $\tau_c^{(2)}$ are taken from Ref. [95], while the oscillator frequencies $\omega_{osc}^{(1)}$, and $\omega_{osc}^{(2)}$ are extracted from TG measurements. Within these limitations, best results are obtained with solvent reorganization energies of $\lambda_{solv}^{(1)} = 39$ cm^{-1} and $\lambda_{solv}^{(2)} = 106$ cm^{-1}, and reorganization energies of the intramolecular modes of $\lambda_{osc}^{(1)} = 110$ cm^{-1} and $\lambda_{osc}^{(2)} = 84$ cm^{-1}, respectively.

Results of the numerical simulations are shown in the bottom rows of Fig. 5.2a and b. Closer inspection of the figures reveals very good congruity with the experimental spectra. A detailed comparison of experimental and simulated values is presented in Fig. 5.3b-e. In fact, the positions of the beating maxima and minima, the magnitude of both the diagonal (Fig. 5.3b) and the anti-diagonal (Fig. 5.3c) widths, the relative amplitudes of their oscillations, and the trend of the tilt angle (Fig. 5.3e), including the negative sign of the angle at certain population times, are fairly well reproduced. The good correspondence of theoretical and experimental results strongly suggests that the observed modulation of the 2D spectra indeed originates from a slow vibrational mode.

5.4 Analytical Considerations

The qualitative agreement between experiment and theory (on the basis of numerical simulations) motivates to proceed to an analytical analysis to gain further understanding of the nature of the vibrational effects in 2D electronic spectra. To this end, a two-level electronic system interacting with a single underdamped oscillatory mode (frequency $\omega_{osc} = 140\,\mathrm{cm}^{-1}$ and reorganization energy $\lambda_{osc} = 80\ \mathrm{cm}^{-1}$) and a single solvent mode (correlation time $\tau_c = 150$ fs and reorganization energy $\lambda_{solv} = 100\,\mathrm{cm}^{-1}$) is assumed in the following. These values are of the same characteristic magnitude as in the calculations above. Starting from the same theoretical point as in the numerical calculations (the third order response functions), a separation of the vibrational part of the response from the one of the overdamped solvent mode is performed. Because the response functions R_n have the form of an exponential function of a sum of g functions of different time arguments (see, e.g., Ref. [10]), the separation can be performed considering the line broadening function $g(t)$ as the sum of vibrational and solvent contributions

$$g(t) = g_{solv}(t) + g_{vib}(t) \qquad . \tag{5.5}$$

Thus, each response function R_n $(n = 1, \ldots, 4)$ can be written as a product of two contributions $R_n(t_1, t_2, t_3) = R_n^{solv}(t_1, t_2, t_3) R_n^{vib}(t_1, t_2, t_3) e^{-i\omega_{eg}(t_1 \pm t_3) - i\lambda_{vib}(t_1 \pm t_3)}$, where the plus sign in the exponent corresponds to the non-rephasing and the minus sign to the rephasing part of the 2D spectrum. Given time t_2 is longer than the solvent correlation time τ_c, the solvent response becomes t_2-independent and can be written as $R_n^{solv}(t_1, t_2, t_3) = R_n^{(0)}(t_1, t_3)$. It is further assumed that $g_{vib}(t)$ of the underdamped vibrational mode can be approximated as

$$g_{vib}(t) = i\lambda t + i\frac{\lambda}{\omega} \sin \omega t + \frac{\lambda}{\omega} \Xi(T)[1 - \cos \omega t] \tag{5.6}$$

where $\Xi(T) = \coth(\hbar\omega_{vib}/2k_B T)$, and T is the temperature [10]. Further, in Eq. 5.6, the damping of the vibrational mode is assumed to be negligible. Using again the properties of the response functions R_n, one can expand R_n in terms of the Huang–Rhys factors $\frac{\lambda}{\omega}$. This leads to

$$R_n^{vib}(t_1, t_2, t_3) \approx 1 + \frac{\lambda}{\omega} F_n(t_1, t_2, t_3) \tag{5.7}$$

where F is a function containing only sines and cosines of the arguments t_1, t_2, t_3, $t_1 + t_2$, $t_2 + t_3$, $t_1 + t_3$, and $t_1 + t_2 + t_3$. Using trigonometric transformations F can be written as

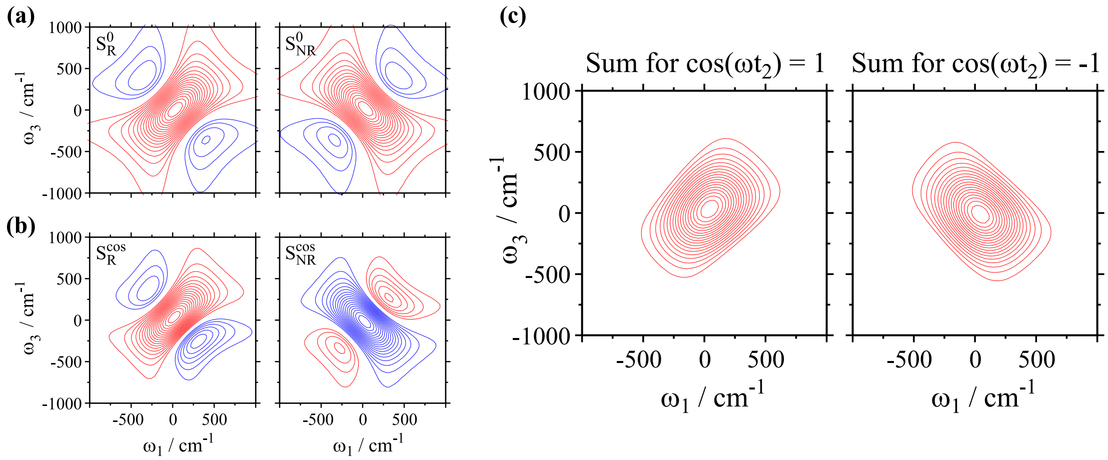

Fig. 5.4: Components of the two-dimensional spectrum of an electronic two-level system interacting with a single overdamped and a single underdamped Brownian mode at room temperature. The parameters for the simulation are given in the text. (a) shows the stationary rephasing and non-rephasing components (S_R^0 and S_{NR}^0, respectively). (b) illustrates the rephasing and non-rephasing prefactors of $\cos\omega t_2$ (S_R^{cos} and S_{NR}^{cos}, cf. Eq. (5.10)). (c) presents the sum of the stationary and cosine contributions for $\cos\omega t_2 = 1$ (left), respectively -1 (right). Every figure is normalized to the maximum of the absolute value (0.5 for stationary, 0.19 for cosine, and 1.0 for the sum).

$$F_n(t_1, t_2, t_3) = K_n(t_1, t_3) + H_n(t_1, t_3)\cos(t_2) + G_n(t_1, t_3)\sin(t_2) \tag{5.8}$$

where the complete t_2-dependence is condensed into the sine and cosine functions (cf. Appendix). The derivation of the functions $K_n(t_1, t_3)$, $H_n(t_1, t_3)$, and $G_n(t_1, t_3)$ is straightforward, and results in expressions which are sums of sine and cosine terms of the arguments ωt_1, ωt_3, and $\omega(t_1 + t_3)$. Thus, the total response function R_n can be written as

$$\begin{aligned} R_n(t_1, t_2, t_3) &= R_n^{(0)}(t_1, t_3) + R_n^{(0)}(t_1, t_3)K_n(t_1, t_3) \\ &+ R_n^{(0)}(t_1, t_3)H_n(t_1, t_3)\cos(t_2) + R_n^{(0)}(t_1, t_3)G_n(t_1, t_3)\sin(t_2). \end{aligned} \tag{5.9}$$

Combining Eqs. 5.9, 5.1, 5.2, and 5.3, one can write for the 2D spectrum

$$\begin{aligned} S(\omega_1, t_2, \omega_3) &= S_R^0(\omega_1, \omega_3) + S_{NR}^0(\omega_1, \omega_3) \\ &+ \left[S_R^{cos}(\omega_1, \omega_3) + S_{NR}^{cos}(\omega_1, \omega_3)\right]\cos\omega t_2 \\ &+ \left[S_R^{sin}(\omega_1, \omega_3) + S_{NR}^{sin}(\omega_1, \omega_3)\right]\sin\omega t_2. \end{aligned} \tag{5.10}$$

For $t_2 = \frac{n\pi}{\omega}$, i.e. where $\sin\omega t_2 = 0$, Fig. 5.4 illustrates the characteristic shapes of the contributions (on the right hand side of Eq. 5.10) to the absorptive part of the 2D signal. Fig. 5.4a presents the stationary contributions, S_R^0 and S_{NR}^0, respectively. Fig. 5.4b shows the prefactors of the cosine term in Eq. (5.10) (S_R^{cos} and S_{NR}^{cos}). Fig. 5.4c, finally, presents the sum of all contributions (for times $t_2 = \frac{n\pi}{\omega}$) when $\cos\omega t_2 = 1$ (left), and for $\cos\omega t_2 = -1$ (right), respectively.

One immediately notices that rephasing contributions are elongated along the diagonal of the 2D spectrum, whereas the non-rephasing features are elongated along the anti-diagonal. A striking feature of these partial 2D spectra is the sign inversion of the non-rephasing cosine contribution S_{NR}^{cos} with respect to the corresponding stationary contribution S_{NR}^0. For $\cos\omega t_2 = 1$, the summation thus results in an enhancement of the rephasing part and a decrease of the non-rephasing part of the spectrum, causing an overall elongation along the diagonal. For $\cos\omega t_2 = -1$, one observes enhancement of the non-rephasing part and thus elongation along the anti-diagonal.

For parameters relevant for the present system, the amplitudes of the contributions oscillating with a cosine function are found to be approximately two times larger than the ones oscillating with a sine function, and both are significantly smaller than the stationary contributions. One can therefore expect the most significant changes in the 2D lineshape to oscillate with the cosine of the population time. An evaluation of the rephasing and non-rephasing parts of the experimental absorptive 2D spectra (not shown here) confirms this notion. The amplitudes of the rephasing and non-rephasing parts at population times $t_2 = n\pi/\omega$ are observed to vary without significant changes of their line-shape. Rather, the oscillation of the diagonal and anti-diagonal width is a result of the periodic enhancement and suppression of rephasing and non-rephasing parts with respect to each other.

5.5 Conclusions

The first experimental signatures of vibrational coherence in 2D electronic spectra are presented. They can be assigned to periodic changes of the relative amplitudes of the rephasing and non-rephasing signal parts. Expansion of the vibrational part of the third-order response in terms of the Huang-Rhys factor (λ/ω) shows that these enhancements and suppressions are caused by coherent vibrational motion. For an intuitive understanding of the periodic changes, one has to recall the multi-level structure of the quantum mechanical system. Both the ground and excited electronic states of PERY feature levels spaced by vibrational frequency ω, which is smaller than the bandwidth of the pulses. The first two laser pulses thus not only populate vibrational states, but also excite coherences between these states. During t_2-evolution, these coherences modulate the signal by a factor $\exp(\pm i\omega t_2)$. The second-order cumulant approach permits to comprise this coherent dynamics together with solvent induced damping into the energy gap correlation function. Expanding this function of an underdamped vibrational mode in λ/ω, one finds the most significant changes to oscillate with the cosine of the population time. Given ω is small compared to the electronic energy gap, one finds the rephasing and non-rephasing signal parts to oscillate with opposite phase.

APPENDIX

The vibrational part $R_n^{vib}(t_1,t_2,t_3)$ of the response functions can be approximately written as $R_n^{vib}(t_1,t_2,t_3) = e^{-i\omega(t_3 \pm t_1)} e^{\frac{\lambda}{\omega}F_n(t_1,t_2,t_3)} \approx e^{-i\omega(t_3 \pm t_1)}(1 + \frac{\lambda}{\omega}F_n(t_1,t_2,t_3))$, where the function $F_n(t_1,t_2,t_3)$ consists of three parts. The first, t_2-independent part, $K_n(t_1,t_3)$, is given by

$$K_1(t_1,t_3) = -i[\sin\omega t_1 - \sin\omega t_3] - \Xi(T)[2 - \cos\omega t_1 - \cos\omega t_3] \tag{5.11}$$

$$K_2(t_{1,}t_3) = i[\sin\omega t_1 + \sin\omega t_3] - \Xi(T)[2 - \cos\omega t_1 - \cos\omega t_3] \tag{5.12}$$

$$K_3(t_1,t_3) = i[\sin\omega t_1 - \sin\omega t_3] - \Xi(T)[2 - \cos\omega t_1 - \cos\omega t_3] \tag{5.13}$$

$$K_4(t_1,t_3) = -i[\sin\omega t_1 + \sin\omega t_3] - \Xi(T)[2 - \cos\omega t_1 - \cos\omega t_3] \tag{5.14}$$

The second, cosine-oscillating part, $H_n(t_1,t_3)\cos\omega t_2$, reads

$$\begin{aligned} H_1(t_1,t_3) = {} & \Xi(T)[1 - \cos\omega t_3 - \cos\omega t_1 + \cos\omega(t_1+t_3)] \\ & + i[\sin\omega t_1 - \sin\omega t_3 - \sin\omega(t_1+t_3)] \end{aligned} \tag{5.15}$$

$$\begin{aligned} H_2(t_1,t_3) = {} & -\Xi(T)[1 - \cos\omega t_3 - \cos\omega t_1 + \cos\omega(t_1+t_3)] \\ & + i[\sin\omega t_1 - \sin\omega t_3 - \sin\omega(t_1+t_3)] \end{aligned} \tag{5.16}$$

$$\begin{aligned} H_3(t_1,t_3) = -\Xi(T)[1-\cos\omega t_3 - \cos\omega t_1 + \cos\omega(t_1+t_3)] \\ +i[\sin\omega t_1 + \sin\omega t_3 - \sin\omega(t_1+t_3)] \end{aligned} \tag{5.17}$$

$$\begin{aligned} H_4(t_1,t_3) = \Xi(T)[1-\cos\omega t_3 - \cos\omega t_1 + \cos\omega(t_1+t_3)] \\ +i[\sin\omega t_1 + \sin\omega t_3 - \sin\omega(t_1+t_3)] \end{aligned} \tag{5.18}$$

The third, sine-oscillating part, $G_n(t_1,t_3)\sin\omega t_2$, is given by

$$\begin{aligned} G_1(t_1,t_3) = \Xi(T)[\sin\omega t_3 + \sin\omega t_1 - \sin\omega(t_1+t_3)] \\ +i[1-\cos\omega t_3 + \cos\omega t_1 - \cos\omega(t_1+t_3)] \end{aligned} \tag{5.19}$$

$$\begin{aligned} G_2(t_1,t_3) = -\Xi(T)[\sin\omega t_3 + \sin\omega t_1 - \sin\omega(t_1+t_3)] \\ +i[1-\cos\omega t_3 + \cos\omega t_1 - \cos\omega(t_1+t_3)] \end{aligned} \tag{5.20}$$

$$\begin{aligned} G_3(t_1,t_3) = -\Xi(T)[\sin\omega t_3 + \sin\omega t_1 - \sin\omega(t_1+t_3)] \\ -i[1-\cos\omega t_3 - \cos\omega t_1 + \cos\omega(t_1+t_3)] \end{aligned} \tag{5.21}$$

$$\begin{aligned} G_4(t_1,t_3) = \Xi(T)[\sin\omega t_3 + \sin\omega t_1 - \sin\omega(t_1+t_3)] \\ -i[1-\cos\omega t_3 - \cos\omega t_1 + \cos\omega(t_1+t_3)] \end{aligned} \tag{5.22}$$

The total response can therefore be separated into stationary, cosine-oscillating, and sine-oscillating contributions.

6. SIMULTANEOUS CHARACTERIZATION OF MONOMERIC AND DIMERIC LINESHAPES

Excitonic interactions are investigated at the simplest possible stage of molecular aggregation - the formation of a dimer. Two-dimensional electronic spectra of a prototypical cyanine dye, whose spectral properties in aqueous solution are determined by an equilibrium of monomers and dimers, are presented. Exploiting the broad excitation bandwidth and the high temporal resolution of ultrashort excitation pulses, the experiments allow to characterize simultaneously the spectral lineshapes of the two species in terms of static and dynamic disorder. The distinctly different spectral relaxation dynamics are quantified by a lineshape analysis and compared to impulsive limit simulations employing a Brownian oscillator model. Quantum chemical methods give insight into the interplay between structure and electronic properties of the species involved. The findings are qualitatively in line with theoretical considerations, which predict the energetic fluctuations of delocalized excitonic states to be reduced as compared to site-localized excitations.

Related publication:

Two-Dimensional Electronic Spectra of an Aggregating Dye: Simultaneous Measurement of Monomeric and Dimeric Lineshapes
A. Nemeth, V. Lukes, J. Sperling, F. Milota, H. F. Kauffmann, and T. Mancal
Physical Chemistry Chemical Physics, **11**, 5986 (2009)

6.1 Introduction

Given inter-molecular interactions in an ensemble of molecular absorbers are weak, electronic excitations can be assumed to be site-localized, as electronic couplings will act as a small perturbation of the system only. If, on the other hand, the electronic coupling strengths between molecules become comparable to (static and/or dynamic) fluctuations of their site-transition energies, excitations may become coherently delocalized, and collective excited states (excitons) with distinct spectral properties are formed [29]. Experimentally, this phenomenon has been reported already in 1936 independently by G. Scheibe and E. E. Jelley [96, 97]. E.g., for the well-studied case of a linear periodic arrangement of molecules, a new dominant absorption band appears, which, depending on the mutual orientation of molecular transition dipoles, is either red-shifted (J-aggregates) or blue-shifted (H-aggregates) to the monomer transition.

Being projected onto a single frequency axis, detailed informations on inter-molecular coupling strengths, excitation delocalization effects, and homogenous/inhomogeneous contributions to the spectral lineshape remain hidden in linear optical spectra of excitonic systems. Several nonlinear spectroscopies have been designed to selectively probe only homogeneous dynamics by eliminating inhomogeneous contributions [10, 98, 99]. Two-dimensional electronic spectroscopy (2D-ES), in particular, has emerged as the method of choice for investigating inter-molecular interaction strengths and for deepening the comprehension of how properties of individual sites are reflected in the optical response of aggregates. However, apart form a study on a covalently linked oligophenylene-dimer [69], experimental studies so far focused on either dilute solutions of non-interacting dye molecules [22, 61, 66, 59, 94], or on larger complexes, like natural [23, 25, 100] or artificial [101, 102, 103] light harvesters. This is in some contradiction to the popularity of dimers (as the simplest aggregate prototypes) in theoretical studies of excitonic interactions [86, 104, 85, 90], and the following results are considered as a step towards closing this gap.

Analyzing suitable molecular systems that offer straightforward access to control the extent of excitation delocalization, one finds a variety of convenient choices from the class of aggregating cyanine dyes. Due to strong dispersion forces associated with the high polarizability of the chromophore, cyanine dyes (at higher concentrations) tend to form

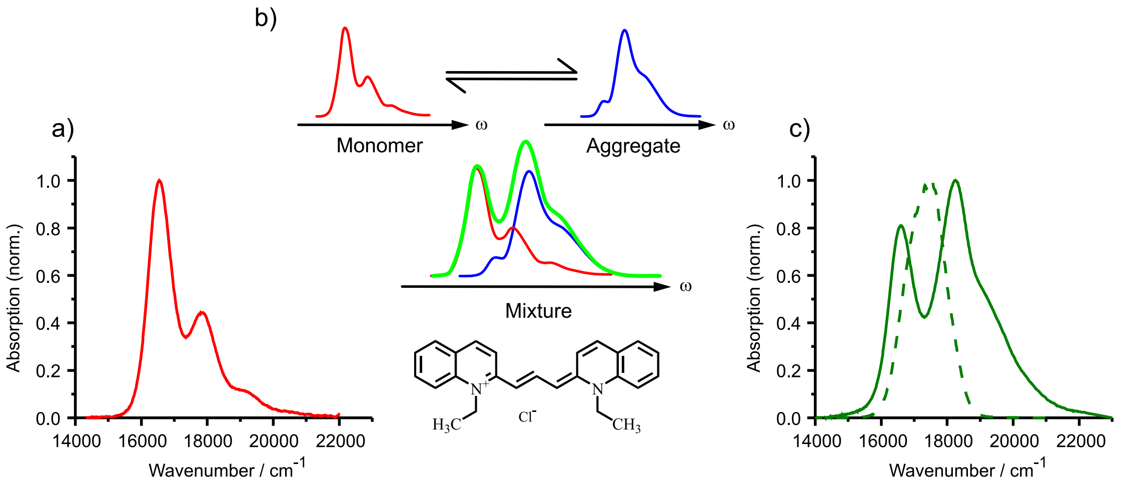

Fig. 6.1: (a) Linear absorption spectrum of Pinacyanol chloride (PIN) in methanol. (b) Schematics of new bands appearing upon aggregation of PIN monomers. The chemical structure of PIN is shown at the bottom. (c) Absorption spectrum (solid line) of an equilibrated mixture of PIN in a water/methanol solution compared to the laser pulse spectrum (dashed line).

aggregates in aqueous solution [105]. The degree of aggregation can thereby be controlled by both solute concentration and/or the polarity of the solvent, which permits to study effects of excitation delocalization at the lowest level of aggregation, by direct comparison of monomeric and dimeric lineshapes in 2D-ES spectra.

The aggregates of Pinacyanol chloride (PIN, cf. Fig. 6.1), a prototypical cyanine dye investigated in the present study, belong to the class of H-aggregates. Fig. 6.1b schematically explains the spectral pattern of the sample that is observed in water-methanol mixtures. According to the common interpretation of the PIN spectrum under conditions of partial aggregation [105], the three new bands in linear absorption (LA) are assigned to the lower and the upper exciton levels of molecular dimers, and an additional blue-shifted band originating from higher aggregates (cf. the aggregate spectrum shown in the upper right corner of Fig. 6.1b). By tuning the solvent polarity, the concentrations of the different species can be adjusted for a double-peaked LA spectrum, referred to as the monomeric and the dimeric absorption maximum in the following (cf. Fig. 6.1c).

In this study, 2D-ES is applied to simultaneously characterize the two spectral bands in terms of underlying dynamic and static disorder, fully exploiting the broad bandwidth and ultrashort duration of the excitation pulses. After a quantum chemical characterization of the electronic properties of monomers and of dimeric molecular arrangements, the experimental data is qualitatively recovered in simulations based on third-order response function theory, employing Brownian oscillators for modeling the lineshapes.

6.2 Experiment and Results

Experimental. Pinacyanol chloride is purchased from Sigma Aldrich and used as received. Solutions with $c = 1.5 \cdot 10^{-4}$ mol/l are prepared with a mixture of water and methanol (37.5 % v/v). The central frequency of the excitation pulses is tuned to 17500 cm^{-1}, to cover both the monomer and the dimer absorption peak. Nonlinear experiments are performed with 10 nJ of energy in each pulse. The observed spectral features are found to remain unchanged also for reduced pulse energies (4 nJ), from which one can conclude that higher order and/or saturation effects do not affect the spectral lineshapes. 2D spectra are obtained by scanning t_1 in the interval ±100 fs in steps of 0.65 fs (for a fixed value of t_2).

It should be mentioned that, even though the excitation pulses are spectrally broad enough to simultaneously investigate the dynamics of both the monomer and the dimer band, they do not cover the entire absorption spectrum of the sample. In other words, when comparing linear absorption features and the 2D electronic spectra, one has to keep in mind that the latter are dressed by the finite bandwidth of the laser pulses. This spectral filter effect affects the extracted diagonal peak widths more than the anti-diagonal ones [93], so that the corresponding numerical values can be taken only as a relative measure. This point becomes further evident if the experimental data is compared to impulsive limit calculations (see below), however, it does not affect the conclusions drawn.

Experimental Results. Fig. 6.2a shows a selection of normalized 2D electronic spectra in amplitude representation, recorded at t_2-delays of 0, 20, 70, 2500, and 10000 fs. The 2D spectra recover the two isolated peaks observed in linear absorption (being related to monomer and dimer signal contributions), and one can clearly perceive the difference in their dynamical evolution. The effects are quantified in Fig. 6.2b (for the monomer peak) and Fig. 6.2c (for the dimer peak), which show the evolution of the diagonal and anti-diagonal peak-widths (determined at the intensity level of $1/e$), and the corresponding diagonal to anti-diagonal peak-width (D/A) ratios for the full sequence of experimentally recorded t_2-delays.

Notably, both species exhibit quite similar characteristics at $t_2 = 0$ fs, with an initial D/A-ratio of 1.7 (cf. Fig. 6.2). For the monomer, however, the anti-diagonal width quickly increases, and, after 70 fs, approaches the value of the diagonal width (the latter remains essentially constant throughout all t_2-delays). Accordingly, the D/A-ratio decreases to 1.1, corresponding to a circular peak shape, which remains almost invariant at increased t_2-delays, indicating only little residual spectral inhomogeneity. The dimer peak, on the other hand, exhibits distinctly different behavior. Being slightly twisted off of the diagonal

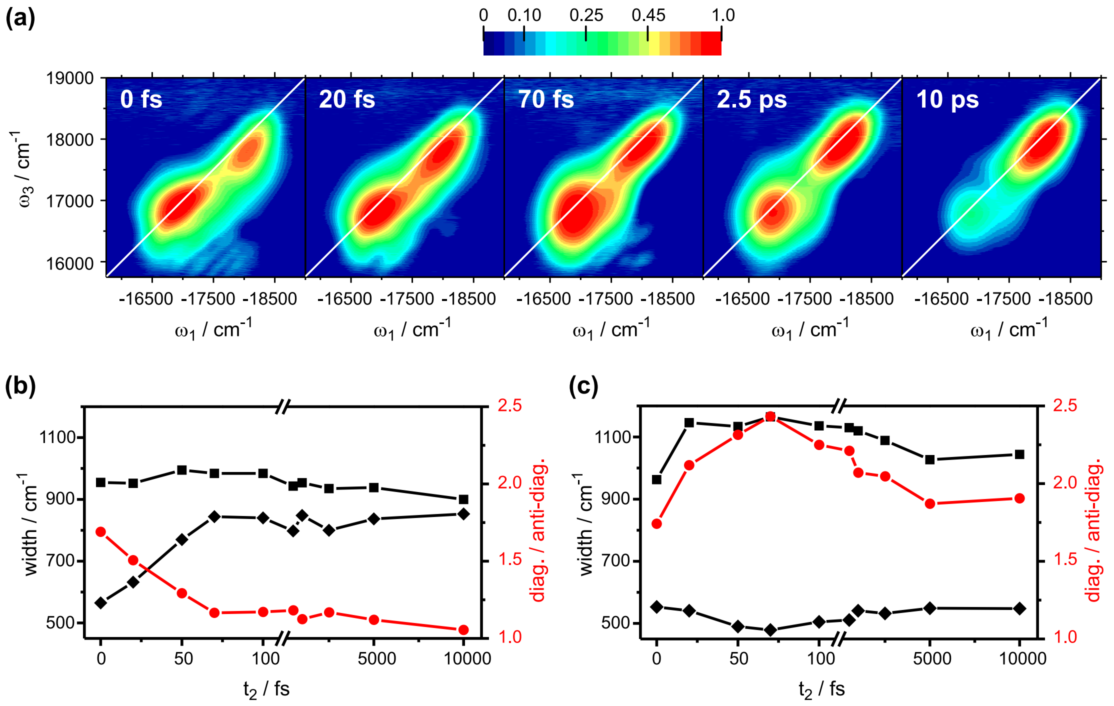

Fig. 6.2: (a) Two-dimensional amplitude spectra of Pinacyanol for t_2-times of 0, 20, 70, 2500, and 10000 fs (from left to right). All spectra are normalized to the respective signal maximum, the color scale is shown on top. The lineshape analysis for the full sequence of 2D spectra is shown separately for the (b) monomeric and the (c) dimeric peak. Squares (diamonds) show the evolution of the diagonal (anti-diagonal) peak-widths; circles (red) show the diagonal to anti-diagonal peak-width ratio.

at $t_2 = 0$ fs, its long axis initially rotates clockwise towards the diagonal. As shown below, this effect can be attributed to interferences between positive and negative signal contributions (in the absorptive signal part). In accordance with this clockwise rotation, the diagonal width of the dimer peak increases, whereas the anti-diagonal width slightly decreases and reaches a minimum after 70 fs (the D/A-ratio is thus increased to 2.4). At later t_2-times, the diagonal width levels off to approximately twice the anti-diagonal width, as indicated by a D/A-ratio of roughly 1.9. It is further apparent from the data shown in Fig. 6.2, that the lifetimes of the two species strongly differ. One observes that the monomer signal has completely vanished after 10 picoseconds (ps), which is in very good agreement with previously reported fluorescence lifetimes [106, 107]. The quick decay is attributed to non-radiative decay channels (associated with torsional motion), that are not open to dimers [108].

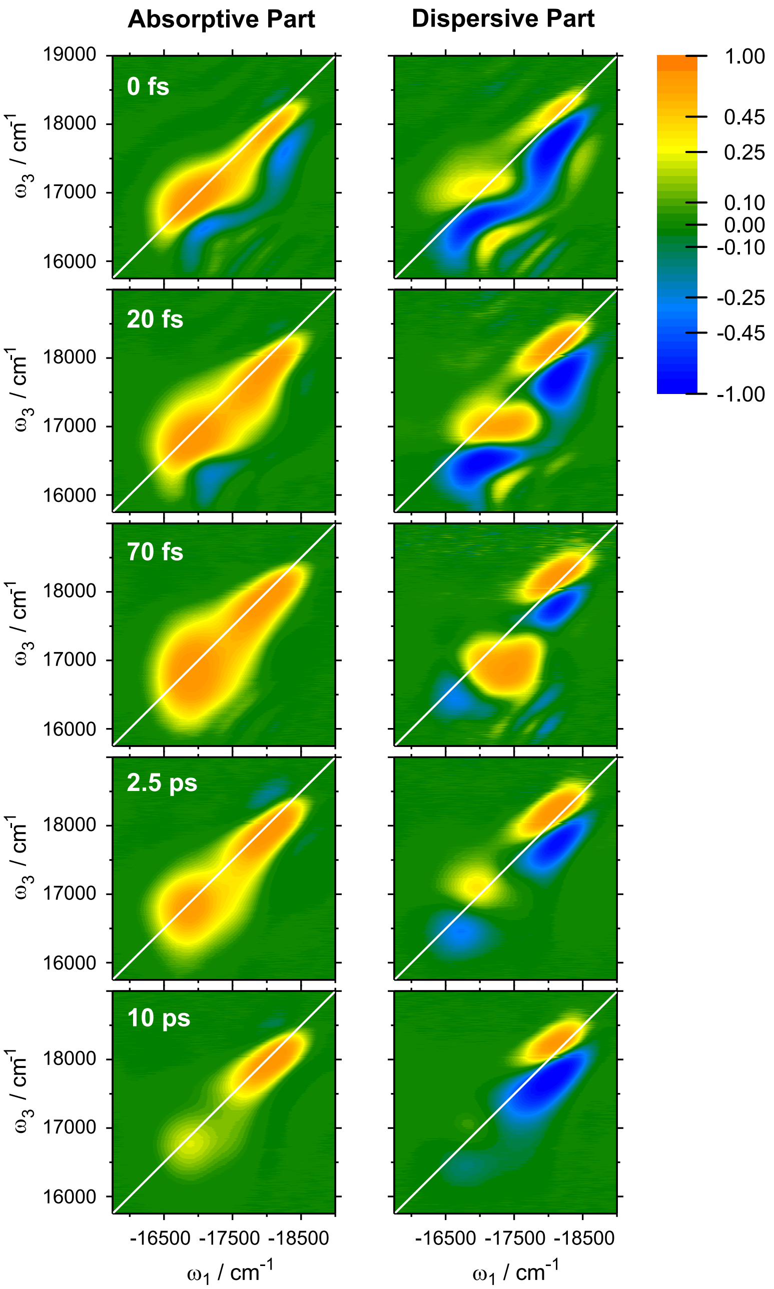

Fig. 6.3: Absorptive (left column) and dispersive (right column) parts of the experimental 2D signal for t_2-times of 0, 20, 70, 2500, and 10000 fs (from top to bottom). All spectra are normalized to the respective maximum absolute value and share the same color scale.

The absorptive parts of the complex 2D signals essentially reflect the characteristics of the amplitude plots (cf. left column in Fig. 6.3). The weak negative features in $|\omega_1| > \omega_3$ (observed for the pulse overlap region $t_2 \leq 20$ fs) are attributed to Liouville space pathways in which correct pulse ordering is not maintained. These negative contributions are responsible for the distorted peak shapes in the amplitude representation. Apart from this notion, the absorptive signals evolve similarly to the amplitude spectra, with the dimer peak maintaining its diagonal elongation and the monomer peak quickly acquiring a circular shape. In the dispersive signal parts, in turn, positive and negative valued contributions are observed for both peaks (cf. right column in Fig. 6.3). In analogy to the D/A-ratio described above, here, it is the slope of the nodal line (separating the positive and negative contributions) that pinpoints the differing spectral characteristics of monomers and dimers. Upon closer inspection of Fig. 6.3, for the monomer, one finds the angle of the nodal line to be initially rotated off from a horizontal orientation by $\approx 30°$ ($t_2 = 0$ fs). Within the first 20 fs, the nodal line becomes parallel to the ω_1-axis, and rotates further clockwise at later times. Contrarily, the orientation of the nodal line for the dimer peak is very similar for all t_2-delays.

6.3 Simulations and Discussion

Quantum Chemical Calculations. To provide a conceptual basis for the simulation of nonlinear signals, a quantum chemical analysis of the structure and absorption properties of the PIN monomers and dimers is carried out. Notably, density functional theory (DFT) has been successfully applied to interpret the structure and optical spectra of various π-conjugated systems, but is numerically limited to a relatively small number of atoms. Therefore, the simulations partly resort to semi-empirical methods that offer a reasonable compromise between reliability of results and computational requirements.

The ground state geometries of the PIN monomers are optimized using DFT as well as the semi-empirical DFTB+ method [109]. For the DFT calculations, which are performed using the Turbomol program [110], the SV(P) basis set [111] and the B3LYP [112] and PBE [113] functionals are employed. Due to numerical problems connected with the geometry optimization of PIN dimers, the possible van-der-Waals structures are calculated using the DFTB+ method only, following the procedure outlined by Aradi *et al.* [109], and under inclusion of dispersion interactions. On the basis of the optimized ground state geometries, the vertical electronic absorption transitions are calculated at the ZINDO level of theory (using the the Gaussian03 package [114]).

The optimized DFTB+ geometries reveal the existence of eight possible conformations; two of them (M_{cis}, M_{trans}) are depicted in Fig. 6.4a. Both of the two most stable conformations have *cis*-orientation (M_{cis}) of the two nitrogen atoms carrying the ethyl chains, and the molecules are almost planar. These two conformations differ only in the mutual orientation

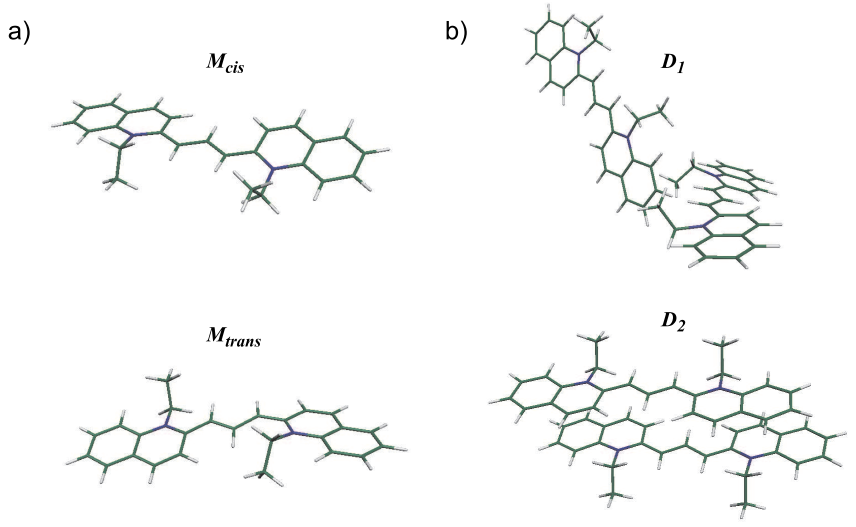

Fig. 6.4: (a) Optimal DFTB+ structures of two out of eight possible monomer structures with *cis*- and *trans*-conformation of the two nitrogen atoms (labeled M_{cis} respectivley M_{trans}). (b) Two out of four possible van-der-Waals dimer structures (D_1, D_2).

of the alkyl groups that are twisted by approximately 8-11° with respect to the central bridge. Further, the energy difference (11 cm^{-1}) between the two structures is practically negligible. The two *trans*-conformations (M_{trans}), on the other hand, are about 1500 cm^{-1} higher in energy with respect to the most stable *cis*-conformation. Comparable results are obtained also by DFT calculations employing B3LYP and PBE functionals. Thus, the dimer structures are analyzed further for *cis*-oriented monomers only. The lowest ZINDO vertical electronic transition of M_{cis} is found at 17123 cm^{-1} and carries an oscillator strength of $f = 1.692$. The transition is of predominantly $\pi - \pi^*$ character (92% of its oscillator strength can be associated with the HOMO to LUMO transition).

As already mentioned, starting geometries for dimer calculations are generated only for *cis*-conformations. On the basis of DFTB+ calculations, one finds four stable van-der-Waals structures; two of them (D_1, D_2) are depicted in Fig. 6.4b. Structure D_1 has a T-shape orientation, where the shortest distance between the nitrogen atoms of the two interacting molecules is 6.2 Å. The sandwich structure D_2, in turn, exhibits the highest π-stacking. In D_2, the interacting molecules are practically co-planar and their distance is ca. 3.5 Å. The remaining two conformations are half-slipped sandwich structures with similar (parallel) monomer orientations. In the following, the sandwich orientation is assumed to be the dominant structural motif also in the condensed phase, and slipped structures to be reflected as inhomogeneous broadening of the associated electronic transition.

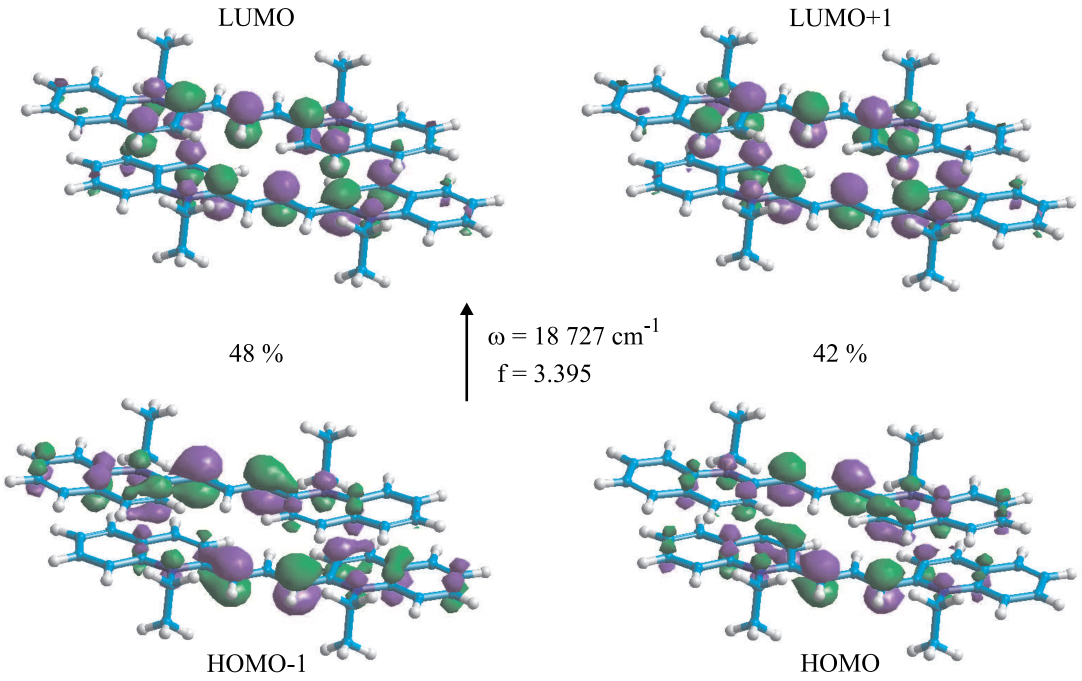

Fig. 6.5: ZINDO orbitals based on the optimal DFTB+ geometry of D_2, depicting the main contributions to the transition at 18 727 cm^{-1}.

As expected for a sandwich-type dimer (D_2), the allowed electronic transition to the first excited state is blue-shifted with respect to the monomer absorption, and located at 18727 cm^{-1}. The oscillator strength of this transition is about twice the oscillator strength of the corresponding monomer transition and amounts to $f = 3.395$. Fig. 6.5 depicts the HOMO and LUMO orbitals that dominate the electronic transition, with HOMO-1→LUMO accounting for 48 %, and HOMO→LUMO+1 accounting for 42 % of the oscillator strength, respectively. In accordance with considerations based on Frenkel exciton theory (predicting a second, red-shifted, forbidden transition for sandwich-type dimers), the quantum-chemical calculations reveal a transition at 14115 cm^{-1} carrying zero oscillator strength. It is important to note that for the three other dimer conformations, electronic excitations are found to be localized on one of the two monomers only. Therefore, the excitation energy coincides with the one of the monomer, and no energetic shift of absorption is observed.

Conceptual Approach to Simulations of 2D Electronic Spectra. In the following, while keeping an eye on the results presented above, the relevant electronic states, intramolecular vibrations, and system-bath coupling parameters that need to be accounted for in simulations of the 2D spectra shall be discussed.

In view of the quantum chemical calculations (which indicate higher lying electronic states to be beyond the experimental excitation bandwidth), is it reasonable to assume that the monomeric spectral band can be represented by an electronic two-level system. In other words, one can assume the Hamiltonian

$$H^{(mon)} = [\epsilon_g + V_g(Q)]|g\rangle\langle g| + [\epsilon_e + V_e(Q)]|e\rangle\langle e| \tag{6.1}$$

where ϵ_g and ϵ_e are the pure electronic excitation energies, and $V_g(Q)$ ($V_e(Q)$) is the nuclear potential energy surface in the electronic ground (excited) state. The electron-phonon interaction can be identified by splitting the above Hamiltonian into pure bath, pure electronic, and interaction terms ($H^{(mon)} = H_{bath} + H_{el} + H_{el-ph}$). This yields

$$H_{el-ph} = \Delta V(Q)|e\rangle\langle e| \tag{6.2}$$

where $\Delta V(Q) = V_e(Q) - V_g(Q) - \langle V_e(Q) - V_g(Q)\rangle$ (therein, $\langle \ldots \rangle$ denotes averaging over the reservoir degrees of freedom). In third-order response function theory, the signatures of both intra-molecular as well as bath modes are comprised in the so-called line-broadening function

$$g(t) = \frac{1}{\hbar^2} \int\limits_0^t d\tau \int\limits_0^\tau d\tau' \langle \Delta V(Q,\tau')\Delta V(Q,0)\rangle \tag{6.3}$$

where the time-dependence of ΔV results from the interaction picture with respect to the bath Hamiltonian H_{bath}. To model both type of effects (intra-molecular and bath modes), the Brownian oscillator model is employed [10], wherein which each mode is specified by its vibrational frequency (ω), its reorganization energy (λ), and its dephasing time (τ_c)[1]. A fast underdamped vibrational mode is introduced according to the progression in linear absorption of PIN monomers (cf. Fig. 6.1a); a second (slow) underdamped vibrational mode is postulated to account for the pronounced dynamics in the time evolution of the 2D monomeric peak (cf. Fig. 6.3). Bath effects are incorporated by an additional overdamped mode. Further, the monomer signal is damped by a relaxation factor to account for the short lifetime of the lower energy band.

Appropriate boundaries are less straight forward to argue for the *aggregated* species, in particular if trying to bridge to an excitonic picture of the dimers' spectral properties. So far, the electronic states of PIN dimers have been experimentally inferred from linear absorption spectra of monomer/dimer-mixtures, by applying iterative fitting procedures

---

[1] In theory, the electronic transition energy obtained from quantum chemical calculations corresponds to the value $\epsilon_e + \lambda - \epsilon_g$.

(in fact, also Fig. 6.1 is based on such an approach) [105]. Accordingly, the two redmost peaks of the aggregate's linear absorption spectrum (cf. Fig. 6.1b) are commonly attributed to the lower and higher one-exciton states of H-type dimers [115, 116, 117, 118]. In the Frenkel exciton picture, the corresponding Hamiltonian (for the dimer) is given by

$$H^{(dim)} = H_1^{(mon)} \otimes 1_2 + 1_1 \otimes H_2^{(mon)} + J\left(|g_1\rangle|e_2\rangle\langle e_1|\langle g_2| + h.c.\right) \tag{6.4}$$

where J is the excitonic resonance coupling and $\otimes$ denotes the direct product of a monomeric Hamiltonian with the unity operator ($1_n = |g_n\rangle\langle g_n| + |e_n\rangle\langle e_n|$) defined on the Hilbert space of the other monomer. The eigenstates of $H^{(dim)}$, the so-called excitonic states $|\alpha\rangle$, are linear combinations of the excited states $|n\rangle$ localized on individual monomers

$$|\alpha\rangle = \sum_{n=1}^{2} c_n^\alpha |n\rangle \tag{6.5}$$

where the coefficients c_n^α are obtained from the diagonalization of $H^{(dim)}$. The transformation from the basis of local states to the basis of the electronic eigenstates also changes the electron-phonon interaction Hamiltonian [39]. In the excitonic basis, the lineshape function transforms to

$$g_\alpha(t) = \sum_{n=1}^{2} |c_n^\alpha|^4 g_n(t) \qquad . \tag{6.6}$$

In the above expression, the $g(t)$-functions are defined according to Eq. 6.3, and the indices n and α refer to states localized on individual monomers respectively the excitonic states in Eq. 6.5. As is well known, the delocalization of electronic excitations (due to mixing of the monomeric electronic states) in molecular aggregates affects the contributions from both static and dynamic disorder to the spectral line shape. For *static* disorder (inhomogeneous broadening), the effect refers to the reduction of spectral inhomogeneity as a result of statistic sampling over independent site energies. The exchange narrowing of *dynamical* fluctuations (homogeneous broadening) [119], on the other hand, will act towards a reduction of the anti-diagonal width in the 2D lineshape of the dimer.

To establish the context with the present study, it should be emphasized that the quantum chemical calculations indicate excitation delocalization ("excitonic behavior") in only one type of dimer (D_2), while electronic excitations are found to remain site-localized for the remaining structures. Accordingly, the linear absorption of the latter will overlap with the absorption of (isolated) monomers, making them indistinguishable in the spectroscopic sense. Further, for the excitonic structure D_2, one finds an energetically lower lying (forbidden) electronic state, however, it is pronouncedly red-shifted to monomer absorption (as expected from Frenkel exciton theory). Therefore, the two redmost peaks of aggregated PIN monomers (cf. Fig. 6.1b) are assumed to originate from *different* species, rather than from the excitonic splitting of electronic states in one and the same dimer. This conclusion is substantiated by the experimental 2D electronic spectra shown in Fig. 6.3. Given the excitonic dimer had an electronic transition in the vicinity of the monomer peak, one would clearly expect the appearance of cross-peaks, as a consequence of a common ground state, and, presumably, from excitation relaxation from the upper to the lower exciton level. Obviously, such cross-peaks do not appear in the experimental 2D spectra[2]. In view of these findings and the fact that, for the experimental excitation bandwidth, the spectral characteristics of the aggregated species are strongly dominated by a single (dimeric) peak, one can again resort to an electronic two-level model (incorporating the dominant dimer transition only).

Simulations and Comparison to Experiment. Absorptive and dispersive 2D electronic spectra, calculated for a t_2-delay of 0, 20, 70, 100, 2500, and 10000 fs, are shown in Fig. 6.6 (cf. Fig. 6.3 for corresponding experimental data). The simulation results are obtained with the model boundaries outlined above, assuming the impulsive limit, and performing an extensive search in parameter space for best agreement with experimental data. Before further discussion, is should be mentioned that the ratio of monomer to dimer concentrations has been initially adjusted to match the experimental linear absorption spectrum. However, keeping this ratio for calculations of nonlinear data, one finds the 2D spectra to be entirely dominated by the dimer peak. Therefore, in Fig. 6.6, the dimer peak has been scaled down (in amplitude) by a factor of 0.3, for better comparability with experimental data. This procedure can be justified as a consequence of the experimentally limited excitation bandwidth, from which quantitatively similar changes in relative peak magnitudes can be expected.

The parameters used to generate the data presented in Fig. 6.6 are summarized as follows. For the monomer, the fast vibrational mode (1350 cm^{-1}) is assigned a reorganization energy of 500 cm^{-1} and a dephasing time of 1 ps. The second underdamped mode is assigned a frequency of 200 cm^{-1}, a reorganization energy of 100 cm^{-1}, and a dephasing time of 1 ps. This (slower) mode accounts for the dynamics observed at early t_2-delays, characterized by oscillations of the amplitude, and diagonal and anti-diagonal widths of the monomer peak. The remaining, overdamped mode, which is introduced to represent bath effects and used to fine-tune the spectral lineshapes, is characterized by a reorganization energy of 150 cm^{-1}, and, like the two underdamped modes, a dephasing time of 1 ps. No significant changes in the simulated data are found upon variation of the latter parameter. The monomer signal is damped using a relaxation factor e^{-Kt_2} (with $K = 0.2$ ps^{-1}), in order to account for the short lifetime of the monomer's excited state and to reproduce the consequent disappearance of the monomer peak.

---

[2] In line with this argumentation, one can attribute negative contributions to the real parts of the 2D spectra (observed at very early times, cf. left column in Fig. 6.3) to pulse overlap effects and/or to electron-phonon interaction effects, rather than to the excited state absorption of excitonic states.

Distinctly different system-bath coupling characteristics need to be assumed for reproducing the behavior of the dimeric peak. In particular, the experimentally observed anti-diagonal width is by far smaller than one would predict from a Frenkel exciton model, i.e., by a straight forward transformation of monomer parameters according to Eq. 6.6. Rather, for reproducing the shape and the t_2-evolution of the dimer peak, one needs to assume a significant inhomogeneous broadening of the excitonic transition (full width at half maximum $\Delta = 600$ cm^{-1}), while including a single overdamped mode only (reorganization energy 50 cm^{-1}). The inhomogeneous broadening contribution enters as an additional term αt^2 (with $\alpha = \Delta^2/16\ln 2$) into the line broadening function. These parameters are found to appropriately account for the small initial anti-diagonal width of the dimer peak (and its comparably large diagonal width), as well as the increase of the anti-diagonal width at longer t_2-delays.

In the simulated 2D spectra, electron-phonon coupling effects are reflected as two dissimilar signatures. First, as a consequence of assuming the impulse limit, the simulated data exhibits vibrational cross-peaks, which are related to the high-frequency mode of the monomer. Under the present experimental conditions, the temporal period of this mode (approximately 25 fs) is comparable to the temporal widths of the excitation pulses. Therefore, since the vibrational cross-peaks quickly oscillate (changing their magnitude and phase) as a function of t_2, they can be expected to be averaged out in the experiment, due to the integrating effect of finite pulse envelopes. While this effect gives rise to a significant dissimilarity between simulated and measured data, on the other hand, the calculations do reproduce negative contributions to the absorptive signal part for $0 < t_2 < 20$ fs (not shown here). Thus, in line with the argumentation above, one can interpret these features to originate from the modulation of the electronic system by electron-phonon interactions, rather than being indicative of excited state absorption (in the experiment, additional negative contributions arise due to the pulse overlap effects).

Apart from the vibrational cross-peak, the impulsive limit calculations are in good qualitative agreement with the experimental data. In particular, as can be seen by inspecting both the absorptive and the dispersive signal parts (left and right column in Fig. 6.6), the

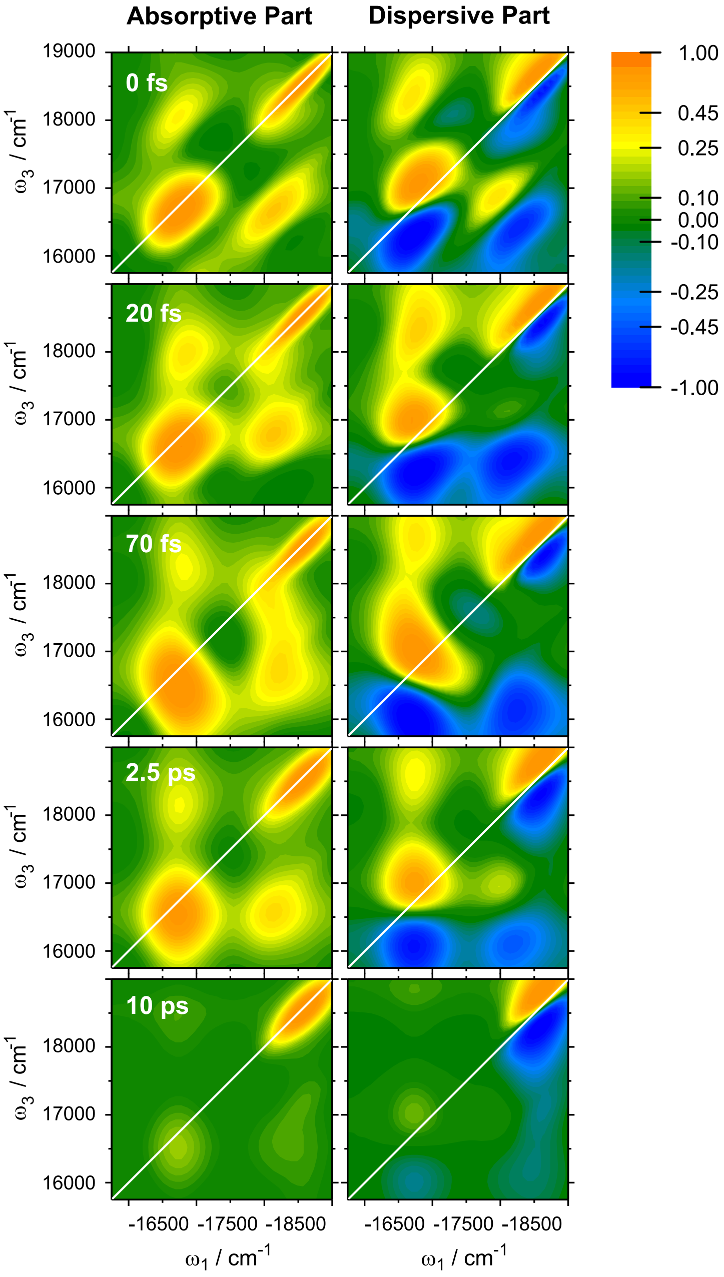

Fig. 6.6: Absorptive (left column) and dispersive (right column) parts of the simulated 2D signal for t_2-times of 0, 20, 70, 2500, and 10000 fs (from top to bottom). All spectra are normalized to the respective maximum absolute value and share the same color scale.

dynamics of the monomer peak is fairly well reproduced. Its anti-diagonal width in the absorptive 2D spectrum increases rapidly between 0 and 70 fs, and the peak acquires a circular contour at a t_2-delay of 2.5 ps. In the dispersive signal part, on the other hand, the nodal line of the monomer peak is initially oriented along the diagonal (at $t_2 = 0$ fs), while turning rapidly clockwise at increasing t_2-delays. Finally, note that for t_2 =20 and t_2 =70 fs, the tilt of the (monomeric) nodal line towards the anti-diagonal, in combination with the dynamics of the vibrational cross-peak, lead to a pronounced signal enhancement in the $|\omega_1| > \omega_3$ part of the 2D spectrum. On the basis of this observation, it is tempting to speculate that some weak remnants of these features are resembled also in the experimental data plotted in Fig. 6.2a respectively Fig. 6.3.

6.4 Conclusions

The present study combines quantum chemical calculations on the structure, geometry, and transition energies of Pinacyanol monomers and dimers, with experimental and simulated 2D electronic spectra. The quantum chemical calculations reproduce the peak positions of monomers and dimers in linear absorption, and indicate the existence of a blue-shifted absorption band for sandwich-type dimer conformations. Two-dimensional electronic spectroscopy, in turn, allows to simultaneously track the evolution of monomeric and dimeric peak shapes in real time. One observes the monomeric transition to exhibit a very fast loss of inhomogeneity, which can be followed by the evolution of the D/A-ratio in the absorptive 2D signal, and the slope of the nodal line in the corresponding dispersive signal part. The dimer contribution to the 2D spectrum, on the other hand, exhibits a remarkable absence of dynamics on the timescales explored in the experiment, lacking characteristic traces of electron-phonon interaction.

Though these findings are qualitatively in line with predictions from Frenkel exciton theory, the observed (anti-diagonal) narrowing of the dimer transitions exceeds the exchange narrowing expected from excitation delocalization. Moreover, the results indicate a high degree of inhomogeneity to be present for the dimer structures. On one hand, this is presumably related to a broad distribution of monomer distances in the dimers, implying a broad distribution of coupling strengths and excitonic transition energies. On the other hand, the data indicates that dimer formation is accompanied by a change of the dominant vibrational modes coupled to the electronic transition. The latter hypothesis is supported by the increased lifetime of the dimer. Also the fact that the dimeric 2D lineshapes (in both the absorptive and the dispersive 2D signal parts) depend only weakly on delay time t_2, suggests that the dimer transition is much less affected by intra- and/or inter-molecular phonon-modes. Although a strong vibrational cross-peak is observed in the (impulsive limit) simulations of the 2D spectra (as a consequence of the unlimited excitation bandwidth), the presented calculations provide a basis for qualitative conclusions.

The chapter is closed with two remarks. First, excitonic interactions between different *vibrational* levels are neglected in the present study. Such effects are beyond the linear semi-classical description of the system-bath coupling, but may impact quantitative aspects of the simulations. Second, in contrast to previous work (cf. Chapter V) [94], finite bandwidth effects are not accounted for. The validity of the procedure applied previously relies on a weak dependence of the nonlinear response on delay t_2, and is therefore precluded in the present context, due to inclusion of a high frequency mode for the monomer transition. Quantitative calculations based on finite pulse theory, and an explicit inclusion of at least some vibrational modes, are thus referred to forthcoming work.

7. EXCITON MOTION IN MOLECULAR NANOTUBES

In this chapter, exciton motion in a supramolecular double-walled tubular aggregate is characterized by temporal, energetic, and spatial attributes. The experimental results from two-dimensional electronic spectroscopy measurements are compared against both homogeneous and inhomogeneous microscopic models. Accounting for intra- as well as inter-wall electronic interactions in the framework of an excitonic basis, the phenomena evidenced in the experimental patterns are captured in the infinite homogeneous limit. Calculations on large but finite structures identify disorder-induced effects, which become increasingly relevant for higher energy states. Though a simple translation of energetic into spatial exciton properties fails to describe the spectrum of eigenstates, exciton funneling into lowest energy states is accompanied by spatial localization on molecular sites of the inner tubular wall.

Related publications:

Excitons and disorder in molecular nanotubes: A 2D electronic spectroscopy study and first comparison to a microscopic model
J. Sperling, A. Nemeth, J. Hauer, D. Abramavicius, S. Mukamel, H. F. Kauffmann, and F. Milota
submitted (2010)

Excitonic Couplings and Inter-band Energy Transfer in a Double-Wall Molecular Aggregate imaged by coherent 2D Electronic Spectroscopy
F. Milota, J. Sperling, A. Nemeth, D. Abramavicius, S. Mukamel, and H. F. Kauffmann
Journal of Chemical Physics, **131**, 054510 (2009)

Tracing Exciton Dynamics in Molecular Nanotubes with 2D Electronic Spectroscopy
A. Nemeth, F. Milota, J. Sperling, D. Abramavicius, S. Mukamel, and H. F. Kauffmann
Chemical Physics Letters, **469**, 130 (2009)

Two-Dimensional Electronic Photon Echoes of a Double Band J-Aggregate: Quantum Oscillatory Motion versus Exciton Relaxation
F. Milota, J. Sperling, A. Nemeth, and H. F. Kauffmann
Chemical Physics, **357**, 45 (2008)

7.1 Introduction

The effectiveness of natural light-harvesting complexes relies on delocalization and directed transfer of excitation energy on spatially well-defined arrangements of molecular absorbers. Therefore, long-range molecular order and coherent excitation delocalization are central prerequisites for engineering energy flows in bio-inspired devices.

A novel ansatz in the development of artificial light harvesters is the transfer of the self-organization tendency of organic surfactants to molecular dyes [120]. The approach relies on linking hydrophobic and hydrophilic substituents to aggregate forming molecular dyes with efficient excitonic couplings. Among such amphiphilic (hydrophilic *and* hydrophobic) chromophores, the class of cyanine derivatives has the outstanding ability to self-organize into tubular structures [121]. As illustrated in Fig. 7.1a for a tubular aggregate formed by the dye C_8S_3[1], the spatial structure of the supramolecules is well characterized [122]. In a motif that is typical for molecular nanotubes, the C_8S_3-chromophores are wrapped into a double-walled cylinder, with an inner diameter of ≈10 nm, a wall-to-wall distance of ≈4 nm, and lengths approaching the micrometer scale. The complexes thereby strongly resemble the rod elements in light-harvesting chlorosomes of green bacteria, which contain a huge number of bacteriochlorophylls in cylindrical arrangements of comparable diameters [123, 124].

Even though the idea to use self-assembled tubules as artificial light-harvesters is tantalizing, up to now, experimental and theoretical studies addressing inter-wall exciton transport have not been clearly linked. As in linear aggregates, the spectroscopic properties of cylindrical aggregates are determined by the close spatial proximity of coupled molecular transition dipoles and the consequent formation of Frenkel-excitons [29]. However, in contrast to one-dimensional structures, the linear absorption (LA) of a periodic lattice with cylindrical symmetry splits into a longitudinal (coinciding with the cylinder axis) and two energy-degenerate transversal transitions (perpendicular to the cylinder axis, cf. Fig. 7.1b) [122, 125]. The experimental LA spectrum of the double-walled C_8S_3-aggregate, on the other hand, shows three bands, with two lower energy bands (band I/band II) polarized parallel and a third band (band III) polarized predominately transversal to the main tubular axis (cf. Fig. 7.2). The question arises to which extent this spectral shape

---

[1] 3,3'-bis(3-sulfopropyl)-5,5',6,6'-tetrachloro-1,1'-dioctylbenzimidacarbocyanine

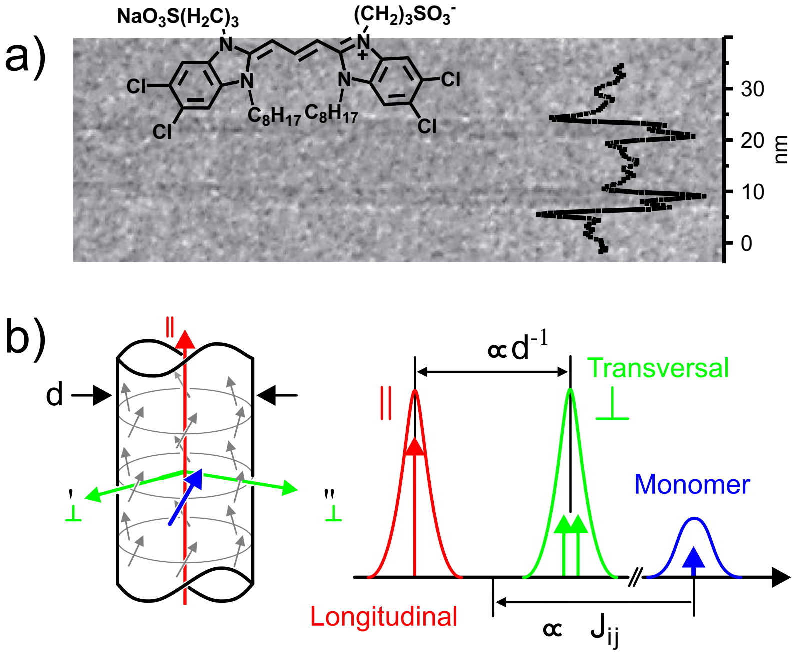

Fig. 7.1: (a) Chemical structure of the monomer and a cryogenic transmission microscopy image of the aggregated sample C_8S_3. The curve on the right side shows the horizontally integrated image gray tone. (b) Schematics of the spatial arrangement of monomer transition moments in a single wall. Electronic coupling gives rise to a longitudinal ($\mu_{||}$) and two (energy-degenerate) transversal transitions ($\mu'_{\perp}$, $\mu''_{\perp}$). The splitting $\Delta\omega$ between bands $||$ and $\perp$ is inversely proportional to the diameter of the tubule. The spectral red-shift δ with respect to the monomer transition (ω_0) reflects inter-chromophore coupling strengths.

can be regarded as an additive superposition of two single-wall contributions. So far, band-mixing effects due to inter-wall couplings have been regarded to be weak only, and, consequently, excitation energy transfer between the spectral domains assumed to be of Förster-type. This chapter presents evidence for strong electronic inter-wall interactions and their spectroscopic signatures.

7.2 Linear and Nonlinear Experiments

Sample Preparation. The sample is purchased from FEW Chemicals (Wolfen, Germany) and used as received. The dye is dissolved in water (Alfa Aesar, spectrophotometric grade) and gently stirred for one week under exclusion of light. This stock solution, with a concentration of $5{\cdot}10^{-4}$ mol/l can be stored for a few weeks without any changes in the linear absorption spectrum. For the measurements the stock solution is diluted with water (1:1) to tune the maximum absorbance to ≈0.4.

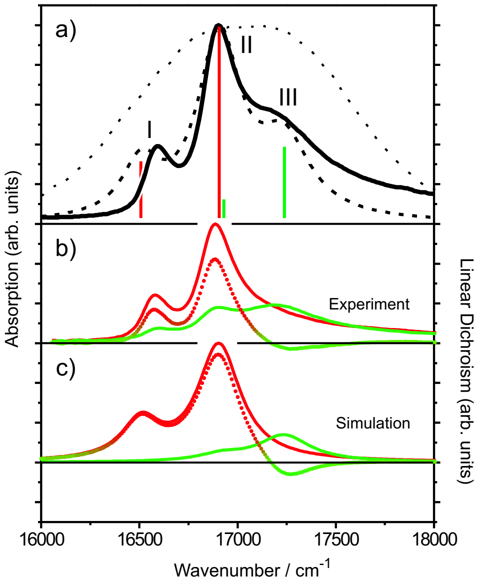

Fig. 7.2: Linear absorption (LA) spectra from experiment and infinite model simulation. (a) Isotropic LA spectrum (solid line) with labeling of bands. The dotted line shows the laser pulse spectrum for comparison. The calculated isotropic LA is shown as dashed line; vertical solid lines indicate the stick spectrum. (b) LA spectra under conditions of alignment in a flow-jet, recorded with light polarized parallel (red line, $\varepsilon_{\|}$) and vertical (green line, $\varepsilon_{\perp}$) to the flow direction. Colored dots show the corresponding linear dichroism (LD) spectrum ($\varepsilon_{\|} - \varepsilon_{\perp}$). The corresponding simulated data is shown in (c).

Linear Spectra. Due to the huge disparity in spatial dimensions, tubular aggregates tend to align along the flow direction in thin liquid films. This property can be utilized by implementing a gravity driven, wire-guided drop jet [83], in which, based on comparison with calculations, the average angle between the longitudinal tubular axes and the direction of the aligning flow is estimated to be 20°. By switching the light polarization between parallel and vertical to the jet, this allows preferential excitation of either longitudinal or transversal transition moments (for which the terminology *parallel* respectively *vertical* excitation is used in the following).

The isotropic LA spectrum of C_8S_3 in aqueous solution (cf. Fig. 7.2) shows two well-resolved peaks and a broad shoulder at higher energies (hereafter referred to as band I, II, and III, respectively). As illustrated in Fig. 7.2b, the LA substantially reshapes for parallel and vertical excitation conditions. For parallel excitation, the two strong peaks of band I and II dominate the spectrum ($\varepsilon_{\|}$), and band III appears only as a weak spectral ridge. For vertical excitation ($\varepsilon_{\perp}$) band III is the most intense feature, with a well resolved peak maximum. To considerable extent, this linear dichroism (LD $= \varepsilon_{\|} - \varepsilon_{\perp}$, cf Fig. 7.2b) has been taken to support the notion of weak inter-wall interactions. Accordingly, the two main bands (band I and band II) have been assigned to longitudinal transitions of weakly interacting cylindrical mono-layers, with transversal transitions that energetically coincide in a high energy wing (band III).

2D Correlation and Relaxation Patterns. To reduce unwanted higher-order effects and non-resonant signals from the solvent, and to prevent the sample from too fast photodegradation, the input beam is attenuated by a ND filter (after the NOPA) to yield not more than 0.5 nJ of energy in each of the excitation pulses. This energy corresponds to a fluence of $2.2 \cdot 10^{13}$ photons/cm^2 for each excitation pulse, which results in excitation of 0.08% of the molecules. For the present sample the scanning procedure for a given t_2-time (population time) requires stepping the t_1-delay from -200 fs to +200 fs in 0.65 fs steps.

Fig. 7.3 shows the amplitude representations of the complex 2D signals. Due to off-diagonal cross-intensities, the correlation spectra ($t_2 = 0$) in Fig. 7.3a and c are asymmetric with respect to the diagonal, which divides the plots into two triangular parts ($\omega_3 < |\omega_1|$ and $\omega_3 > |\omega_1|$). For parallel excitation (Fig. 7.3a), the double peak structure of the LA is recovered along the diagonal, and one observes around 20% of the maximal intensity at the band II/band I off-diagonal coordinate in $\omega_3 < |\omega_1|$. Also for vertical excitation (Fig. 7.3c), all cross-intensities in $\omega_3 < |\omega_1|$ are non-zero, although the diagonal signal of band III is substantially weaker than one would expect from its intensity in the LA. A cross-peak between band III and band I is clearly resolved. These off-diagonal intensities reveal electronic couplings between all of the three bands, the variation in the coupling patterns reflecting the dominant orientations of transition dipole moments. Parallel excitation intensifies the cross-intensity between the predominantly longitudinal transitions of band I and band II. Vertical excitation increases the relative contribution of band III and highlights its correlation with both of the two lower energy bands.

Apart from the differences in the correlation plots, the temporal evolution of the relaxation spectra is governed by comparable effects. A striking feature is the growing in of an intense cross-peak ($\omega_3 < |\omega_1|$), that arises from exciton relaxation into band I (cf. Fig. 7.3). At increasing t_2-delays, the feature acquires a more and more elliptic shape, extending from the $|\omega_1|$-coordinate of band II far into higher frequencies. Also the diagonal contours of band I and band II become pronouncedly streaked. Because of simultaneous energy uphill transfer (on a slower timescale), a much weaker off-diagonal feature appears at reversed coordinates ($\omega_3 > |\omega_1|$). This observation of concurrent exciton transfer thereby illustrates the gain in information content by a 2D spread of the system's response.

Depending on whether the system evolves in a one-exciton coherence or a coherence between a one- and a two-exciton state during t_3, absorptive 2D-ES signal parts of coupled

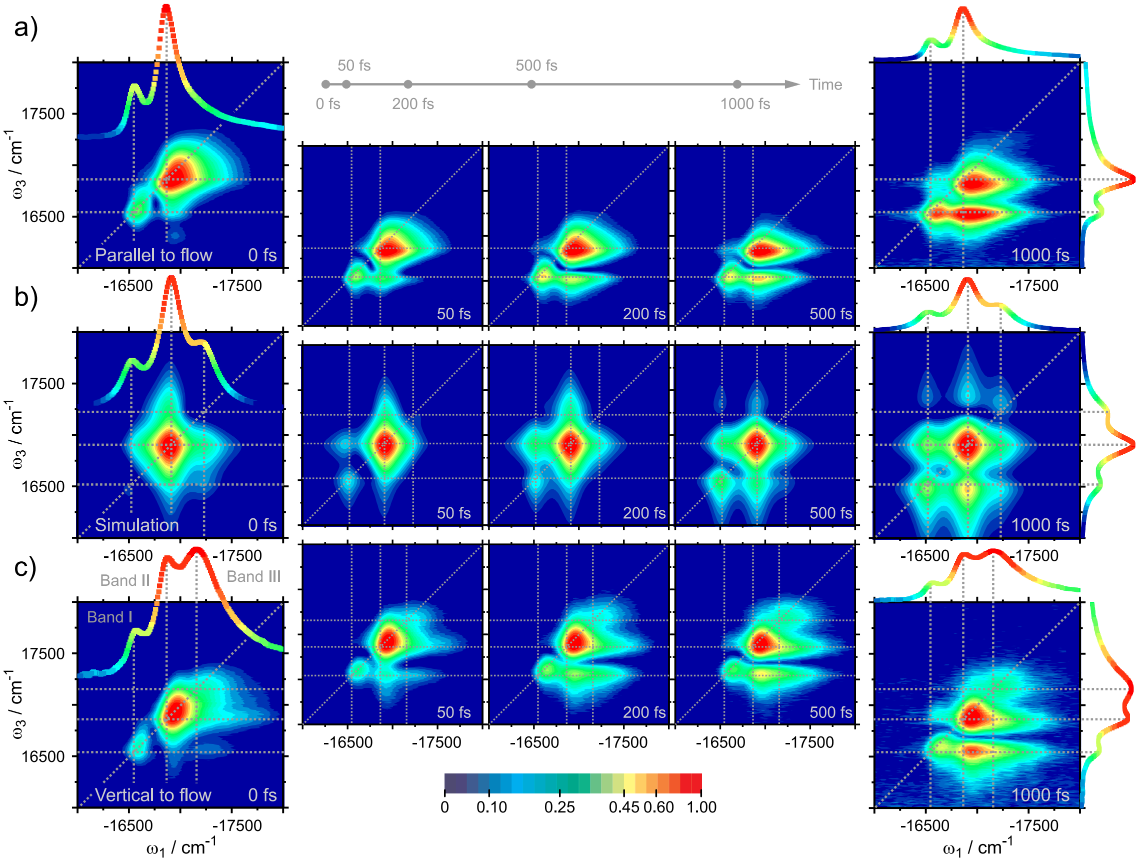

Fig. 7.3: Amplitude representations of 2D electronic spectra recorded with excitation pulses polarized (a) parallel and (c) vertical to the flow direction (all spectra are normalized). From left to right, each row shows the 2D correlation spectrum ($t_2 = 0$ fs) and relaxation spectra recorded for t_2-delays of 50, 200, 500, and 1000 fs, respectively. The corresponding (normalized) linear absorption spectra are shown for comparison in the first and last 2D spectrum of each sequence, along with dotted guidelines that mark the absorption maxima. The middle row (b) shows the calculated (spatially averaged) 2D signals of the infinite model system (also used to generate the linear spectra shown in Fig. 7.2a and c).

absorbers feature both positive and negative contributions [18, 68, 126]. In the language of pump-probe spectroscopy, 2D peaks with negative sign are related to excited-state absorption (ESA) from the one- into the two-exciton band [18, 127]. Since transitions between successively higher exciton manifolds are blue-shifted with respect to each other, ESA contributions to the 2D signal become shifted off of the diagonal into $\omega_3 > |\omega_1|$. Turning to the 2D absorptive correlation spectra shown in Fig. 7.4, one observes this effect for both lower energy bands (cf. Fig. 7.4a and c). In particular for parallel excitation, ESA signals are strong and contribute significantly to all of the recorded relaxation spectra (cf. Fig. 7.4a). For vertical excitation, the negative signals are generally weaker, and essentially disappear

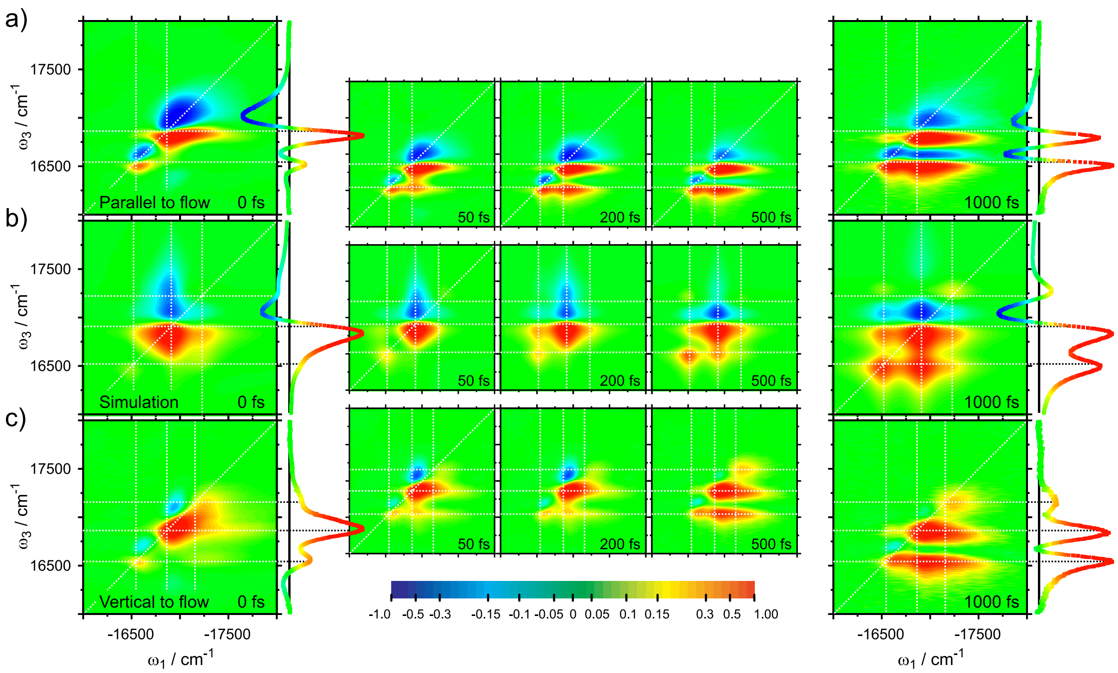

Fig. 7.4: Absorptive parts of 2D electronic spectra recorded with excitation pulses polarized (a) parallel and (c) vertical to the flow direction (same delay times as in Fig. 7.3). The curves in the side panels of the first and the last column show the 2D signals integrated along ω_1, and are equivalent to frequency resolved pump-probe spectra. The middle row (b) shows simulated data. All spectra are normalized to their maximum absolute value.

within 500 fs (cf. Fig. 7.4c). The transition probabilities into the two-exciton manifold are enhanced for one-exciton states with longitudinal transition dipoles. Due to two contributions of opposite sign, the absorptive signals reveal yet another polarization dependent effect. The appearance of the nodal line, separating positive from negative signal parts of the dominant band II peak, changes from an almost horizontal alignment (parallel excitation, Fig. 7.4a) to a more slanted orientation (vertical excitation, Fig. 7.4c). Hence, the spectral inhomogeneity, as perceived from these orientational changes [126], is correlated with the orientation of the exciton's transition dipole moments.

Beyond these aspects, the sequences of 2D absorptive spectra resemble the evolution of diagonal and off-diagonal intensities in the amplitude plots. While correlation spectra ($t_2 = 0$) are dominated by the intense signal of band II, the relaxation spectra highlight the evolution of the off-diagonal peak in $\omega_3 < |\omega_1|$ (simultaneously gaining in intensity and ellipticity) and the appearance of a considerably weaker cross-peak in $\omega_3 > |\omega_1|$. Within one picosecond, the motion of relaxing excitons thus reshapes the diagonal signals of band I and band II into peaks of almost equal intensity.

These experimental findings allow to draw two conclusions. First, 2D-ES proves that *all* of the excitonic states are coupled and share a common ground state. As to the second point, is shall be recalled that a cross-peak imaging exciton transfer in a 2D relaxation spectrum is proportional to the product of the squared transition dipole magnitudes of *both* of the states involved ($\propto |\mu_i|^2|\mu_j|^2$). This permits to observe the process as long as at least one of the states absorbs strong enough. In the present case, the formation of streaked profiles, despite the only weak diagonal intensities at high frequencies, reflects the characteristics of excitonic states to substantially change across the spectrum of eigenstates. Both of these statements are substantiated in the following.

7.3 Simulations and Discussion

Construction of a Microscopic Model. In C_8S_3, roughly one hundred sites fill a tubular volume of one nanometer length [121, 122], implying that roughly 10^4 sites are needed to set up a reasonably converged structure. On the other hand, a calculation of the nonlinear response of N excitonically coupled sites requires explicit information of the N single- and the N(N-1)/2 double-excited eigenstates [30]. A simulation of nonlinear spectra within a microscopic model that includes disorder effects is thus by far too expensive. Therefore, an infinite one-dimensional periodic lattice is employed, whose unit cell contains two circular arrangements of transition dipoles (representing molecular sites, cf. Fig. 7.5). Though limited to homogeneous broadening, this permits to calculate linear and nonlinear signals employing the quasi-particle scattering approach [127] (see Appendix).

Keeping the inter-wall distance fixed, one can observe the key spectral properties to remain essentially unaltered for a broad range of tubular diameters (if site-per-ring occupation numbers are appropriately adjusted). This allows to reduce the number of chromophores by assuming diameters of 10 nm and 3.3 nm for the outer and inner ring, respectively. The two rings are equidistantly occupied with 24 (outer wall) and 16 (inner wall) sites, reflecting the occupation ratio of roughly 60 versus 40 sites as deduced from experiment [121]. All other microscopic parameters compare well to previous estimates [122]. A lattice constant (distance of adjacent rings along the longitudinal cylinder axis) of 1.1 nm is assumed, and the site transition energies are set to ω_0 =18380 cm^{-1}. Site-to-site couplings are calculated within the extended dipole model, assuming two charges $Q = \pm 0.41e$ (e stands for electron charge) separated by l =0.56 nm (corresponding to a molecular transition dipole moment of μ = 11.03 debye). In an iterative procedure, these parameters are initialized (while restricting transition dipole orientations to tangential planes) and a fit to the experimental

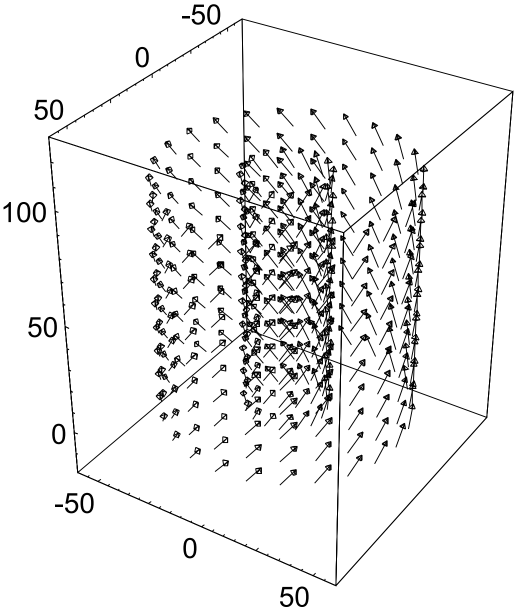

Fig. 7.5: Lattice used for simulations. Tick labels indicate the spatial dimensions in angstroms. The clip shows a stack of 10 adjacent unit cells, arrows indicate the orientation of the molecular transition dipole moments (scaled for a correspondence of 1 Debye to 1 Å).

linear absorption spectrum is performed, varying the transition dipole orientations and the system-bath coupling parameters. Doing so, one obtains the transition dipoles of the inner and outer wall oriented at an angle of 32° respectively 38° to the longitudinal cylinder axis (cf. Fig. 7.5), and an effective system-bath coupling strength of 280 cm^{-1} (timescale 50 fs). Despite the limitations inherent to an infinite model, as shown in Fig. 7.2, the linear spectra can be well reproduced.

Simulation of Nonlinear Spectra. As the essential features of the experimental 2D spectra are similar for both excitation polarizations, for the present context of experiment and theory, only spatially averaged signals (simulations of the isotropic nonlinear response) shall be discussed. As illustrated in Fig. 7.3b and Fig. 7.4b, the key spectral properties of the experimental 2D signals are fairly well reproduced. In the correlation spectra, the asymmetry of the two triangular 2D signal parts is recovered. In particular, the diagonal signal of band III is virtually missing on the normalized scale, while its cross-correlation with band II and band I is readily perceived. Similar is true for the intensity rearrangements in the sequence of 2D relaxation spectra. As can be seen by comparing the rightmost columns of Fig. 7.3 and 7.4 ($t_2 = 1000$ fs), the agreement thereby improves with increasing time delays and approaches a quantitative level, except for the cross-peaks in the $\omega_3 > |\omega_1|$ signal part (being too intense in the simulation). The relative overestimation of energy uphill transfer rates can be attributed to mainly originate from experimentally observed excited-state population decay by fluorescence from band I, which is not included in the model.

In essence, the calculations show best agreement with the experiment if the low energy regions of the 2D spectra are compared (i.e. bands I and II). This is remarkable insofar, as due to the symmetry of the perfectly ordered structure, in the homogeneous limit, the model involves only four states with a non-zero transition moment: As shown in Fig. 7.2a, the stick spectrum of the infinite lattice features two longitudinal and two transversal transitions (each of the two latter stemming from two energy-degenerate contributions with orthogonal transition dipole moments). Thus, in the experiment, the spectral properties of the corresponding bands are determined by a small number of electronic levels only. On the other hand, the limitations of the few-level approach become increasingly apparent at higher frequencies. The ongoing elongation of the cross-peak and the diagonal contour of band II, both stretching far into the high energy region of $|\omega_1|$, are not fully reconstructed. Apart from deviations that arise from the assumption of purely homogeneous lineshapes, this finding reflects a growing density of excitonic states, accompanied by a decrease of the average oscillator strength. This notion is proven in the following section, by examining the excited state manifold of a large but finite structure, in which molecular sites are spatially and energetically disordered.

Disorder and Spatio-Energetic Exciton Properties. As outlined above, essential aspects of the relaxation dynamics in tubular aggregates are presumed to originate from site disorder and the consequent variation of the spatio-energetic exciton characteristics across the spectrum. For an analysis of the manifold of excitonic states beyond the homogenous limit, the microscopic information (lattice parameters) as deduced from the infinite model is an obvious starting point. By introducing energetic and spatial site disorder, and recalculating the electronic site-to-site couplings, the exciton wavefunctions can be obtained by diagonalization of the corresponding Frenkel exciton Hamiltonian.

The finite model calculations are performed on a structure containing 80 adjacent double-rings (i.e. a total of 3200 sites), building up a tubule of roughly 90 nm length. To model orientational disorder, a random deviation of site-transition moments from their ideal lattice position is introduced. For energetic disorder, site transition energies are randomly assigned from a Gaussian distribution with a width σ_ω = 225 cm^{-1} (centered at ω_0 =18380 cm^{-1}). These parameters for static disorder ensure exciton properties to be converged for the chosen size of the system (i.e. to be independent of a further increase of the tubular length). Dynamical disorder is modeled by coupling every site to a bath

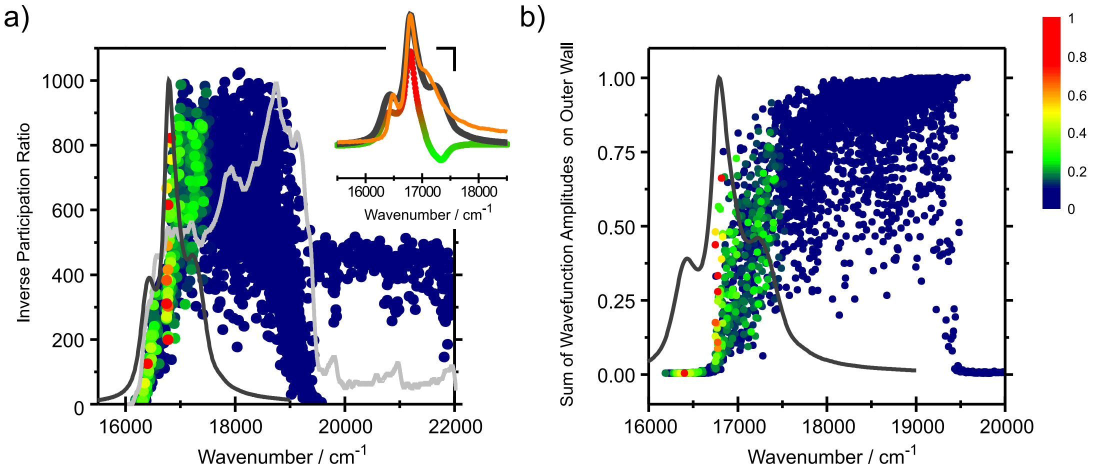

Fig. 7.6: Results from finite model calculations. Both plots (a) and (b) show the same data for a single realization of disorder. (a) Inverse participation ratio versus exciton energy. Each dot represents an excitonic state, its color indicating the normalized transition dipole moment. The plotting sequence of points thereby follows increasing transition strengths, ensuring that a particular state can be only overlaid by a state with stronger absorption. The density of states (light grey line) and the averaged absorption spectrum (dark gray line) are shown as overlay. Inset: Calculated absorption spectrum (black solid line), linear dichroism (colored dots), and the experimental absorption spectrum (solid orange line) for comparison. (b) Sum of wavefunction amplitudes located on the outer wall (see text for details). Coloring of points as in (a). The dark grey line shows the averaged LA spectrum.

mode (an overdamped Brownian oscillator with a reorganization energy of 100 cm^{-1} and a correlation time of 50 fs) [127]. To cross-check these assumptions, the averaged (10^4 realizations) linear spectra are calculated, employing the cumulant expansion of Gaussian fluctuations (CGF) approach [10]. As illustrated by the inset of Fig. 7.6a, the simulated linear spectra of the fluctuating multilevel system reproduce the experimental data, except for deviations that are analogous to the ones already observed for the infinite case.

Fig. 7.6a and b illustrate the essential characteristics of the excited state manifold for a single, representative realization of disorder (statistical averaging does not affect the conclusions). In Fig. 7.6a, the inverse participation ratio (excitation delocalization length) is plotted as a function of the absorption frequency. Each dot represents an excitonic state, and is colored according to the (normalized) absolute value of the corresponding transition dipole moment (μ_i). A comparison with the (averaged) linear absorption spectrum allows to classify bands I to III according to the underlying transitions. For each finite tubular segment, there are only a few, dominant states that contribute to band I, which can be characterized to be of highly localized nature. For band II, it is still a relatively small number of states that determine the absorption peak. However, their delocalization lengths span a wide range of values, precluding a simple characterization of the absorption band. Finally, band III, originates from a large number of only weakly absorbing excitonic states, that are less densely spaced in energy and strongly delocalized.

To extract the predominant spatial location of the excitonic wavefunctions in terms of the inner or outer tubular wall, in Fig. 7.6b, for the same data set, the sums of the wavefunction amplitudes collected on sites of the outer wall only are shown. Recalling that for every exciton wavefunction a summation of amplitudes over all sites gives unity, this fraction tends to zero for excitons that mainly reside on the inner wall (while approaching unity if the wavefunctions are spread on the outer wall only). The functional form of this plot, which resembles a rectangular shape with a rounded edge on its low energy side, is revealing. While the localization of excitons within band I, in fact, takes place on the inner wall, the states within band II are not only dispersed in delocalization lengths, but are also highly scattered in their spatial properties with respect to the double-walled structure. Again, the effect is less pronounced for band III excitons, which can be crudely described as excitations that are equally shared between both of the two aggregate walls. It should be emphasized that the strong inter-wall delocalization of all but the lowest energy states falsifies a straightforward classification of the aggregate's absorption bands.

It is essential to note that the behavior described above, even though with variably stringent contrasts, is observed for a wide range of disorder parameters. The implications for not only the spatio-energetic assignment of absorption bands, but also for the perception of the exciton relaxation process is to be underlined. Because of intra- *and* inter-wall electronic interactions, *all* bands share at least a part of their wavefunction on the inner cylindrical assembly. As band I is dominated by (site-) localized transitions located on the inner tubule, the energy downhill motion of relaxing excitons is associated with an overall spatial transfer towards the inner wall and, simultaneously, a localization on a decreasing number of molecular sites. Even for quite large tubular segments, the lower energy parts of the absorption spectrum are determined by a handful of states only. Thus, the essential spectral signatures of exciton motion might be either fitted into phenomenological schemes of effective levels [103, 101, 102, 128], or, as demonstrated in the present work, recovered in the infinite limit of a microscopic model. The finite model results, in turn, explain why a congruence of experimental data and few-level simulations becomes increasingly difficult to achieve for the high energy region of the density-of-states [101, 102]: The higher the exciton frequencies, the more the consequences of molecular disorder come into play. Thereby, disorder affects transversal transitions (with typically high transition energies) to a greater extent than longitudinal ones (which dominate the red side of the spectrum).

7.4 Conclusions

The present sample is only one out of a variety of available tubular supramolecules. Nevertheless, one can expect the key conclusions to be general, and to hold also for structures that are either spatially even more complex (like interwoven tubules [101, 102, 129]), or whose detailed microscopic structure is tuned toward new morphologies by the admixture of surfactants [101, 130]. In particular, a simple translation of spectral (energetic) band positions into spatial properties will generally fail, due to the delocalization of excitons induced by both intra- and inter-wall couplings. It is the consideration of all electronic interactions, in the framework of an excitonic Hamiltonian basis, which provides an appropriate description of the experimental data. The picture drawn here can be readily connected to the recently reported correlated fluctuation of excitonic bands in a related tubular aggregate [129]. Since all exciton wavefunctions are found to be at least partly located on one and the same wall, and to consequently overlap in space (i.e. to involve common molecular chromophores), also their fluctuations share a certain degree of correlation. Notably, the effect does not necessarily implicate correlated fluctuations of individual molecular sites. Further, even in the presence of disorder, only a relatively small number of states governs the spectroscopic properties of the aggregate. Combined with the notion that fluctuation amplitudes become exchange-narrowed for delocalized (excitonic) states, the theoretical considerations are fully in line with experimentally observed inter-band coherences [101, 128]. This study provides a guideline of how exciton motion in supramolecular systems can be studied, despite the limits currently set for connecting experimental and theoretical methodologies. Though the present work reports on an artificial light harvester which self-assembles in aqueous solution, it is inspiring to think about likely functional analogies to tubular complexes occurring in nature [124, 131], which, similarly, do not require any structural templates.

APPENDIX

For simulations of linear and nonlinear signals, a one-dimensional periodic lattice whose unit cell contains two circular arrangements of transition dipoles is employed (cf. Fig. 7.5). In the following, sites inside a unit cell are labeled by the index m, while each cell is identified by its position vector $\mathbf{R}$. Each chromophore is treated as an electronic two-level system. The chromophore coupling $J_{mm'}(\mathbf{R}-\mathbf{R}')$ is a function of the distance between the cells $\mathbf{R}$ and $\mathbf{R}'$. The real-space Hamiltonian of the system is given by [132]

$$\hat{H} = \sum_{\mathbf{R}\mathbf{R}'}\sum_{mn} J_{mn}(\mathbf{R}-\mathbf{R}')\hat{B}^{\dagger}_{\mathbf{R}m}\hat{B}_{\mathbf{R}'n} + \frac{\Delta}{2}\sum_{\mathbf{R}}\sum_{m}\hat{B}^{\dagger 2}_{\mathbf{R}m}\hat{B}^{2}_{\mathbf{R}m} \tag{7.1}$$

where $\hat{B}^{\dagger}_{\mathbf{R}m}$ is the exciton creation operator on the m^{th} chromophore in the $\mathbf{R}^{\text{th}}$ cell, and $\hat{B}_{\mathbf{R}m}$ is the conjugate annihilation operator. Boson statistics, i.e. the commutation relation $[\hat{B}_{\mathbf{R}m}, \hat{B}^{\dagger}_{\mathbf{R}'n}] = \delta_{mn}\delta_{\mathbf{R}\mathbf{R}'}$, is assumed (soft-core boson model). The first term in the Hamiltonian above represents one-exciton site energies ($\epsilon = J_{mm}(0)$) as well as resonant interactions, while the second term is a two-exciton binding parameter.

The one-exciton states of the system are Bloch states with wavefunctions

$$\Psi^{\mathbf{q}\lambda}_{\mathbf{R}m} = \frac{1}{\sqrt{L}}\mathrm{e}^{-i\mathbf{q}\mathbf{R}}\phi_{m\lambda}(\mathbf{q}) \tag{7.2}$$

where L is the number of unit cells. Each eigenstate has a pair of quantum numbers $\mathbf{q}\lambda$, where λ denotes different Davydov subbands in the one-exciton band, and $\mathbf{q} = \frac{\pi}{L}[-1, 1]$, with a step $\delta\mathbf{q} = \frac{2\pi}{L}$, is the momentum. The states $\phi_{m\lambda}(\mathbf{q})$ are the one-exciton states of a unit cell

$$\sum_{n} J_{mn}(\mathbf{q})\phi_{n\lambda}(\mathbf{q}) = \epsilon_{\lambda}(\mathbf{q})\phi_{m\lambda}(\mathbf{q}) \tag{7.3}$$

where

$$J_{mn}(\mathbf{q}) = \sum_{\mathbf{R}} \mathrm{e}^{i\mathbf{q}\mathbf{R}} J_{mn}(\mathbf{R}) \tag{7.4}$$

and $\epsilon_{\lambda}(\mathbf{q})$ is the exciton energy (in the Davydov subband λ).

The response of the excitonic system to optical fields is given in terms of many-exciton propagators (the exciton Green functions). The one-exciton Green function is $G_{\mathbf{q}\lambda}(t) = \theta(t)\mathrm{e}^{-i\epsilon_{\lambda}(\mathbf{q})t-\gamma_{\lambda}(\mathbf{q})t}$, wherein $\gamma_{\lambda}(\mathbf{q})$ is the exciton dephasing. The linear response function (used for calculating LA and LD spectra) is given by [10]

$$R^{(1)} = \sum_{\lambda} |\mu_{\lambda}|^2 G_{\lambda}(t) \tag{7.5}$$

where $\mu_{\lambda} = L\sum \mu_m \phi_{m\lambda}$ is the exciton transition dipole. It is further assumed that $La \ll \bar{\lambda}$ (where a is the lattice constant and $\bar{\lambda}$ is the optical wavelength), i.e., only zero-momentum exciton states contribute to the response.

The calculation of the nonlinear response involves two-exciton states. Using the quasi-particle representation, the third order response can be calculated from the Green function solution of the nonlinear exciton equations (NEE) [133, 132]. For the photon-echo phase-matching direction ($\mathbf{k_s} = -\mathbf{k_1} + \mathbf{k_2} + \mathbf{k_3}$) one finds

$$\begin{aligned} R^{(3)}(t_3, t_2, t_1) = & \sum_{\lambda_4\lambda_3\lambda_2\lambda_1} \sum_{\lambda_2''\lambda_3'\lambda_2'\lambda_1'} \mu_{\lambda_4}\mu_{\lambda_3}\mu_{\lambda_2}\mu_{\lambda_1} \\ & \times \int_0^\infty \mathrm{d}\tau G_{\lambda_4}(t_3 - \tau) V_{\lambda_4\lambda_1'\lambda_2'\lambda_3'} G^*_{\lambda_1'}(\tau) G^{(Y)}_{\lambda_2'\lambda_3',\lambda_2''\lambda_3}(\tau) G^{(N)}_{\lambda_2''\lambda_1',\lambda_2\lambda_1}(t_2) G^*_{\lambda_1}(t_1) \quad . \end{aligned} \tag{7.6}$$

In the expression above, V is the "scattering potential" (obtained by transforming the second term in the Hamiltonian to the one-exciton eigenstate basis), $G^{(Y)}$ is the two-exciton Green function, and $G^{(N)}$ is the one-exciton density-matrix Green function (both of the latter in the one-exciton basis). Eq. 7.6 reflects the interaction and propagation sequence in the third order response: the first interaction generates an exciton which propagates according to G^*, the second interaction generates a density matrix in one-exciton space that propagates according to $G^{(N)}$. After the third-interaction, the propagation is factorized into $G^*_{\lambda_1'}$ and $G^{(Y)}_{\lambda_2'\lambda_3',\lambda_2''\lambda_3}$, in order to account for two-exciton states. The particles finally interact through the scattering potential and generate the signal at λ_4. Similar to the linear response, only zero-momentum states are assumed to interact with the field.

To avoid the explicit calculation of $G^{(Y)}$, which involves all two-exciton states, their resonances are described using the exciton scattering matrix $\Gamma_{\lambda_4\lambda_3\lambda_2\lambda_1}$. In frequency domain one obtains

$$G^{(Y)}(\omega) = G^{(0)}(\omega) + G^{(0)}(\omega)\Gamma(\omega)G^{(0)}(\omega) \tag{7.7}$$

where $G^{(0)}_{\lambda_4\lambda_3,\lambda_2\lambda_1}(\omega) = \delta_{\lambda_4\lambda_2}\delta_{\lambda_3\lambda_1}I_{\lambda_2\lambda_1}(\omega)$ is the free two-exciton Green function with $I_{\lambda_2\lambda_1}(\omega) = (\omega - \epsilon_{\lambda_2} - \epsilon_{\lambda_1} + i\gamma_{\lambda_2} + i\gamma_{\lambda_1})^{-1}$. Using this scattering matrix and applying a double Fourier transformation, one arrives at the response function

$$\begin{aligned} R^{(3)}(\Omega_3, t_2, \Omega_1) = & \sum_{\lambda_4\lambda_3\lambda_2\lambda_1} \sum_{\lambda_2'\lambda_1'} \mu_{\lambda_4}\mu_{\lambda_3}\mu_{\lambda_2}\mu_{\lambda_1} \\ & \times G_{\lambda_4}(\Omega_3)\Gamma_{\lambda_4\lambda_1'\lambda_2'\lambda_3}(\Omega_3 + \epsilon_{\lambda_1'} + i\gamma_{\lambda_1'}) I_{\lambda_2'\lambda_3}(\Omega_3 + \epsilon_{\lambda_1'} + i\gamma_{\lambda_1'}) \\ & \times G^{(N)}_{\lambda_2'\lambda_1',\lambda_2\lambda_1}(t_2) G^*_{\lambda_1}(\Omega_1) \qquad . \end{aligned} \tag{7.8}$$

The scattering matrix is calculated using the Dyson equation [10]. For a two-level system, it is given by

$$\Gamma_{\lambda_4\lambda_3\lambda_2\lambda_1}(\omega) = \sum_{mn} \phi_{m\lambda_4}\phi_{m\lambda_3}\phi_{n\lambda_2}\phi_{n\lambda_1}[D^{-1}(\omega)]_{mn} \tag{7.9}$$

with

$$D_{mn}(\omega) = \frac{1}{L}\sum_{\mathbf{q}}\sum_{\lambda_2\lambda_1} \frac{\phi_{m\lambda_2}(\mathbf{q})\phi_{m\lambda_1}(-\mathbf{q})\phi^*_{n\lambda_2}(-\mathbf{q})\phi^*_{n\lambda_1}(\mathbf{q})}{\omega - \epsilon_{\lambda_2}(\mathbf{q}) - \epsilon_{\lambda_1}(-\mathbf{q}) + i\gamma_{\lambda_2}(\mathbf{q}) + i\gamma_{\lambda_1}(-\mathbf{q})} \qquad . \tag{7.10}$$

The exciton density matrix Green function, in turn, is obtained from the Redfield equation for the density matrix [127]:

$$\frac{\mathrm{d}}{\mathrm{d}t}\rho_{\lambda\lambda'} = -i(\epsilon_\lambda - \epsilon_{\lambda'})\rho_{\lambda\lambda'} - \sum_{\lambda''\lambda'''} K_{\lambda\lambda',\lambda''\lambda'''}\rho_{\lambda''\lambda'''} \tag{7.11}$$

where K is the Redfield relaxation rate matrix. The secular approximation for the density matrix is used (populations, i.e. diagonal elements in the density matrix, and coherences, i.e. off-diagonal elements in the density matrix, evolve independently). Populations follow the Pauli master equation, while coherences show exponentially damped oscillations [10]. Thus, the Redfield rate matrix is of the form

$$K_{\lambda\lambda',\lambda''\lambda'''} = \delta_{\lambda\lambda'}\delta_{\lambda''\lambda'''}K_{\lambda\lambda,\lambda''\lambda''} + \delta_{\lambda\lambda''}\delta_{\lambda'\lambda'''}(1-\delta_{\lambda\lambda'})\gamma^{(N)}_{\lambda\lambda'} \tag{7.12}$$

where $K_{\lambda\lambda,\lambda''\lambda''}$ is the population transport rate from exciton state λ'' to λ and $\gamma^{(N)}_{\lambda\lambda'}$ is the dephasing rate for inter-band coherence.

The final signal is obtained by convoluting the response function with the envelopes of the optical fields (pulse overlap effects are neglected). One thus obtains

$$\begin{aligned} S^{(3)}(\Omega_3, t_2, \Omega_1) = &\sum_{\lambda_4\lambda_3\lambda_2\lambda_1}\sum_{\lambda_2'\lambda_1'} \mu_{\lambda_4}\mu_{\lambda_3}\mu_{\lambda_2}\mu_{\lambda_1} \\ &\times E_4^*(\epsilon_{\lambda_4} - \omega_4)E_3(\omega_3 - \epsilon_{\lambda_3})E_2(\omega_2 - \epsilon_{\lambda_2})E_1^*(\epsilon_{\lambda_1} - \omega_1) \\ &\times G_{\lambda_4}(\Omega_3)\Gamma_{\lambda_4\lambda_1'\lambda_2'\lambda_3}(\Omega_3 + \epsilon_{\lambda_1'} + i\gamma_{\lambda_1'})I_{\lambda_2'\lambda_3}(\Omega_3 + \epsilon_{\lambda_1'} + i\gamma_{\lambda_1'}) \\ &\times G^{(N)}_{\lambda_2'\lambda_1',\lambda_2\lambda_1}(t_2)G^*_{\lambda_1}(\Omega_1) \qquad . \end{aligned} \tag{7.13}$$

The relaxation rates (cf. Eq. 7.11 and Eq. 7.12) are calculated assuming each chromophore to be coupled to a statistically independent bath, represented by a single overdamped Brownian oscillator [10]. Such a model is characterized by the spectral density of the transition energy fluctuations, $\tilde{\epsilon}(t)$ [134]:

$$C''(\omega) = \frac{1}{2}\int \mathrm{d}t e^{i\omega\tau}\langle[\tilde{\epsilon}(t), \tilde{\epsilon}(0)]\rangle = 2l\frac{\omega\Lambda}{\omega^2 + \Lambda^2} \qquad . \tag{7.14}$$

The relaxation rates in real space can be calculated using second-order perturbation theory (in fluctuations) and assuming the Markovian (fast fluctuation) limit. For the present system, using the auxiliary function [127]

$$M^{(\pm)}(\omega) = \int_0^\infty \mathrm{d}t e^{i\omega t} \int \frac{\mathrm{d}\omega}{2\pi} C''(\omega) \left[\coth\left(\frac{\beta\hbar\omega}{2}\right)\cos(\omega t) \mp i\sin(\omega t)\right] \tag{7.15}$$

one obtains

$$\gamma_\lambda = \sum_{\lambda'} M^{(+)}(\epsilon_\lambda - \epsilon_{\lambda'})\phi_{\lambda\lambda'} \tag{7.16}$$

and

$$K_{\lambda'\lambda',\lambda\lambda} = 2\mathrm{Re}M^{(+)}(\epsilon_\lambda - \epsilon_{\lambda'})\phi_{\lambda\lambda'} \tag{7.17}$$

where $\phi_{\lambda\lambda'} = \eta\sum_n \phi^2_{n\lambda}\phi^2_{n\lambda'}$. For inter-band coherences, pure dephasing is neglected and the expression $\gamma^{(N)}_{\lambda\lambda'} = \frac{1}{2}(K_{\lambda\lambda,\lambda\lambda} + K_{\lambda'\lambda',\lambda'\lambda'})$ is used.

8. OUTLOOK

We start off confused and end up confused on a higher level.

A. F. Chalmers in his book *What is this thing called science?*

Related publication:

Compact phase-stable design for single- and double-quantum two-dimensional electronic spectroscopy
A. Nemeth, J. Sperling, J. Hauer, H. F. Kauffmann, and F. Milota
Optics Letters, **34**, 3301 (2009)

Emerging Experimental Refinements

The presentation of this work has been done with the intention to illustrate how two-dimensional electronic spectroscopy (2D-ES) can simply visualize the physics behind complex third-order nonlinear spectroscopic signals. In view of the relatively simple experimental implementation presented here, one can certainly expect 2D-ES to become recognized and accessed by a broader scientific community - even though “2D-spectrometers” will probably not become commercially available as ready-to-use “black boxes” in the very next future. Nevertheless, since 2D-ES has distinct advantages if compared to other nonlinear methods, it has the potential to attain a comparable level of importance for studying electronic processes as 2D nuclear magnetic resonance has for determining molecular structures. The success of NMR and its continuing application to increasingly larger molecules not least results from a great freedom in generating sophisticated, specifically tailored pulses sequences, containing up to hundreds of pulses. Such developments are out of reach in 2D-ES, due to physical barriers that limit the attainable nonlinear signal intensities. However, also in 2D-ES, emerging methodological variations rely on refinements of the pulse sequence for enhancing desired signal pathways, in tandem with experiments designed to access correlations of successively higher excited states.

Recent examples of such developments are experiments devised to directly probe double-quantum coherences, i.e. coherences between single- and double-excited states [135]. In the experimental realization described in the present work, constant phase relations within the sequence of excitation pulses (and the local oscillator) are accomplished only pairwise, which imposes limitations on the time-delays that can be Fourier transformed without loss of phase information. Only recently, employing a pulse shaper [28], by implementing active phase-stabilization [60], or by uncoupling of time-delays [71], this limitation has been overcome, offering access to new types of 2D frequency-frequency correlations. Further, an universal set-up has been reported, that is easy to implement and align, yet provides passive phase-stability between all four pulses involved in the experiment [136]. The proposed design not only permits to carry out a variety of four-wave mixing experiments, but also allows to reliably record single-quantum and double-quantum (2Q) 2D-ES spectra, as illustrated for the electronic multi-level structure of a linear molecular aggregate in Fig. 8.1 [136]. In even more complex excitonic systems, where congested peak patterns

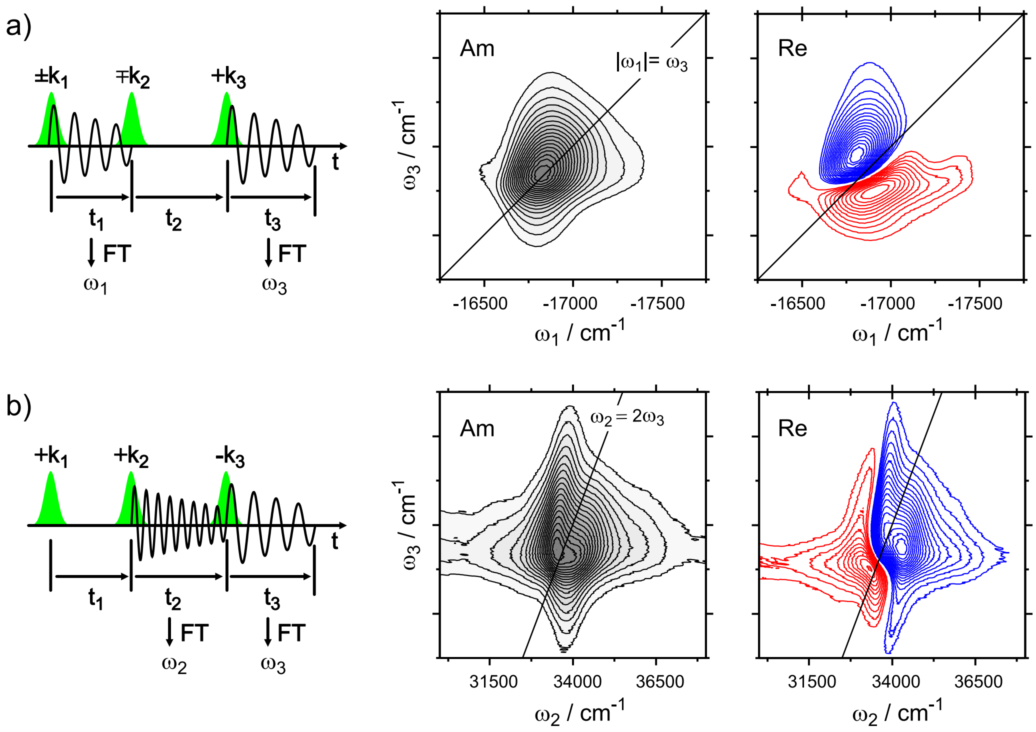

Fig. 8.1: Comparison of conventional 2D-ES and double-quantum (2Q) 2D-ES. The amplitude (Am) and real part (Re) representation of experimental data recorded with both methods for a linear molecular aggregate is shown. (a) In 2D-ES, the real part representation of the signal reveals two contributions giving rise to an intense peak in the amplitude spectrum. Positive features (red) are associated with single-quantum coherences (ground-state bleach/stimulated emission pathways), while the negative feature (blue) originates from coherences between single- and double excited states (excited state absorption). (b) In 2Q 2D-ES, the system is in a double-quantum coherence during t_2, oscillating at approximately twice the frequency of single-quantum coherences. After Fourier transformation, the single peak in the amplitude spectrum now appears along $\omega_2 \approx 2\omega_3$. Again, two contributions adding up to form the amplitude spectrum can be distinguished in the real part of the two-dimensional spectrum.

may hamper the analysis of conventional 2D data, 2Q 2D-ES can be expected to provide valuable information on how signals are to be assigned to contributions arising from single- and double-quantum coherences. In particular, one can envision to directly explore the correlations between double excited states and their constituent single excited states, by spreading their signatures into two different frequency axes [135].

The complexity of nonlinear signals, which commonly rapidly grows with the number coupled molecular chromophores, has been also the driving force behind the so-called method of cross-peak specific 2D-ES, aimed to selectively highlight electronic coupling effects in two-dimensional signals [137]. The principle of cross-peak specific 2D-ES relies on a particular choice of pulse polarizations, for specific enhancement of nonlinear response pathways that otherwise become obscured by broad diagonal features. As has been demonstrated, a selective elimination of diagonal signals can reveal electronic intermolecular interactions that can not be resolved by conventional 2D-ES spectra [137]. Moreover, the cross-peak specific technique causes some response pathways to contribute with opposite sign to the 2D signal, which facilitates the assignment of cross-peaks to specific nonlinear response pathways (based on sign changes) and allows for stringent tests against theoretical models. A captivating notion is that, in principle, all possible polarization sequences can be constructed from linear combinations of three orthogonal sequences [138]. Thus, given experimental recordings for only three polarization conditions, it should be possible to construct arbitrary polarization dependent spectra. The idea to employ programmable pulse shaping in this context is tantalizing.

Future Perspective

It appears fair to say that the extension of two-dimensional electronic spectroscopy with ultra-broadband excitation sources, enabling experimentalists to cover the entire visible range, is predictable, as is a shift of forthcoming studies towards higher frequency regimes. On the one hand, extending experiments into the regime of ultraviolet radiation will not only give access to spectral regions where residues of proteins absorb, but also permit to study smaller and hence simpler chromophores, which can be tackled with high-level electronic structure calculations. On the other hand, the feasibility of broadband excitation might connect future 2D-ES studies to open questions in non-equilibrium dynamics. One can envision, e.g., to apply a 2D-ES pulse sequence to a system that has been previously kicked into a non-equilibrium state, like a reactive crossing, by yet another laser pulse.

In a general perspective, the potential of 2D-ES currently relies to a considerable extent on the support that can be provided by theoretical modeling, which is particularly prolific if the *spatial* structure of a molecular complex under study is already more or less well known. For studies of systems for which spatial information is not readily at hand, it will be essential to develop strategies that can extract more quantitative information directly from experimental data. The above described refinements might open new stages of multi-dimensional spectroscopy, in which space-energy relationships between interacting electronic systems will be visualized for an increasingly broader range of molecular systems, both from the natural and the synthetic world.

BIBLIOGRAPHY

[1] E. L. Hahn, *Phys. Rev.*, **80**, 580 (1950).

[2] W. P. Aue, E. Bartholdi, and R. R. Ernst, *J. Chem. Phys.*, **64**, 2229 (1976).

[3] R. R. Ernst, G. Bodenhausen, and A. Wokaun, *Principles of Nuclear Magnetic Resonance in One and Two Dimensions.*, Clarendon Press, 1987.

[4] K. Wüthrich, *NMR of Proteins and Nucleic Acids*, Wiley, 1986.

[5] R. P. Feynman, F. L. Vernon, and R. W. Hellwarth, *J. Appl. Phys.*, **28**, 49 (1957).

[6] B. Vogelsanger, M. Andrist, and A. Bauder, *Chem. Phys. Lett.*, **144**, 180 (1988).

[7] T. H. Maiman, *Nature*, **187**, 493 (1960).

[8] N. A. Kurnit, I. D. Abella, and S. R. Hartmann, *Phys. Rev. Lett.*, **13**, 567 (1964).

[9] M. D. Levenson and S. S. Kano, *Introduction to Nonlinear Laser Spectroscopy*, Academic Press, 1987.

[10] S. Mukamel, *Principles of Nonlinear Optical Spectroscopy*, Oxford University Press, 1995.

[11] Y. R. Shen, *The Principles of Nonlinear Optics*, John Wiley & Sons, 2002.

[12] R. W. Boyd, *Nonlinear Optics*, Academic Press, 2003.

[13] A. H. Zewail, *J. Phys. Chem. A*, **104**, 5660 (2000).

[14] S. Mukamel, *Ann. Rev. Phys. Chem.*, **51**, 691 (2000).

[15] M. T. Zanni, *Curr. Opin. Struc. Biol.*, **11**, 516 (2001).

[16] R. M. Hochstrasser, *Proc. Nat. Acad. Sci.*, **104**, 14190 (2007).

[17] P. Hamm, J. Helbing, and J. Bredenbeck, *Ann. Rev. Phys. Chem.*, **59**, 291 (2008).

[18] M. Cho, *Chem. Rev.*, **108**, 1331 (2008).

[19] N. T. Hunt, *Chem. Soc. Rev.*, **38**, 1837 (2009).

[20] D. M. Jonas, *Ann. Rev. Phys. Chem.*, **54**, 425 (2003).

[21] L. Lepetit, G. Chériaux, and M. Joffre, *J. Opt. Soc. Am. B*, **12**, 2467 (1995).

[22] J. D. Hybl, A. W. Albrecht, S. M. G. Faeder, and D. M. Jonas, *Chem. Phys. Lett.*, **297**, 307 (1998).

[23] T. Brixner, J. Stenger, H. M. Vaswani, M. Cho, R. E. Blankenship, and G. R. Fleming, *Nature*, **434**, 625 (2005).

[24] D. Zigmantas, E. L. Read, T. Mancal, T. Brixner, A. T. Gardiner, R. J. Cogdell, and G. R. Fleming, *Proc. Nat. Acad. Sci.*, **103**, 12672 (2006).

[25] G. S. Engel, T. R. Calhoun, E. L. Read, T. K. Ahn, T. Mančal, Y. C. Cheng, R. E. Blankenship, and G. R. Fleming, *Nature*, **446**, 782 (2007).

[26] F. Milota, J. Sperling, A. Nemeth, T. Mancal, and H. F. Kauffmann, *Acc. Chem. Res.*, **42**, 1364 (2009).

[27] E. Collini and G. D. Scholes, *Science*, **323**, 369 (2009).

[28] K. Stone, K. Gundogdu, D. B. Turner, X. Li, S. T. Cundiff, and K. A. Nelson, *Science*, **324**, 1169 (2009).

[29] A. S. Davydov, *Theory of Molecular Excitons*, Plenum Press, 1971.

[30] S. Mukamel and D. Abramavicius, *Chem. Rev.*, **104**, 2073 (2004).

[31] F. C. Spano, *Phys. Rev. Lett.*, **67**, 3424 (1991).

[32] R. Kubo, *Adv. Chem. Phys.*, **15**, 101 (1969).

[33] J. R. Schmidt, N. Sundlass, and J. L. Skinner, *Chem. Phys. Lett.*, **378**, 559 (2003).

[34] Y. J. Yan and S. Mukamel, *J. Chem. Phys.*, **89**, 5160 (1988).

[35] Y. J. Yan and S. Mukamel, *Phys. Rev. A*, **41**, 6485 (1990).

[36] W. M. Zhang, T. Meier, V. Chernyak, and S. Mukamel, *J. Chem. Phys.*, **108**, 7763 (1998).

[37] W. M. Zhang, T. Meier, V. Chernyak, and S. Mukamel, *Phil. Trans. R. Soc. A*, **356**, 405 (1998).

[38] M. Yang and G. R. Fleming, *Chem. Phys.*, **282**, 163 (2002).

[39] M. Cho, H. M. Vaswani, T. Brixner, J. Stenger, and G. R. Fleming, *J. Phys.Chem. B*, **109**, 10542 (2005).

[40] F. Milota, A. Tortschanoff, J. Sperling, L. Kuna, V. Szöcs, and H. F. Kauffmann, *Appl. Phys. A*, **78**, 497 (2004).

[41] F. Milota, J. Sperling, V. Szöcs, A. Tortschanoff, and H. F. Kauffmann, *J. Chem. Phys.*, **120**, 9870 (2004).

[42] V. Szöcs, T. Palszegi, A. Tortschanoff, and H. F. Kauffmann, *J. Chem. Phys.*, **116**, 8218 (2002).

[43] B. S. Prall, D. Y. Parkinson, G. R. Fleming, M. Yang, and N. Ishikawa, *J. Chem. Phys.*, **120**, 2537 (2004).

[44] J. A. Cina, D. S. Kilin, and T. S. Humble, *J. Chem. Phys.*, **118**, 46 (2003).

[45] R. M. Hochstrasser, *Nature*, **434**, 570 (2005).

[46] K. Okumura, A. Tokmakoff, and Y. Tanimura, *Chem. Phys. Lett.*, **314**, 488 (1999).

[47] V. May and O. Kühn, *Charge and Energy Transfer Dynamics in Molecular Systems*, Wiley VCH, 2000.

[48] M. J. S. Dewar, E. G. Z. E. F. Healy, and J. J. P. Stewart, *J. Am. Chem. Soc.*, **107**, 3902 (1985).

[49] V. Lukes, M. Breza, D. Vegh, P. Hrdlovic, and V. Laurinc, *Synth. Met.*, **138**, 399 (2003).

[50] *Rev. Comp. Chem. Vol. 2*, Editors K. B. Lipkowitz and D. B. Boyd, VCH Publishing, 1991.

[51] *Hyperchem Rel. 7.5*, Hyperchem Inc., 1995.

[52] A. L. Thompson, K. M. Gaab, J. Xu, C. J. Bardeen, and T. J. Martinez, *J. Phys. Chem. A*, **108**, 671 (2004).

[53] W. P. de Boeij, M. S. Pshenichnikov, and D. A. Wiersma, *Chem. Phys. Lett.*, **238**, 1 (1995).

[54] W. P. de Boeij, M. S. Pshenichnikov, and D. A. Wiersma, *J. Phys. Chem.*, **100**, 11806 (1996).

[55] W. P. de Boeij, M. S. Pshenichnikov, and D. A. Wiersma, *Ann. Rev. Phys. Chem.*, **49**, 99 (1998).

[56] W. P. de Boeij, M. S. Pshenichnikov, and D. A. Wiersma, *Chem. Phys.*, **233**, 287 (1998).

[57] L. Lepetit and M. Joffre, *Opt. Lett.*, **21**, 564 (1996).

[58] N. Belabas and M. Joffre, *Opt. Lett.*, **27**, 2043 (2002).

[59] C. N. Borca, T. Zhang, X. Li, and S. T. Cundiff, *Chem. Phys. Lett.*, **416**, 311 (2005).

[60] A. D. Bristow, D. Karaiskaj, X. Dai, T. Zhang, C. Carlsson, K. R. Hagen, R. Jimenez, and S. T. Cundiff, *Rev. Sci. Inst.*, **80**, 73108 (2009).

[61] P. Tian, D. Keusters, Y. Suzaki, and W. S. Warren, *Science*, **300**, 1553 (2003).

[62] E. M. Grumstrup, S.-H. Shim, M. A. Montgomery, N. H. Damrauer, and M. T. Zanni, *Opt. Exp.*, **15**, 16681 (2007).

[63] J. A. Myers, K. L. M. Lewis, P. F. Tekavec, and J. P. Ogilvie, *Opt. Exp.*, **16**, 17420 (2008).

[64] K. Gundogdu, K. W. Stone, D. B. Turner, and K. A. Nelson, *Chem. Phys.*, **341**, 89 (2007).

[65] G. D. Goodno, G. Dadusc, and R. J. D. Miller, *J. Opt. Soc. Am. B*, **15**, 1791 (1998).

[66] M. L. Cowan, J. P. Ogilvie, and R. J. D. Miller, *Chem. Phys. Lett.*, **386**, 184 (2004).

[67] T. Brixner, I. V. Stiopkin, and G. R. Fleming, *Opt. Lett.*, **29**, 884 (2004).

[68] T. Brixner, T. Mančal, I. V. Stiopkin, and G. R. Fleming, *J. Chem. Phys.*, **121**, 4221 (2004).

[69] A. M. Moran, J. B. Maddox, J. W. Hong, J. Kim, R. A. Nome, G. C. Bazan, S. Mukamel, and N. F. Scherer, *J. Chem. Phys.*, **124**, 194904 (2006).

[70] U. Selig, F. Langhojer, F. Dimler, T. Löhrig, C. Schwarz, B. Gieseking, and T. Brixner, *Opt. Lett.*, **33**, 2851 (2008).

[71] V. I. Prokhorenko, A. Halpin, and R. J. D. Miller, *Opt. Exp.*, **17**, 9764 (2009).

[72] G. L., R. Ernstorfer, E. Riedle, R. Eichberger, and F. Willig, *Appl. Phys. B*, **80**, 727 (2005).

[73] P. Baum, M. Breuer, E. Riedle, and G. Steinmeyer, *Opt. Lett.*, **31**, 2220 (2006).

[74] C. Iaconis and I. A. Walmsley, *Opt. Lett.*, **23**, 792 (1998).

[75] C. Iaconis and I. A. Walmsley, *IEEE J. Quantum Elect.*, **35**, 501 (1999).

[76] P. Baum, S. Lochbrunner, and E. Riedle, *Opt. Lett.*, **29**, 210 (2004).

[77] P. Baum and E. Riedle, *J. Opt. Soc. B*, **22**, 1875 (2005).

[78] T. Wilhelm, J. Piel, and E. Riedle, *Opt. Lett.*, **22**, 1494 (1997).

[79] J. Piel, E. Riedle, L. Gundlach, R. Ernstorfer, and R. Eichberger, *Opt. Lett.*, **31**, 1289 (2006).

[80] G. Steinmeyer, *Opt. Exp.*, **11**, 2385 (2003).

[81] R. Szipöcs and A. Köhazi-Kis, *Appl. Phys. B*, **65**, 115 (1997).

[82] M. Khalil, N. Demirdöven, and A. Tokmakoff, *Phys. Rev. Lett.*, **90**, 47401 (2003).

[83] M. J. Tauber, R. A. Mathies, X. Chen, and S. E. Bradforth, *Rev. Sci. Inst.*, **74**, 4958 (2003).

[84] S. Laimgruber, H. Schachenmayr, B. Schmidt, W. Zinth, and P. Gilch, *Appl. Phys. B*, **85**, 557 (2006).

[85] A. V. Pisliakov, T. Mančal, and G. R. Fleming, *J. Chem. Phys.*, **124**, 234505 (2006).

[86] P. Kjellberg, B. Brüggemann, and T. Pullerits, *Phys. Rev. B*, **74**, 24303 (2006).

[87] D. Egorova, M. F. Gelin, and W. Domcke, *Chem. Phys.*, **341**, 113 (2007).

[88] D. Egorova, M. F. Gelin, and W. Domcke, *J. Chem. Phys.*, **126**, 74314 (2007).

[89] Y.-C. Cheng, G. S. Engel, and G. R. Fleming, *Chem. Phys.*, **341**, 285 (2007).

[90] Y.-C. Cheng and G. R. Fleming, *J. Phys. Chem. A*, **112**, 4254 (2008).

[91] D. S. Larsen, K. Ohta, and G. R. Fleming, *J. Chem. Phys.*, **111**, 8970 (1999).

[92] D. S. Larsen, K. Ohta, Q.-H. Xu, M. Cyrier, and G. R. Fleming, *J. Chem. Phys.*, **114**, 8008 (2001).

[93] S. M. Gallagher-Faeder and D. M. Jonas, *J. Phys. Chem. A*, **103**, 10489 (1999).

[94] A. Nemeth, F. Milota, T. Mančal, V. Lukeš, H. F. Kauffmann, and J. Sperling, *Chem. Phys. Lett.*, **459**, 94 (2008).

[95] K. Ohta, D. S. Larsen, M. Yang, and G. R. Fleming, *J. Chem. Phys.*, **114**, 8020 (2001).

[96] G. Scheibe, *Angw. Chem.*, **49**, 563 (1936).

[97] E. E. Jelley, *Nature*, **138**, 1009 (1936).

[98] A. B. Myers, *Ann. Rev. Phys. Chem.*, **49**, 267 (1998).

[99] J. L. Skinner and W. E. Moerner, *J. Phys. Chem.*, **100**, 13251 (1996).

[100] E. L. Read, G. S. Schlau-Cohen, G. S. Engel, J. Wen, R. E. Blankenship, and G. R. Fleming, *Biophys. J.*, **95**, 847 (2008).

[101] F. Milota, J. Sperling, A. Nemeth, and H. F. Kauffmann, *Chem. Phys.*, **357**, 45 (2009).

[102] A. Nemeth, F. Milota, J. Sperling, D. Abramavicius, S. Mukamel, and H. F. Kauffmann, *Chem. Phys. Lett.*, **469**, 130 (2009).

[103] F. Milota, J. Sperling, A. Nemeth, D. Abramavicius, S. Mukamel, and H. F. Kauffmann, *J. Chem. Phys.*, **131**, 54510 (2009).

[104] V. Szöcs, T. Palszegi, V. Lukes, J. Sperling, F. Milota, W. Jakubetz, and H. F. Kauffmann, *J. Chem. Phys.*, **124**, 124511 (2006).

[105] W. West and S. Pearce, *J. Phys. Chem.*, **69**, 1894 (1965).

[106] C. J. Tredwell and C. M. Keary, *Chem. Phys.*, **43**, 307 (1979).

[107] P. J. Thistlethwaite and H. J. Griesser, *Chem. Phys. Lett.*, **91**, 58 (1982).

[108] F. Heisel, J. A. Miehe, and J. Rachidi, *Chem. Phys. Lett.*, **134**, 379 (1987).

[109] B. Aradi, B. Hourahine, and T. Frauenheim, *J. Phys. Chem. A*, **111**, 5678 (2007).

[110] R. Ahlrichs, M. Bär, M. Häser, H. Horn, and C. Kölmel, *Chem. Phys. Lett.*, **162**, 165 (1989).

[111] J. B. Collins, P. R. Schleyer, J. S. Binkley, and J. A. Pople, *J. Chem. Phys.*, **64**, 5142 (1976).

[112] A. D. Becke, *J. Chem. Phys.*, **104**, 1040 (1996).

[113] J. P. Perdew, K. Burke, and M. Ernzerhof, *Phys. Rev. Lett.*, **77**, 3865 (1996).

[114] *GAUSSIAN 03, Revision A.1*, Gaussian Inc., 2003.

[115] H. Min, J. Park, J. Yu, and D. Kim, *Bull. Kor. Chem. Soc.*, **19**, 650 (1998).

[116] B. Neumann and P. Pollmann, *Phys. Chem. Chem. Phys.*, **2**, 4784 (2000).

[117] R. Sabate, M. Gallardo, A. de la Manza, and J. Estelrich, *Langmuir*, **17**, 6433 (2001).

[118] B. Kopainsky, J. K. Hallermeier, and W. Kaiser, *Chem. Phys. Lett.*, **83**, 498 (1981).

[119] E. W. Knapp, *Chem. Phys.*, **85**, 73 (1984).

[120] J. Knoester, Ed., *Light-harvesting J-Aggregates*, Special Issue of the International Journal of Photoenergy, 2006.

[121] S. Kirstein and S. Dähne, *Int. J. Photoenergy*, **2006**, 1 (2006).

[122] C. Didraga, A. Pugžlys, P. R. Hania, H. von Berlepsch, K. Duppen, and J. Knoester, *J. Phys. Chem. B*, **108**, 14976 (2004).

[123] V. I. Prokhorenko, D. B. Steensgaard, and A. R. Holzwarth, *Biophys. J.*, **85**, 3173 (2003).

[124] S. Ganapathy, G. T. Oostergetel, P. K. Wawrzyniak, M. Reus, A. G. M. Chew, F. Buda, E. J. Boekema, D. A. Bryant, A. R. Holzwarth, and H. J. M. de Groot, *Proc. Nat. Acad. Sci.*, **109**, 8525 (2009).

[125] K. Didraga, J. A. Klugkist, and J. Knoester, *J. Phys. Chem. B*, **106**, 11474 (2002).

[126] I. Stiopkin, T. Brixner, M. Yang, and G. R. Fleming, *J. Phys. Chem. B*, **110**, 20032 (2006).

[127] D. Abramavicius, B. Palmieri, D. V. Voronine, F. Sanda, and S. Mukamel, *Chem. Rev.*, **109**, 2350 (2009).

[128] J. M. Womick, S. A. Miller, and A. M. Moran, *J. Phys. Chem. A*, **113**, 6587 (2009).

[129] J. M. Womick, S. A. Miller, and A. M. Moran, *J. Phys. Chem. B*, **113**, 6630 (2009).

[130] H. von Berlepsch, S. Kirstein, and C. Böttcher, *Langmuir*, **18**, 7699 (2002).

[131] Z. G. Fetisova, A. M. Freiberg, and K. E. Timpmann, *Nature*, **334**, 633 (1988).

[132] V. Chernyak, W. M. Zhang, and S. Mukamel, *J. Chem. Phys.*, **109**, 9587 (1998).

[133] F. C. Spano and S. Mukamel, *J. Chem. Phys.*, **95**, 7526 (1991).

[134] V. Chernyak and S. Mukamel, *J. Chem. Phys.*, **105**, 4565 (1996).

[135] J. Kim, S. Mukamel, and G. D. Scholes, *Acc. Chem. Res.*, **42**, 1375 (2009).

[136] A. Nemeth, J. Sperling, J. Hauer, H. F. Kauffmann, and F. Milota, *Opt. Lett.*, **34**, 3301 (2009).

[137] E. L. Read, G. S. Engel, T. R. Calhoun, T. Mančal, T. K. Ahn, R. E. Blankenship, and G. R. Fleming, *Proc. Nat. Acad. Sci.*, **104**, 14203 (2007).

[138] N. S. Ginsberg, Y.-C. Cheng, and G. R. Fleming, *Acc. Chem. Res.*, **42**, 1352 (2009).

ABSTRACT

Though a variety of time-resolved spectroscopies of electronic transitions have come of age, only recent experimental progress allows to exploit coherent pulse sequences, and to adopt concepts that were initially developed in nuclear magnetic resonance spectroscopy. Two-dimensional electronic spectroscopy (2D-ES) correlates electronic transition frequencies that evolve in different time intervals, and is currently becoming recognized as a unique tool for gathering spectral information that can not be accessed directly by other spectroscopic methods. The content of this thesis substantiates this statement, by presenting theoretical and experimental studies of increasingly complex molecular systems, covering the range from non-interacting dye molecules in solution to a supramolecular assembly of coupled molecular absorbers.

After a brief presentation of underlying concepts, an exemplary theoretical study on the information content of 2D electronic spectra is presented, focusing on their potential to distinguish between different conformations of electronically coupled dimers. In the following, experimental hurdles in the implementation are discussed, and a passively phase-stabilized 2D experimental set-up is described, suitable for studies across the entire visible spectrum. For the simplest possible case of an electronic two-level absorber, the motion of a low-frequency vibrational wavepacket in a perylene-based dye is traced experimentally. By simultaneously monitoring monomers and van-der-Waals bound dimers of an aggregating molecular chromophore, it is then illustrated how 2D line-shapes are affected by exciton delocalization induced by electronic inter-molecular couplings. Finally, electronic interactions are found to dominate the optical response of a self-assembling aggregate, in which the motion of excitons, relaxing across a multi-band spectrum, is characterized by temporal, spatial, and energetic attributes. Forthcoming developments are subsumed in the outlook.

ZUSAMMENFASSUNG

Obwohl sich während der letzten Jahrzehnte eine Vielzahl von Techniken zur Ultrakurzpuls-Spektroskopie elektronischer Übergänge etablieren konnte, sind Messungen mit koheränten Pulssequenzen erst seit wenigen Jahren möglich. Dieser Forschritt in der Instrumentierung erlaubt, die ursprünglich in der Kernspinresonanzspektroskopie entwickelten multidimensionalen Konzepte auch im sichtbaren Bereich des elektromagnetischen Spektrums experimentell umzusetzen. Zwei-Dimensionale Elektronische Spektroskopie (2D-ES) ist in der Lage, elektronische Koheränzen zwischen verschiedenen Zeitintervallen zu korrelieren, und erlaubt damit die eine direkte Abfrage von spektralen Informationen, die in alternativen Exerimenten nur indirekt zugänglich oder gänzlich verborgen sind. Die vorliegende Arbeit untermauert diese Aussage mit theoretischen und experimentellen Untersuchungen molekularer Systeme zunehmender Komplexität.

Nach einer kurzen Diskussion theoretischer Grundlagen wird zunächst der Informationsgehalt von 2D Spektren anhand von Modellrechnungen an einem Ensemble von konformativ ungeordneten, elektronisch gekoppelten Dimeren illustriert. Anschließend werden die Hürden bei der experimentellen Implementierung von 2D-ES diskutiert und ein passiv phasen-stabilisierter Aufbau beschrieben, der Versuche im gesamten sichbaren Wellenlängenbreich ermöglicht. Experimente an einem Perylen-Farbstoff, einem einfachen molekularen System mit nur zwei relevanten elektronischen Zuständen, illustrieren durch das Verfolgen einer niederfrequenten Vibration wie sich vibronische Effekte in der Dynamik von 2D Spektren wiederspiegeln. Eine gleichzeitige spektrale Vermessung der monomeren und der van-der-Waals gebundenen dimeren Form eines aggregierenden Chromophors zeigt, daß inter-molekulare Wechselwirkungen und die konsequente Delokalisierung elektronischer Zustände direkt mit 2D-ES vermessen werden kann. Inter-molekulare elektronische Kopplungen dominieren die optische Antwortfunktion des abschließend untersuchten supramolekularen Aggregates, in welchem die Relaxation von elektronischen Exzitonen durch 2D-ES temporal, spatial, und energetisch charakterisiert wird. Die Arbeit schließt mit einem Ausblick auf mögliche zukünftige Weiterentwicklungen multi-dimensionaler elektronischer Spektroskopien.

CURRICULUM VITAE

* 18.05.1975, Vienna

02/2007 - 08/2007	Department of Chemistry, University of California, Irvine
02/2005 - 05/2005	Chair for BioMolecular Optics, Ludwig-Maximilians-Universität, Munich
04/2003	Awarded doctoral scholarship from the Austrian Academy of Sciences
08/2001	Diploma thesis with distinction
1993 - 2001	Study of chemistry at the University of Vienna
1985 - 1993	Secondary school in Vienna, final exams with distinction

LIST OF PUBLICATIONS

Articles

Excitons and disorder in molecular nanotubes: A 2D electronic spectroscopy study and first comparison to a microscopic model
J. Sperling, A. Nemeth, J. Hauer, D. Abramavicius, S. Mukamel, H. F. Kauffmann, and F. Milota
submitted (2010)

Vibrational wave packet induced oscillations in two-dimensional electronic spectra. I. Experiments
A. Nemeth, F. Milota, T. Mancal, V. Lukes, J. Hauer, H. F. Kauffmann, and J. Sperling
Journal of Chemical Physics, *submitted* (2010)

Vibrational wave packet induced oscillations in two-dimensional electronic spectra. II. Theory
T. Mancal, A. Nemeth, F. Milota, V. Lukes, H. F. Kauffmann, and J. Sperling
Journal of Chemical Physics, *submitted* (2010)

Two-dimensional Electronic Spectroscopy of β-carotene
N. Christensson, F. Milota, A. Nemeth, J. Sperling, H. F. Kauffmann, T. Pullerits, and J. Hauer
Journal of Physical Chemistry B, **113**, 16409 (2009)

Compact phase-stable design for single- and double-quantum two-dimensional electronic spectroscopy
A. Nemeth, J. Sperling, J. Hauer, H. F. Kauffmann, and F. Milota
Optics Letters, **34**, 3301 (2009)

Two-dimensional electronic spectroscopy of molecular excitons
F. Milota, J. Sperling, A. Nemeth, T. Mancal, and H. F. Kauffmann
Accounts of Chemical Research, **42**, 1364 (2009)

Excitonic couplings and inter-band energy transfer in a double-wall molecular aggregate imaged by coherent 2D electronic spectroscopy
F. Milota, J. Sperling, A. Nemeth, D. Abramavicius, S. Mukamel, and H. F. Kauffmann
Journal of Chemical Physics, **131**, 54510 (2009)

Two-Dimensional Electronic Spectra of an Aggregating Dye: Simultaneous Measurement of Monomeric and Dimeric Line-Shapes
A. Nemeth, V. Lukes, J. Sperling, F. Milota, H. F. Kauffmann, and T. Mancal
Physical Chemistry Chemical Physics, **11**, 5986 (2009)

Tracing exciton dynamics in molecular nanotubes with 2D electronic spectroscopy
A. Nemeth, F. Milota, J. Sperling, D. Abramavicius, S. Mukamel, and H. F. Kauffmann
Chemical Physics Letters, **469**, 130 (2009)

Two-Dimensional Electronic Photon Echoes of a Double Band J-Aggregate: Quantum Oscillatory Motion versus Exciton Relaxation
F. Milota, J. Sperling, A. Nemeth, and H. F. Kauffmann
Chemical Physics, **357**, 45 (2009)

Vibronic modulation of lineshapes in two-dimensional electronic spectra
A. Nemeth, F. Milota, T. Mancal, V. Lukes, H. F. Kauffmann, and J. Sperling
Chemical Physics Letters, **459**, 94 (2008)

Exciton Dynamics in a Disordered Conjugated Polymer: Three-Pulse Photon-Echo and Transient Grating Experiments
J. Sperling, A. Nemeth, P. Baum, F. Sanda, E. Riedle, H. F. Kauffmann, S. Mukamel, and F. Milota
Chemical Physics, **349**, 244 (2008)

Theoretical investigation of the structure and the electron-vibrational dynamics of 9,9$'$-spirobifluorene
V. Lukes, R. Solc, F. Milota, J. Sperling, and H. F. Kauffmann
Chemical Physics, **349**, 226 (2008)

Two-Dimensional Electronic Spectra of Symmetric Dimers: Intermolecular Coupling and Conformational States
V. Szocs, T. Palszegi, V. Lukes, J. Sperling, F. Milota, W. Jakubetz, and H. F. Kauffmann
Journal of Chemical Physics, **124**, 124511 (2006)

Density Matrix Analysis, Simulation, and Measurements of Electronic Absorption and Fluorescence Spectra of Spirobifluorenes
V. Lukes, T. Palszegi, F. Milota, J. Sperling, and H. F. Kauffmann
Journal of Physical Chemistry A, **110**, 1775 (2006)

Excitonic Relaxation in a Conjugated Polymer: Initial Coherence beyond Energy-Dispersive Population Transfer
J. Sperling, F. Milota, and H. F. Kauffmann
Optics and Spectroscopy, **98**, 795 (2005)

Correlation of femtosecond wavepackets and fluorescence interference in a conjugated polymer: Towards the measurement of site homogeneous dephasing
F. Milota, J. Sperling, V. Szocs, A. Tortschanoff, and H. F. Kauffmann
Journal of Chemical Physics, **120**, 9870 (2004)

Effects of excitation tuning on ultrafast exciton dynamics in poly(p-phenylene-vinylene)
J. Sperling, C. Benesch, L. Kuna, H. F. Kauffmann, and F. Milota
Synthetic Metals, **143**, 315 (2004)

Probing phase relaxation, by measuring fluorescence interference: polarization beatings and electron-phonon coupling in conjugated polymers
F. Milota, J. Sperling, A. Tortschanoff, L. Kuna, V. Szocs, and H. F. Kauffmann
Journal of Luminescence, **108**, 205 (2004)

Femtosecond Coherence in Poly(p-Phenylenevinylene)
F. Milota, A. Tortschanoff, J. Sperling, L. Kuna, V. Szöcs, and H. F. Kauffmann
Applied Physics A, **78**, 497 (2004)

Femtosecond Excitation Tuning and Site Energy Memory of Population transfer in poly(p-phenylenevinylene): Gated Luminescence Experiments and Simulations
J. Sperling, F. Milota, A. Tortschanoff, Ch. Warmuth, B. Mollay, H. Bässler, and H. F. Kauffmann
Journal of Chemical Physics, **117**, 10877 (2002)

Ultrafast Optical Dynamics of Spiro-Compounds
F. Milota, Ch. Warmuth, A. Tortschanoff, J. Sperling, T. Fuhrmann, J. Salbeck, and H.F. Kauffmann
Synthetic Metals, **121**, 1497 (2001)

Book Contributions

Vibrational Beating in Two-Dimensional Electronic Spectra
A. Nemeth, F. Milota, T. Mancal, V. Lukes, H. F. Kauffmann, and J. Sperling
Ultrafast Phenomena XVI, Springer Series in Chemical Physics, **92** (2009)

2D optical spectroscopy of a conjugated polymer with tuneable visible 15fs-pulses from a 200kHz NOPA
F. Milota, P. Baum, J. Sperling, E. Riedle, K. Matuszna, and H. F. Kauffmann
Ultrafast Phenomena XV, Springer Series in Chemical Physics, **88** (2007)

Unveilling electronic phase relaxation in a strongly disordered conjugated polymer
J. Sperling, F. Milota, A. Tortschanoff, V. Szocs, L. Kuna, C. Benesch, and H. F. Kauffmann
Femtochemistry and Femtobiology - Ultrafast Events in Molecular Science, Elsevier (2004)

Photodynamics of conjugated polymer systems
J. Sperling, C. Benesch, B. Mollay, H. F. Kauffmann, and F. Milota
Trends in Physical Chemistry, **10**, 135 (2004)

Electronic excitation oscillations in PPV - Femtosecond luminescence interferometry
A. Tortschanoff, F. Milota, J. Sperling, V. Szöcs, and H. F. Kauffmann
Ultrafast Phenomena XIII, Springer Series in Chemical Physics, **71** (2003)

Optical dynamics in semiconducting polymers probed by ultrafast spectroscopies
J. Sperling, F. Milota, L. Kuna, C. Warmuth, K. Brunner, H. F. Kauffmann and A. Tortschanoff
Recent Research Developments in Chemical Physics, **4**, 125 (2003)

The complex puzzle of optical femto-dynamics in PPV - Hidden Coherences and energy dispersive population transfer
J. Sperling, F. Milota, A. Tortschanoff, C. Warmuth, and H. F. Kauffmann
Femtochemistry and Femtobiology - Ultrafast Dynamics in Molecular Science, World Scientific (2002)

ACKNOWLEDGEMENTS

The studies described in this thesis have been carried out with the Ultrafast Dynamics group of Harald F. Kauffmann at the University of Vienna and the Technical University of Vienna, with partial financial support from the Austrian Academy of Sciences (doctoral scholarship program DOC). I am very grateful to Harald F. Kauffmann for passionately supporting the work in a fascinating field of science with numerous discussions, advice and vision, and for always encouraging the group to broaden the scientific education at international conferences, workshops, and sojourns abroad.

I am grateful to Eberhard Riedle (Ludwig-Maximilians-Universität, Munich) and Shaul Mukamel (University of California, Irvine), their expertise and the interactions with their groups have given me invaluable experiences.

Among many more people without whom this work could not have been realized in its present form, I wish to explicitly thank Franz Milota and Alexandra Nemeth for not only their contributions and their support throughout the years, but also for sharing all the ups and downs of scientific and nonscientific everyday life.

I wish to thank my parents for their love, and Verena for her love and for her humour.